

Interface-Resolving Simulations of Gas-Liquid Two-Phase Flows in Solid Structures of Different Wettability

Zur Erlangung des akademischen Grades
Doktor der Ingenieurwissenschaften
der Fakultät für Maschinenbau
Karlsruher Institut für Technologie (KIT)

genehmigte
Dissertation

von

M. Sc. Xuan Cai

Tag der mündlichen Prüfung:	16. Dezember 2016
Hauptreferentin:	Prof. Dr.-Ing. Bettina Frohnafel
Korreferent:	Prof. Dr. rer. nat. habil. Olaf Deutschmann
Korreferent:	Prof. Dr.-Ing. habil. Bernhard Weigand



This document is licensed under the Creative Commons Attribution – Share Alike 3.0 DE License (CC BY-SA 3.0 DE): <http://creativecommons.org/licenses/by-sa/3.0/de/>

Acknowledgements

First and foremost, I would like to deeply appreciate Dr. Martin Wörner, my scientific advisor. With his immense knowledge and patience, Martin has provided me invaluable scientific advice and guidance, indispensable organizational supports and constant encouragement throughout all my PhD study. Besides, I would like to express sincere gratitude to Prof. Olaf Deutschmann who has given me a lot of valuable scientific suggestions as well as organizational supports during my PhD work at AKD. I am greatly grateful to Prof. Bettina Frohnäpfel for accepting to be my official supervisor at Department of Mechanical Engineering and for her great interest and encouragement on my PhD work. Also, I would like to thank Prof. Bernhard Weigand for being my PhD co-examiner.

My deep gratitude also goes to several non-Karlsruhers: I greatly appreciate Dr. Holger Marschall for his significant contributions during our productive cooperation on the phase-field method development and implementation in OpenFOAM®. I am very grateful to Prof. Pengtao Yue for sharing me his deep insights on the phase-field method and also for his great hospitality during my research visit to him at Virginia Tech. I would like to thank Prof. Alla Hocine for intensive scientific discussions on wetting-related topics during his visits to us at KIT.

I would like to express my gratitude to my collaborators at KIT. I would like to thank Dipl.-Ing Sebastian Meinicke for our collaboration on CFD for sponge structure within the Helmholtz Energy Alliance. I appreciate M.Sc. Verena Fink for our cooperation for co-supervising a master-thesis project. I am grateful to my colleagues M.Sc. Anna Abai and M.Sc. Marion Börnhorst for our collaboration within the project SFB/Transregio 150. Besides I would like to thank Mr. Farshid Jamshidi, Mr. Sumedh Yadav and Mr. Ronan Bernard for their assistance during their students' projects with us.

I own many thanks to other AKD colleagues besides Anna and Marion mentioned above. I greatly appreciate Mrs. Ursula Schwald and Mr. Martin Spoo for their great supports with administrative and IT issues respectively. I would like to thank Dipl.-Ing Carlos Falconi, M.Sc. Sercan Erdogan and M.Sc. Mino Woo for their daily helps and pleasant discussions on scientific/non-scientific topics in office or during lunch time. Besides my thanks go to Dr. Matthias Hettel, Dr. Lubow Maier, Dr. Vikram Menon, Dr. Hüseyin Karadeniz, Dr. Alexander Zellner, M.Sc. Sivaram Kannepalli, M.Sc. Henning Stotz, M.Sc. Aayan Banerjee – among others – for the enjoyable discussions with them.

I am deeply indebted to my family and friends in Wuhan, Munich, Karlsruhe and Blacksburg. I am very grateful to my parents who are always there to support and encourage me. Especially, I would like to thank my girlfriend Jiaqi for her companionship and patience.

Finally I acknowledge Helmholtz Energy Alliance “Energy-efficient chemical multiphase processes” (HA-E-0004) and SFB/Transregio 150 "Turbulent, chemical reacting multi-phase flows near walls" for funding my PhD study and Karlsruhe House of Young Scientists (KHYS) for financially supporting my research visit to Virginia Tech.

Abstract

This PhD study is devoted to numerical investigations of two-phase flows on and through elementary and complex solid structures of varying wettability. Reliable numerical simulations of such multi-phase and multi-scale processes require an accurate modeling of the motion of the three-phase contact line. For this, conventional sharp interface models suffer from a classical paradox between moving contact line and no-slip boundary condition at solid wall. A promising approach for resolving this paradox is the phase-field method, where the interface is treated as a transition layer of small but finite thickness. This method provides a pure diffusive mechanism for the motion of contact line which can be used in combination with a no-slip boundary condition at solid walls.

During the study, the phase-field method is developed and implemented in OpenFOAM®. Therein the Cahn-Hilliard equation for phase-field description is coupled with the Navier-Stokes equations for incompressible fluid flows. The numerical method and code are verified by a series of test cases of two-phase flows. These include phase-field diffusion, droplet deformation in shear flow, capillary rise in vertical channel and equilibrium state of droplet on solid surface. In all the cases, excellent agreement is achieved with analytical solutions from literature. Then, the method is successfully applied to reproduce several representative droplet-wetting phenomena in real-life scenarios, ranging from elementary spreading dynamics on horizontal surfaces to complex wetting on chemically-heterogeneous substrates. The computational results are in good match with experimental and numerical data from literature.

Subsequently, this thesis presents an innovative numerical study for wettability dependent interaction of a rising bubble with solid structures. By comparison with experimental data from literature, the numerical method is firstly validated for terminal bubble rise velocity and instantaneous cylinder-induced bubble cutting behavior. The numerical method is then employed to study the behavior of a single air bubble rising

through a representative subdomain of a periodic open cellular structure (POCS) filled with stagnant water. The results indicate that the bubble shape and path do significantly depend on the structure wettability. The current numerical investigation suggests a clear evidence that the utilization of structures with high wettability is beneficial for enhancing mass transfer and catalytic reactions in industrial chemical reactors packed with POCS.

Moreover with the numerical method, local two-phase interfacial hydrodynamics in heterogeneous foam structures is investigated. After the validation for gas flow hydrodynamics in alumina sponge structure, the method is applied to interface-resolving simulations of gas-liquid two-phase flows in a representative elementary volume (REV) of Silicon Infiltrated Silicon Carbide (SiSiC) foam structure. To obtain a physical liquid phase distribution in such a REV, a modeling strategy is proposed and developed by mirroring computational domain and imposing periodic boundary conditions. Then qualitative and quantitative investigations are carried out to shed light on influences of physical parameters (i.e. liquid saturation, structure wettability and interfacial tension) on gas-liquid interfacial area. Such detailed insights gained from the present simulations are very useful for characterization of local interfacial phenomena in complex solid foam structure, which is rather challenging to access experimentally.

All the results above altogether show that the phase-field method and numerical solver developed in OpenFOAM® are reliable and promising computational tools for investigating interfacial two-phase flows on and through elementary and complex solid structures.

Kurzfassung

Diese Doktorarbeit beschäftigt sich mit numerischen Untersuchungen von Zweiphasenströmungen auf und durch elementare und komplexe feste Strukturen von unterschiedlicher Benetzbarkeit. Zuverlässige numerische Simulationen von solchen Mehrphasen- und Mehrskalen-Prozessen erfordern eine fundierte Modellierung der bewegten Kontaktlinien. Hierbei gibt es bei konventionellen Modellen mit scharfer Grenzfläche ein Paradoxon zwischen der bewegten Kontaktlinie und der Haftbedingung an einer festen Wand. Ein vielversprechender Ansatz zur Auflösung dieses Paradoxons ist die Phasenfeld Methode, bei der die Grenzfläche als Schicht mit kleiner aber endlicher Dicke betrachtet wird. Dieser Ansatz stellt einen rein diffusiven Mechanismus bereit, der eine Bewegung der Kontaktlinie in Kombination mit der Haftbedingung auf der festen Wand erlaubt.

Im Rahmen der Arbeit wird eine Phasenfeld Methode für das Rechenprogramm OpenFOAM[®] entwickelt und implementiert. Dabei wird die Cahn-Hilliard-Gleichung für die Beschreibung der Phasenverteilung mit den inkompressiblen Navier-Stokes-Gleichungen für die Zweiphasenströmung gekoppelt. Der Code wird zunächst anhand einer Reihe von Testfällen verifiziert. Diese umfassen Phasenfeld-Diffusion, Tropfen-Deformation in einer Scherströmung, kapillarer Aufstieg im vertikalen Kanal und den Gleichgewichtszustand von Tropfen auf festen Oberflächen. Für alle Testfälle wird eine exzellente Übereinstimmung der numerischen Ergebnisse mit entsprechenden analytischen Lösungen aus der Literatur erreicht. Danach wird der numerische Löser erfolgreich angewendet, um praktische Benetzungsphänomene von Tropfen nachzurechnen. Diese reichen von elementarer Tropfen-Ausbreitungsdynamik auf horizontalen Oberflächen bis hin zur komplexen Benetzung auf chemisch heterogenen Substraten. Auch für diese Fälle stimmen die Berechnungsergebnisse gut mit experimentellen und numerischen Daten aus der Literatur überein.

Darauf folgend präsentiert die Dissertation eine innovative numerische Untersuchung der Interaktion einer aufsteigenden Luftblase mit festen Strukturen. Dazu wird das numerische Modell zunächst für die stationäre Steiggeschwindigkeit der Blase und ihre Zerteilung durch einen horizontalen Zylinder anhand experimenteller Ergebnisse aus der Literatur validiert. Daran anschließend wird der Blasenauftstieg in einem repräsentativen Teilgebiet einer periodischen offen zelligen Struktur („Periodic Open Cellular Structure“, POCS) untersucht. Dabei zeigt sich, dass die Form und das Aufstiegsverhalten der Blase maßgeblich von der Benetzbarkeit der Struktur abhängen. Die numerischen Ergebnisse legen nahe, dass für die Intensivierung von Stofftransport und katalytischen Reaktionen in industriellen chemischen Reaktoren POCS mit guter Benetzbarkeit vorteilhaft sind.

In einem weiteren Anwendungsschwerpunkt werden Strömungen in heterogenen Schwammstrukturen untersucht. Der numerische Löser wird zunächst für die einphasige Gasströmung in einer Aluminiumoxid-Schwammstruktur validiert, und dann für die grenzflächenauflösenden Simulationen von Gas-Flüssig-Zweiphasenströmungen in einem repräsentativen elementaren Volumenelement (REV) einer Schwammstruktur aus Silizium-infiltriertem Siliziumcarbid (SiSiC) angewendet. Um eine physikalische Phasenverteilung an den Ein- und Austrittsrändern des Rechengbietes zu erreichen, wird eine Modellierungsstrategie eingesetzt. Dazu wird das REV gespiegelt, so dass periodische Randbedingungen verwendet werden können. Darauf basierend werden qualitative und quantitative Untersuchungen durchgeführt, um die Einflüsse von verschiedenen Parametern (z.B. Flüssigkeitssättigung, Benetzbarkeit, Oberflächenspannung) auf die Gas-Flüssig-Grenzfläche aufzuklären. Diese Ergebnisse sind nützlich für die Charakterisierung der Grenzfläche in komplexen festen Schwammstrukturen, bei denen experimentelle Messungen sehr schwierig sind.

Die Gesamtheit der Ergebnisse dieser Dissertation belegt, dass die Phasenfeld-Methode und der neu entwickelte numerische Löser in OpenFOAM® sehr zuverlässige

und vielversprechende Berechnungsansätze für Untersuchungen von Grenzflächenphänomenen in Zweiphasenströmungen auf und durch elementare und komplexe feste Strukturen darstellen.

Contents

Acknowledgements	i
Abstract.....	iii
Kurzfassung	v
Contents	viii
1 Introduction.....	1
1.1 Motivation.....	1
1.2 Physical Fundamentals	4
1.2.1 Surface Tension.....	4
1.2.2 Surface Tension near Wall – Wetting	5
1.2.3 Contact Angles at Moving Contact Line – Scales, Scales, Scales	6
1.3 Theoretical Basics for Moving Contact Line Flow Problems	11
1.3.1 Hydrodynamic Theory.....	11
1.3.2 Molecular-Kinetic Theory	14
1.4 Numerical Simulations for Moving Contact Line: State-of-the-Art	15
1.4.1 Volume-of-Fluid (VOF) methods.....	15
1.4.2 Level-Set (LS) methods	17
1.4.3 Front-Tracking (FT) methods.....	17
1.4.4 Phase-Field (PF) methods.....	17
1.5 Objectives and Contributions of This Study	22
1.5.1 Method Development and Numerical Implementation	23
1.5.2 Droplet Wetting on Homogenous/Heterogeneous Surfaces	23
1.5.3 Bubble Motion in Periodic Open Cellular Structure (POCS)	24
1.5.4 Gas-Liquid Interfacial Flow in Sponge Structure.....	25
1.6 Thesis Outline	26

2	Mathematical Formulation and Numerical Methodology.....	28
2.1	Governing Equations.....	28
2.1.1	Convective Cahn-Hilliard Equation	28
2.1.2	Navier-Stokes Equations	30
2.1.3	Dimensionless Formulation	31
2.1.4	Considerations for Choosing ε and κ	32
2.2	Numerical Methodology	34
2.2.1	Implementation Platform – OpenFOAM®.....	34
2.2.2	Numerical Implementation of Phase-Field Method	35
2.3	Summary of Chapter 2.....	37
3	Verification for Fundamental Interfacial Phenomena.....	38
3.1	Phase-Field Diffusion.....	38
3.2	Droplet Deformation in Unbounded Shear Flow.....	41
3.3	Capillary Rise in Vertical Channel.....	44
3.4	Summary of Chapter 3.....	46
4	Droplet Wetting on Flat Solid Surfaces	47
4.1	Equilibrium Shape.....	47
4.2	Spreading Dynamics.....	50
4.2.1	2D Axisymmetric Simulations	50
4.2.2	3D Simulations with Adaptive Mesh Refinement	52
4.3	Droplet Spreading on Chemically-Heterogeneous Surfaces.....	55
4.4	Summary of Chapter 4.....	59
5	Interaction of a Rising Bubble with Solid Structures.....	60
5.1	Introduction	60
5.2	Terminal Bubble Rise Velocity	61
5.2.1	Physical Properties and Computational Set-up	61
5.2.2	Numerical Parameter Study.....	63

5.2.3	Validation.....	66
5.3	Cylinder-induced Bubble Cutting.....	67
5.3.1	Computational Set-up.....	68
5.3.2	Mesh Resolution Study.....	68
5.3.3	Validation.....	70
5.3.4	Influence of Cylinder Wettability.....	72
5.4	Bubble Rise through a Periodic Open Cellular Structure	75
5.4.1	Fluid Properties and Computational Set-up	75
5.4.2	Results.....	76
5.4.3	Discussion	80
5.5	Summary of Chapter 5.....	82
6	Gas-liquid Two-phase Flows in Sponge Structures.....	83
6.1	Introduction and Motivation.....	83
6.2	Validation for Single-phase Gas Flow in Sponge Structure	85
6.2.1	Computational Geometry and Mesh	85
6.2.2	Physical Properties and Computational Set-ups.....	87
6.2.3	Comparison with Reference Experimental and Computational Results....	89
6.3	Interface-resolving Simulation of Two-phase Flows in Sponge Structure	89
6.3.1	Modelling Strategy.....	89
6.3.2	Physical Properties and Computational Set-ups.....	92
6.3.3	Results and Discussions.....	93
6.4	Summary of Chapter 6.....	100
7	Summary and Outlook.....	101
7.1	Summary and Conclusion.....	101
7.2	Outlook and Future Work.....	102

Appendix A. Workflow of Running a *phaseFieldFoam* Test Case. 105
References..... 110
Nomenclature..... 122
List of Abbreviations..... 125
List of Figures 126

1 Introduction

This chapter firstly introduces the motivation for studying wetting phenomena and then related physical fundamentals. Special attention is paid to the inherent multi-scale nature of dynamic wetting where moving contact line (MCL) problem is involved. Theories of MCL physics on different scales are then presented and the state-of-the-art of numerical simulations on MCL flows in literature are reviewed. Among them, phase-field method-based simulations are elaborated since the present PhD work is based on this method.

1.1 Motivation

Two-phase interfacial flows on solid surface are usually termed as wetting phenomena. The wetting phenomena are omnipresent in nature [1]. One of the most striking examples that nature inspires us concerning wetting is the lotus effect; see Figure 1.1. Dewdrops either slide over the leaf and are about to fall down, or stay and form the shapes as shown there. These phenomena are attributed to very high water repellence of the leaf (i.e., super-hydrophobicity) induced by microscopic textures of the leaf surface.



Figure 1.1: Lotus effect of dewdrops on a leaf (from Bonn et al. [1]).

Besides, wetting phenomena are very common in our daily life. For a passenger who takes a train-trip on a rainy day, it is a familiar experience to see an irregular array of rain droplets sticking or “traveling-down” over the outboard surface of a window (see Figure 1.2).

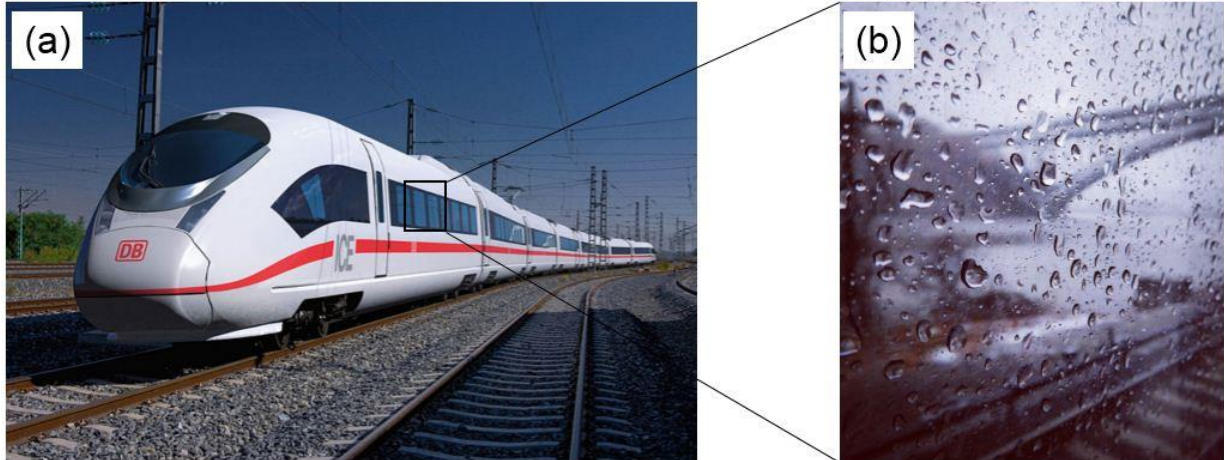


Figure 1.2: On a high-speed train (a), we might have an enjoyable watching experience of wetting when observing rain droplets over the window (b). The picture (a) and (b) are adapted respectively from Trainmountain [2] and Meyerson [3].

Furthermore, wetting phenomena are crucial processes in many industrial applications; in-depth understanding of wetting behavior potentially leads to technological improvement in these industrial processes. One example is found in lab-on-a-chip systems as shown, for example, by Figure 1.3. For such a microfluidics system, accurate knowledge of wetting is a prerequisite for precise manipulation of micro-droplets locations and motions [4].

Another example showing high relevance of wetting process to industrial application is found in multiphase chemical reactors; see Figure 1.4. For such a reactor, internal

structures are nowadays widely used; these are usually referred to as structured

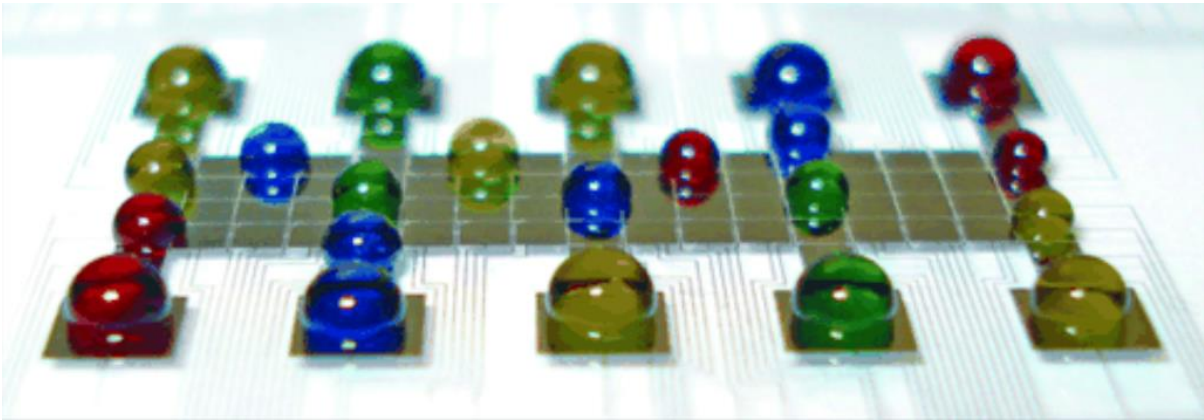


Figure 1.3: A digital microfluidic system (from Jebrail et al. [5]). There each droplet is working as a micro-reactor where parallel reactions can take place with no cross-interference or cross-contamination.

packing [6] (e.g. see Figure 1.4 a). Conventionally, monolith or honeycomb structures are used for structured packing [7]. Just in recent years, chemical engineers have developed some innovative concepts of using novel internal structures, such as periodic open-cell structure (POCS) [8, 9] (see Figure 1.4 b) or sponge structure [10-13] (see Figure 1.4 c). These new structures exhibit advantages over those traditional ones, in the sense of enhanced heat and mass transfer as well as favorability for catalytic chemical reaction if structure surface is coated with catalysts. These structure-packed multiphase reactors normally involve at least two fluid phases, typically gas and liquid. Both the phases could be continuous as demonstrated by the gas-liquid interfacial flows in a representative domain of sponge structure (see Figure 1.4 e), or one phase is continuous and the other is dispersed (see Figure 1.4 d that shows the interaction of POCS and a rising bubble as dispersed phase immersed in a continuous liquid phase). Accurate knowledge of these two-phase interfacial hydrodynamics interacting with the solid packing structures boils down to deep insights into local wetting phenomena (see Figure 1.4 f).

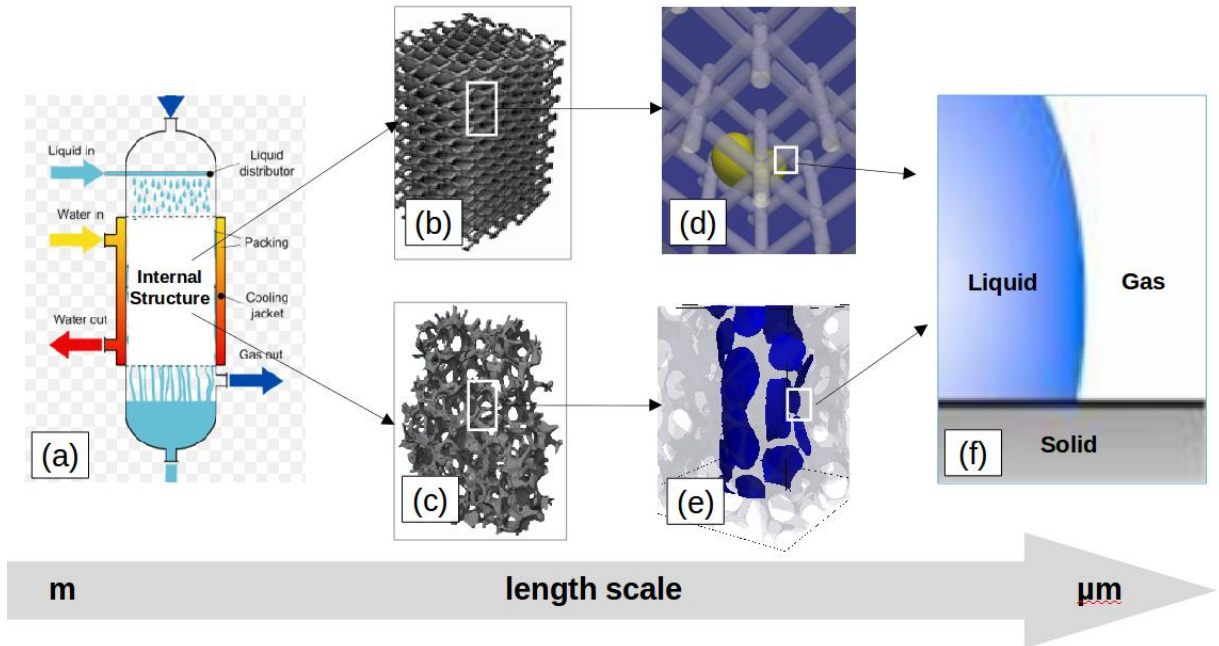


Figure 1.4: Inside-views into (a) structure-packed multiphase reactor of successively decreasing length scales: (b) periodic open-cell structure (POCS), (c) sponge (i.e. foam) structure, (d) rising bubble in a representative domain of POCS filled with liquid, (e) gas-liquid interfacial flow in a representative domain of sponge structure, (f) wetting phenomenon involving contact line where three phases meet together. Among the pictures here, (a) is redrawn from Pugliesi [14]; (b) and (c) are from Dietrich et al. [15].

1.2 Physical Fundamentals

1.2.1 Surface Tension

Physical understanding of wetting is based on that of surface tension. The surface tension can be viewed from two perspectives: thermodynamic or mechanical [16]. In the former, the surface tension arises due to intermolecular interactions at interface and thus is defined as the Gibbs free energy per surface area. In the latter point of view, it is considered as the resultant force per unit length owing to a normal stress anisotropy near interface.

A typical example of surface tension effect is the existence of a pressure jump across curved interfaces of a bubble or droplet. This pressure difference is referred to as Laplace pressure and determined by the Young-Laplace equation:

$$\Delta P = \sigma \left(\frac{1}{R_1} + \frac{1}{R_2} \right) \quad (1.1)$$

where σ is the surface tension coefficient and R_1 and R_2 are the principal curvature radii.

1.2.2 Surface Tension near Wall – Wetting

When the interface (curved due to gas-liquid surface tension) gets in contact with a solid surface, wetting phenomenon arises and the junction where the three phases (gas, liquid and solid) meet together is referred to as contact line (see Figure 1.5). The degree of wetting (i.e. wettability) is determined mechanically by a balance between adhesive and cohesive force: the former drives the liquid droplet to spread over the substrate while the latter causes it to maintain a spherical shape and thus minimize its contact with the substrate. The wettability is usually quantified by the equilibrium contact angle (θ_c) of the droplet at rest: $\theta_c = 0^\circ$ indicates complete (e.g. perfect) wetting while $\theta_c > 0^\circ$ means partial wetting. For the partial wetting case, the solid surfaces can be broadly classified into two types depending on θ_c : $\theta_c < 90^\circ$ amounts to a hydrophilic (or lyophilic for non-water droplet) surface while $\theta_c > 90^\circ$ indicates a hydrophobic (or lyophobic) surface.

For ideal surfaces (i.e. horizontal, smooth and homogeneous), the equilibrium contact angle is unique for a fixed system at a given temperature and pressure. Its value is related to surface tensions among the three phases by the Young equation [17]:

$$\cos \theta_c = \frac{\sigma_{GS} - \sigma_{LS}}{\sigma} \quad (1.2)$$

Therein σ_{GS} is the surface tension between gas and solid while σ_{LS} that between liquid and gas. σ is the surface tension between gas and liquid as introduced in Section 1.2.1. To avoid possible confusion frequently arising due to interchangeable use of the term

“surface” and “interface”, σ is hereinafter called as interfacial tension; in the remainder of the thesis, the term “surface” refers to the boundary between solid and a fluid phase (gas or liquid) while “interface” does to that between gas and liquid.

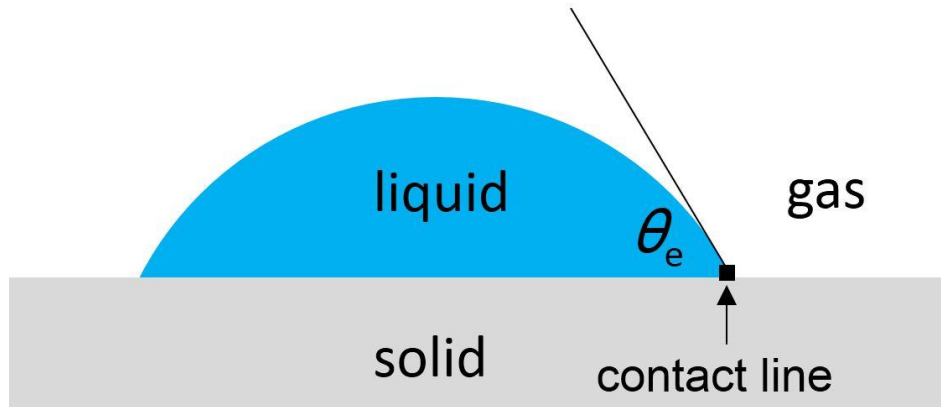


Figure 1.5: A liquid-droplet in ambient gas and resting on solid surface, with equilibrium contact angle θ_e . The “point” where the liquid-gas interface meets the solid surface is termed as contact line. It is noted that since here is a 2D lateral view, the black square dot indicating the contact line is not a point but truly a line in 3D reality.

Most solid surfaces in reality are non-ideal: they could be chemically or geometrically heterogeneous. Such heterogeneity gives rise to the so-called contact angle hysteresis, where the equilibrium contact angle appears within a range $\theta_r \leq \theta_e \leq \theta_a$ rather than as a unique value. Here θ_a and θ_r are referred to as advancing and receding contact angle; for a given system, they are maximum and minimum achievable contact angles respectively.

1.2.3 Contact Angles at Moving Contact Line – Scales, Scales, Scales ...

It will be much more complicated when one turns to consider dynamic wetting scenarios where contact line is moving with respect with solid substrate. It is insufficient to use only the equilibrium contact angle discussed above to characterize completely

moving contact line (MCL) problems, considering the intrinsic multi-scale nature. As Figure 1.6 shows, there are three length scales with three corresponding characteristic contact angles successively.

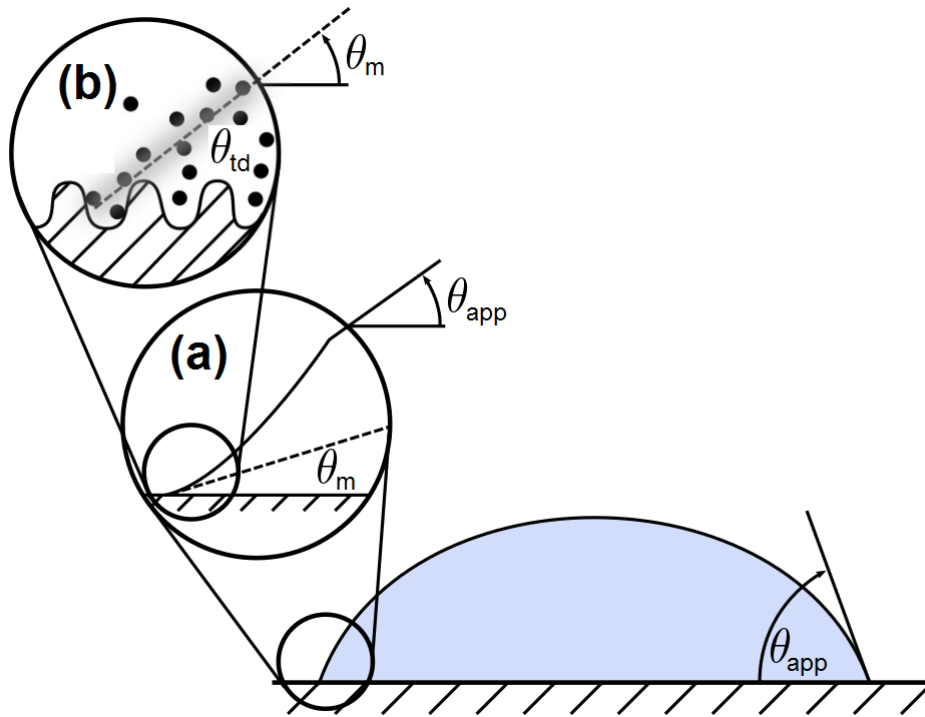


Figure 1.6: Macroscopic- (main panel), microscopic- (inset a) and molecular- (inset b) scale involved in moving contact line physics (adapted from Bonn et al. [1]).

1.2.3.1 Macroscopic Scale with Apparent Contact Angle

At this large scale (see the main panel of Figure 1.6), the flow problem is governed by the balance of gravity and capillarity (i.e. surface tension), assuming that inertial force is negligible. Thus the characteristic length scale here could be indicated by the capillary length $l_\sigma = \sqrt{\sigma/(\rho_L g)}$ that measures the relative importance of capillarity to gravity; in an air-water system at room temperature and pressure, for example, the capillary length is on the magnitude of 1 mm . At this macroscopic scale, we are usually interested in global geometric features such as droplet diameter or its height. With these large-scale

geometric dimensions, the apparent contact angle θ_{app} can be extracted. For example, θ_{app} in the main panel of Figure 1.6 might be estimated with the height and base diameter of the droplet cap, provided that capillary force dominates over gravitational force where the droplet is a spherical cap.

1.2.3.2 Microscopic Scale with Microscopic Contact Angle

If zooming in on a region whose dimension is much smaller than capillary length (see inset a in Figure 1.6), one arrives at the microscopic scale. At this scale, the balance between gravity and capillarity dominating the macroscopic scale is replaced by that between viscosity and capillarity; so viscous forces come into play. Due to the viscous effect one could observe fairly curved interface at the microscopic scale. This viscosity-induced curvature of the interface is well known as viscous bending phenomenon. The physical mechanism behind this bending behavior was revealed by the analytical solution from Huh and Scriven [18], who showed that viscous effects bring about a pressure around interface. This pressure must be balanced by the capillary pressure (i.e. the Laplace pressure) and thus a curved interface arises as implicated by Eq. (1.1). The microscopic contact angle θ_m is supposedly extracted from the tangent of the curved interface at the solid wall.

The microscopic length scale ranges from hundreds of nano-meter to tens of micro-meter. At this scale, Navier-Stokes-based continuum hydrodynamics is still valid at least for non-complex fluids [19]. If using continuum hydrodynamics principles for MCL problems at this scale, however, one will be faced up with a classical paradox between MCL and no-slip boundary condition at solid wall [18]. The latter leads to a stress singularity at MCL where continuum fluid mechanics breaks down. To circumvent the singularity, two approaches have been established and reported in literature. One method is to artificially remove molecular-scale-level region from hydrodynamics solution domain and the other is to modify boundary conditions for flow solutions by allowing for a slip

condition at contact line. Several pioneering scientists used the two approaches respectively to pursue theoretical insights into the microscopic scale MCL flow physics; in the following review, their names will be lined-up in chronological order of their breakthroughs.

In the former approach, we pay tributes to Hoffman, Voinov, Tanner and Cox. In 1975 Hoffman [20] derived a relation for microscopic contact angle with MCL velocity and apparent contact angle, by correlating experimental data from his investigation into the shape of liquid-air interface advancing in a glass capillary. One year later, Voinov [21] arrived at an analytical solution to contact angle in very close vicinity to solid wall; he showed that the contact angle varies logarithmically with the distance to the contact line. Such logarithmical variation of the contact angle in mathematics reflects viscous bending of the interface in physics; the latter had been identified and analyzed by Huh and Scriven [18] as discussed above. Since the solution by Voinov was obtained with lubrication approximation valid only for a quasi-parallel flow, it might apply to only MCL flows with very small contact angles. Based on the outcome of Voinov's work, Tanner [22] derived in 1979 that the time-dependence of spreading base radius follows $r(t) \sim t^{1/10}$, known as the Tanner law in literature. Considering its origin from the Voinov theory, the Tanner law works also only for very small contact angle scenarios. Such application limitation was removed in 1986 when Cox [23] generalized the Voinov solution to MCL flows with large contact angle, beyond the lubrication approximation. Since the Voinov solution can be viewed as the early prototype of the theory generalized by Cox, the latter is usually denoted as the Voinov-Cox law. Further details on this law will be given in Section 1.3.1.

In the latter approach that permits a slip at wall, we should remember Navier, Huh, Scriven and Dussan. In fact, human's insights into slip of flows at solid surface date back to 1823 when Navier [24] proposed a slip mechanism for single-phase gas flow over a substrate; yet it was until one and a half century later (in 1971) that Huh and Scriven [18]

utilized slip models to remove the stress singularity in MCL problems. Different slip models proposing different slip mechanisms could be found in literature. Nevertheless, Dussan [25] pointed out in 1979 that compared to the slip length, details of a particular slip mechanism are of little significance. Given its origin from Navier's work, the slip-based approach is usually referred to as the Navier slip boundary condition. Section 1.3.1 will elaborate on this boundary condition.

1.2.3.3 Molecular Scale with Thermodynamically-Equilibrium Contact Angle

At this molecular scale typically of a few nano-meters (see inset b in Figure 1.6), the Navier-Stokes-based continuum hydrodynamics breaks down and thus fails to describe the molecular interaction of MCL and solid substrate; molecular-kinetics theories with non-continuum philosophy are required. These theories will be briefly introduced in Section 1.3.2. The characteristic contact angle at this scale is intrinsically determined by thermodynamic equilibrium state; so the contact angle here is named as thermodynamically-equilibrium contact angle θ_{td} in the present thesis. θ_{td} is inherent to a specific thermodynamic system, thereby being independent of operating conditions such as contact line speed and flow geometries. It is noted that the thermodynamically-equilibrium contact angle θ_{td} is essentially the equilibrium contact angle θ_e that has been introduced in Section 1.2.2; the prefix "thermodynamically-" is added here to emphasize its thermodynamic nature and avoid any possible confusion with the microscopic contact angle.

Considering three different scales around MCL problems as introduced above, one must always take care to clearly distinguish them when he or she investigates the problems at his or her interesting scales, either analytically, experimentally, or numerically. Otherwise huge confusions would arise.

1.3 Theoretical Basics for Moving Contact Line Flow Problems

As introduced above, MCL flow problems involve three length scales. Among them, the macroscopic scale with the apparent contact angle is the most straightforward since large-scale dimensions of interest are readily accessible either in experiments or in continuum-based simulations. Thus, our attention will be paid to theoretical basics for the microscopic scale and molecular scale, namely, hydrodynamic theory for the former and molecular-kinetic theory for the latter.

1.3.1 Hydrodynamic Theory

As discussed in Section 1.2.3.2, the hydrodynamics approaches can be roughly categorized into two classes: one that carves out the tiny region near MCL from continuum hydrodynamics solution and the other that introduces a slip concept. The former is exemplified by the Voinov-Cox law and the latter is represented by the Navier slip boundary condition.

1.3.1.1 Voinov-Cox Law

Using the Voinov-Cox law [21, 23], one needs to choose a slip length at molecular scale where continuum hydrodynamics does not apply; the tiny region within this length is then cut away from the hydrodynamic solution domain. Hence, the large-scale flow outside the carved-out zone is still resolved by continuum mechanics while the effect of this microscopic zone on the macroscopic flow is sub-grid-like modelled by the following relation for the apparent contact angle θ_{app} and its microscopic counterpart θ_{m} [23]:

$$G(\theta_{\text{app}}, \lambda_{\mu}) = G(\theta_{\text{m}}, \lambda_{\mu}) + Ca_{\text{cl}} \ln(L / L_{\text{s}}) \quad (1.3)$$

where G is a complicated function in the following form:

$$G(\theta, \lambda_{\mu}) = \int_0^{\theta} \frac{d\theta}{f_{\text{Cox}}(\theta, \lambda_{\mu})} \quad (1.4)$$

with

$$f_{\text{Cox}}(\theta, \lambda_\mu) = \frac{2 \sin \theta \left\{ \lambda_\mu^2 (\theta^2 - \sin^2 \theta) + 2 \lambda_\mu \left[\theta(\pi - \theta) + \sin^2 \theta \right] + \left[(\pi - \theta)^2 - \sin^2 \theta \right] \right\}}{\lambda_\mu (\theta^2 - \sin^2 \theta) \left[(\pi - \theta) + \sin \theta \cos \theta \right] + \left[(\pi - \theta)^2 - \sin^2 \theta \right] (\theta - \sin \theta \cos \theta)} \quad (1.5)$$

The first thing to note here is that the Voinov-Cox law (or hydrodynamics theories in general) takes an assumption that the microscopic contact angle θ_m equals the (thermodynamically) equilibrium contact angle θ_e (i.e. θ_{id}). The assumption is said to be based on the so-called principle of Occam's razor (which states that among several competing hypotheses, the one with the fewest/simplest assumptions should be opted for) [26]. This assumption is valid for microscopic length scale near MCL if using hydrodynamics approach but not anymore for molecular scale.

In the Voinov-Cox law above, λ_μ is the viscosity ratio between gas and liquid. The contact line capillary number $Ca_{\text{cl}} = \mu_L U_{\text{cl}} / \sigma$ denotes the contact line velocity U_{cl} normalized by the liquid viscosity μ_L and interfacial tension σ . L is the characteristic macroscopic length scale which, for instance, may be chosen to equate to droplet diameter; L_s is the slip length used to indicate the tiny region near MCL, which is carved out from the continuum solution domain as discussed previously. With slip length L_s typically being of molecular size, $\ln(L/L_s)$ is roughly expected to be of the order of 10 [26]; such a large disparity occurs between the two length scales. Since only macroscopic phenomena at the larger length scale L are of interest for the current study as many others in literature, L_s is treated as an ad-hoc parameter that can be fitted to some benchmark theoretical or experimental data. For $\theta < 135^\circ$ and very small viscosity ratio $\lambda_\mu \rightarrow 0$, Eq. (1.3) can be simplified into:

$$\theta_{\text{app}}^3 = \theta_m^3 + 9Ca_{\text{cl}} \ln(L/L_s) \quad (1.6)$$

The cubic relation above had been confirmed by experiments reported in literature (e.g. [27, 28]) for contact angle up to $70^\circ \sim 100^\circ$ if the contact line capillary number $Ca_{\text{cl}} \ll 1$ and Reynolds number $Re_{\text{cl}} = \rho_L L U_{\text{cl}} / \mu_L \ll 1$.

1.3.1.2 Navier Slip Boundary Condition

In addition to the Voinov-Cox approach, another remedy for the contact line singularity is to relax no-slip boundary condition and thus allow for a slip at solid wall [25]. This relaxation is modelled by the Navier slip boundary condition:

$$U_{cl} = L_s \frac{\partial U}{\partial y}, \quad \text{at } y = 0 \quad (1.7)$$

Therein y is the coordinate normal to the wall. In numerical simulations, this Navier formulation for slip velocity is often used in combination with particular models for the microscopic contact angle θ_m ; under this occasion, θ_m is also called dynamic contact angle θ_d (not to be confused with the apparent contact angle θ_{app}) and accordingly these models are referred to as dynamic contact angle models in literature. Among various dynamic contact angle models, equating the dynamic contact angle θ_d to the equilibrium contact angle θ_e is the simplest one. It works for a relatively slow motion of contact line, but may fail as contact line speed U_{cl} is non-trivial. Under such a condition, one requires models that relate θ_d as a function of U_{cl} and θ_e . These can be exemplified by the Kistler model (see Chapter 6 by Kistler in Berg [29]).

By examining comparatively the corresponding formulation of the Voinov-Cox law and Navier slip boundary condition, one might find that in the Voinov-Cox law macroscopic flow phenomena parameterized by the apparent contact angle θ_{app} and contact line velocity U_{cl} are insensitive to the microscopic details (i.e. the slip length L_s), considering the logarithmic relation in Eq. (1.3) or Eq. (1.6). By comparison, the large-scale flow physics indicated by U_{cl} is rather sensitive to L_s in the Navier approach. Such contrasting features contribute to opposing pros and cons of each method. In the Voinov-Cox model, one may arrive at an accurate solution of the large-scale flow without detailed description of local behavior near the contact line; but this method may not apply if one wants to investigate microscopic dynamics since only large-scale flow physics is intended to be

resolved. On contrary, the Navier formulation requires a physical slip length; the physical slip length is usually under-resolved by even the finest mesh resolution of a feasible continuum-based computation aiming at resolving larger-scale flows. If using such an under-resolved slip length in simulations (e.g., based on Volume-of-Fluid method), the mesh spacing next to solid wall will take over the role of slip length and serve as a “numerical” slip length [30]. As a result, the numerical solution of macroscopic MCL behavior is always mesh-dependent unless special care is taken, for example, in Afkhami et al. [31] who applied a mesh-dependent numerical contact angle model derived with the Voinov-Cox law and then achieved mesh convergence. This downside of the Navier slip boundary condition for macroscopic process is compensated by its upside for microscopic behavior: it has been shown very useful for revealing the microscopic physical mechanism either in experiments [32] or molecular-dynamics simulations [33].

1.3.2 Molecular-Kinetic Theory

Here the concept is completely different from the hydrodynamic theory. Instead of being regarded as continuous media, fluids in the immediate neighborhood of the contact line are viewed to be made up of fluid particle (molecules) [26, 34]. The motion of contact line occurs owing to the thermally activated molecules jumping from one fluid phase to the other across the contact line and thus should be determined by statistical kinetics of molecules for the three-phase region (see inset b in Figure 1.6). Under this modeling framework, a driving force is believed to disturb the equilibrium of molecular displacements between gas and liquid phase. The driving force is supposed to be the so-called unbalanced Young force, i.e. $\sigma[\cos(\theta_{\text{id}}) - \cos(\theta_{\text{app}})]$. A simplified kinetic model can be expressed as follows:

$$U_{\text{cl}} = \frac{\sigma}{\xi} [\cos(\theta_{\text{id}}) - \cos(\theta_{\text{app}})] \quad (1.8)$$

Therein ξ is a constant related to thermodynamics of a specific system. Since further details concerning the molecular-kinetic theory are beyond the background scope of the current study, we are referred to [26, 34-36] for more information on this approach.

1.4 Numerical Simulations for Moving Contact Line: State-of-the-Art

This section reviews state-of-the-art numerical investigations for MCL problems in literature. Although molecular dynamics (MD) simulations are emerging in recent decades as a very effective tool to uncover molecular details of MCL [1, 26], only (quasi-) continuum simulations for macro- and micro-scale MCL behavior are introduced in this section. Even for this narrowed scope, the author does not intend to be all-inclusive; yet he does attempt to cover all the representative investigations on this area to the best of his knowledge. These numerical studies on MCL and wetting problems can be categorized according to their underlying numerical methods for interface-capturing.

1.4.1 Volume-of-Fluid (VOF) methods

VOF methods employ volume fraction F to denote individual phases and therewith capture interface [37]: $F = 1$ for liquid and $F = 0$ for gas, so the gas-liquid interface arises within mesh cells (also called “cut-cells”) where transition $0 < F < 1$ occurs. Depending on whether interface reconstruction is required for the transition region, VOF methods can be subdivided into two categories: Interface-Reconstruction VOF and Color-Function VOF [38]:

1.4.1.1 Interface-Reconstruction VOF (IR-VOF)

IR-VOF needs interface reconstruction for geometrical representation of the interface, as its name suggests. A representative example of state-of-the-art interface reconstruction schemes is the so-called Piecewise Linear Interface Calculation (PLIC); see Rudman [39] as well as Rider and Kothe [40]. In the IR-VOF category, the numerical

study by Renardy et al. [30] is a pioneering work. They showed that even with no-slip boundary condition, a numerical slip length relating to half a mesh spacing adjacent to wall is introduced inherently due to advection of F there. Hence, numerical results would almost always be mesh-dependent given that it is computationally prohibitive to reduce mesh cell size down to physical slip length of nanometer scale. To tackle the problem, Afkhami et al. [31] proposed a mesh-dependent numerical contact angle model using the Voinov-Cox law [23] and thereby gained numerical solutions that are converging with mesh refinement. With this contact angle model as well as by coupling flow field with energy equation, Fath and Bothe [41] investigated numerically thermo-capillary migration of a droplet on a solid wall, using the in-house VOF-based code Free Surface 3D (FS3D) [42, 43]. Besides, Fang et al. [44] studied contact angle hysteresis phenomena with their IR-VOF variant. For further examples in the IR-VOF class, we are referred to Alla et al. [45] and Malgarinos et al. [46], both of whom used ANSYS Fluent®.

1.4.1.2 Color-Function VOF (CF-VOF)

CF-VOF uses a smooth color function which is considered as an approximation of the volume fraction used in IR-VOF, so that geometrical interface reconstruction is not required. CF-VOF is also called algebraic VOF in literature. The iso-surface where $F = 0.5$ indicates interface location. In CF-VOF, the relief from interface reconstruction efforts comes at the cost of numerically diffuse interface, i.e. so called interface “smearing-out”, which leaves interface-capturing very inaccurate. Hence, almost all the CF-VOF implementations should be equipped with some special numerical techniques to counteract or “compress” the numerical smearing-out; see Wörner [38] for concrete examples.

The application of CF-VOF into MCL problems can be exemplified by several numerical studies: Legendre and co-workers [47, 48] carried out numerical simulations of spreading and sliding droplets with appropriate modelling of contact angle hysteresis

using their code JADIM. Both Saha and Mitra [49] as well as Linder et al. [50] employed *interFoam* (a standard OpenFOAM® solver based on CF-VOF) to simulate MCL-related flow phenomena with the implementation of corresponding dynamic contact models. In *interFoam* an artificial compression term is introduced into volume fraction equation to offset numerical interface diffusion [51].

1.4.2 Level-Set (LS) methods

LS methods use a signed distance function from the interface location for interface capturing. The sign is utilized to identify corresponding phases [52, 53]. With LS methods, Spelt and co-workers carried out a line-up of numerical simulations on droplet spreading phenomena [54-57]. Besides, Chen et al. [58] investigated numerically bubble formation on orifice. Further examples of using LS methods for MCL problems can be found in Park and Kang [59], Liu et al. [60], Zahedi et al. [61] and Lakehal et al. [62].

1.4.3 Front-Tracking (FT) methods

In FT methods, a discrete set of Lagrangian markers are used to track the interface [63]. Unlike VOF and LS methods, one could find in literature only a few numerical studies using FT methods for MCL problems: Manservisi and Scardovelli [64] as well as Muradoglu and Tasoglu [65] applied their respective FT methods to numerically reproduce droplet spreading process, with corresponding dynamic contact angle models.

1.4.4 Phase-Field (PF) methods

PF methods are diffuse-interface methods that treat interface between two immiscible fluids as a transition region of small but finite width, endowed with interfacial tension [66]; so PF-methods are also called in literature as diffuse-interface methods, highlighting their “diffuse-interface” as opposed to “sharp-interface” characteristics. Based on thermodynamics instead of mechanics, the PF methods can be traced to van der Waals

more than a century ago [67]. Originally employed to model the initial stages of spinodal decomposition [68], the PF methods have become popular in recent years as a numerical technique for simulating two-phase flows with a wide range of hydrodynamic and interfacial phenomena [69, 70].

In the context of MCL problems, the PF methods are believed to combine macro-, micro- and molecular-scales in a unified theoretical framework [71]. On one hand, it regularizes the stress singularity at solid wall by modelling contact line motion via a chemical-potential-induced diffusion mechanism [72]; this treatment is physically sound since mechanism behind MCL at molecular scale can be viewed as a diffusion process [16]. Therewith, the PF methods can model appropriately molecular-scale dynamics. On the other hand, microscopic- and macroscopic-scale flows and interfacial phenomena are resolved by the coupled Cahn-Hilliard (CH) and Navier-Stokes (NS) equation system. The mathematical formulation of the coupled CH and NS system will be given in Section 2.1.

Apart from the above advantage of dealing with MCL-focused flows, the PF methods have other merits. First from a computational view, handling an interface as a transitional layer of finite thickness greatly facilitates the numerical treatment of topological changes of the interface. Therefore, the PF methods have been successfully applied to simulate interfacial phenomena of singularity such as breakup and coalescence of droplets or bubbles [73-76]. Besides in the PF methods, the diffuse interface is treated in a physical rather than numerical sense. It is essentially different from other interface-capturing methods (e.g. the Color-Function Volume-of-Fluid and conservative Level-Set methods [77]) where the interface is numerically diffuse so that special care (e.g., interface compression or re-initialization) is required to maintain a proper interface diffusion. By contrast, these numerical efforts for diffuse interface regularization are saved in the PF methods. In addition, owing to the energy-based formulation, it is straightforward to use

the PF methods to describe interfacial dynamics and rheology in a unified framework when one studies two-phase flows of complex non-Newtonian fluids [74, 78, 79].

In terms of numerical solution procedures, PF simulations of MCL-related flow dynamics can be classified into two types: one based on Navier-Stokes (NS) equations and the other based on Lattice-Boltzmann Method (LBM):

1.4.4.1 NS-based PF Simulations

Like in other interface capturing methods introduced previously, NS equations are utilized to describe flow dynamics. For interface capturing, a transport equation for order parameter C (also called phase-field) is added and coupled with the NS equations. The transport equation for C appears as two variants: one being with a physically-motivated diffusion term (**Cahn-Hilliard Equation**) and the other being without such a term (**Allen-Cahn Equation**).

The majority of NS-based PF simulations in literature fall into the former category where Cahn-Hilliard (CH) equation governs the transport of C , so do the numerical investigations in this PhD study; the mathematical formulation will be given in Section 2.1.1. Here **Jacqmin** [72] is a pioneer who showed analytically the applicability of CH-based PF methods for MCL dynamics and derived asymptotic relation as sharp interface limit is approached. Since his work onward, PF methods of this type have been progressively employed for MCL problems by several research groups:

Wang and coworkers extended the equilibrium boundary condition from Jacqmin [72] to a general one (i.e. the so-called generalized Navier boundary conditions) by a variational approach based on Onsager's principles of minimum dissipation [80]. They showed that with the proposed boundary condition, one could reproduce the results from experiments [81] and from molecular dynamics simulations [82]. Using their numerical model, they also investigated contact line dynamics on chemically patterned surface [83],

three-component flow phenomena on solid surface [84] as well as droplet impacting a homogeneous substrate [85].

The research activities of **Amberg's** group on this area started with the work on fundamental wetting dynamics and generic sintering-like flows in a solid matrix [86]. Here they used equilibrium wetting conditions by a Neumann boundary condition for order parameter. Later on, they switched to non-equilibrium conditions prescribed by a partial differential equation and demonstrated that the non-equilibrium wetting condition is advantageous over its equilibrium counterpart in terms of accurately capturing rapid wetting dynamics [87, 88]. Their further computational investigations revealing local mechanism of wetting dynamics can be found in Carlson et al. [89, 90] and their recent extension into non-Newtonian droplet wetting is reported in Wang et al. [79].

The group of **Anderson** are the first numerical modelers who applied NS-based PF methods into simulations of droplet impacting solid surface [91]. Besides, they studied capillary-driven spreading of a droplet without impact [92]. Their further contribution to this area can be shown by the analytical efforts on scaling laws of PF methods [93]. Therein they pointed out that it is crucial to choose an appropriate mobility in accordance to artificially enlarged thickness of interface so that macroscopic flow physics can still be accurately reproduced.

The research group key-figured by **Yue and Feng** set out their endeavor on MCL dynamics with a combined analytical and numerical study on sharp-interface limit of CH-based PF methods [94], following their extensive PF simulations of various Newtonian and non-Newtonian interfacial flows problems [74, 78, 95-98]. They showed that the sharp-interface limit could be approached when interfacial thickness is smaller than a threshold value while other model parameters are kept fixed. More significantly, they demonstrated a clear connection between CH-based PF methods and Voinov-Cox law-based sharp-interface methods by relating the diffusion length in the former with the slip

length in the latter. Shortly later, they extended the investigation into wall energy relaxation of the CH model [71, 99]; such an energy relaxation is reflected by a non-equilibrium wetting condition modelled with a partial differential equation of the order parameter (similar to [88]). They showed that the wall energy relaxation gives rise to a microscopic dynamic contact angle that deviates from the equilibrium one, and revealed a competition mechanism between the wall energy relaxation and CH diffusion. By making use of this competition, one might accurately reproduce macroscopic flow dynamics at a reduced computational cost. Further numerical achievements by this group on MCL-related flows can be exemplified by their PF simulations of dynamic wetting of Newtonian and viscoelastic fluids [78, 98] as well as moving and coalescing behavior of droplets driven by substrate wetting gradient and external flows [76].

Ding and coworkers performed comprehensive NS-PF-based numerical simulations of droplet spreading and motions [55, 100-103] using their in-house code with an innovative numerical treatment of large density contrast between two phases [104]. One feature worth noting about their phase-field modelling and simulations is that for microscopic contact angle imposed at wall, they adopt a geometrical formulation [100] rather than surface energy formulation used by other research groups reported previously. The use of the geometrical formulation facilitates application of the NS-PF methods into contact angle hysteresis-related scenarios since it makes straightforward implementation of a contact angle hysteresis window [101]. Recently, they also expanded their working scope into three-component fluid flows involving MCL problems [105].

The other flavor of the C transport equation arises as the Allen-Cahn (AC) equation. The difference of AC-based method from CH-based counterpart is that the former does not have a diffusion term used by the latter to physically describe MCL. Therefore although AC-based PF methods have been extensively employed for a variety of multiphase system [106-108] and interfacial flow problems [109], a few studies can be found in

literature on its application into wetting-related phenomena. Ben Said and coworkers performed simulations of wetting phenomena of compound droplets on solid surface [110] and on fibers [111], with their in-house AC-based PF code. Therein they numerically reproduced multi-droplet systems only in an equilibrium state but no physical wetting process/MCL dynamics. As of now, the numerical work by Badillo [112] might be the only one who applied AC-based PF methods into wetting dynamics problems, to the best of the author's knowledge.

1.4.4.2 Lattice Boltzmann Method (LBM)-based PF Methods

LBM is emerging in recent decades as a popular alternative to conventional NS-based CFD approaches, see e.g. [113-115], considering its suitability for massively parallel computation deployment at high performance computers, among other merits. Instead of taking continuum assumptions, LBM treats fluid consisting of fictive particles and solves the discrete Boltzmann equation with collision models for these particles for fluid flow simulations. The application of LBM-based PF methods into MCL problems was initiated by Chen et al. [116] who studied MCL-related two-phase hydrodynamics under shear flow. Later, Yeomans and co-workers performed very extensive LBM-based PF simulations ranging from local hydrodynamics of MCL [117-120] to droplet spreading and motions on heterogeneous substrates being either chemically-patterned [121-127] or geometrically-patterned [128-134].

1.5 Objectives and Contributions of This Study

The goal of this PhD study can be subdivided into the following four objectives; its contributions to the scientific community can be categorized into the four corresponding aspects as well.

1.5.1 Method Development and Numerical Implementation

The starting-point/base of this PhD work lies in development of an interface-capturing method for two-phase interfacial flows over solid surface (especially, moving contact line problem among others). Here the NS-CH-formulated phase-field method (PFM) is adopted in this study. The start-of-the-art NS-CH-based PFM simulations by other research groups have been reviewed in Section 1.4.4.1; their underlying mathematical formulations are to be presented in Section 2.1.

The NS-CH-based PFM is implemented in foam-extend, a community-driven fork of OpenFOAM®. The implementation efforts have been pursued jointly by Marschall (main developer) and the author of the present PhD thesis. The achievement is – among others – a novel customized top-level solver *phaseFieldFoam* [135, 136], whose capabilities have been shown for a variety of wetting-related processes [137-142]. The purpose of implementing the PFM in the open-source CFD software OpenFOAM® lies in the plan that the newly-developed solver *phaseFieldFoam* will be released freely under the GNU General Public License at an appropriate time; therewith fluid mechanical/chemical engineers will be able to use the code to solve a wide range of interfacial flow or wetting-related processes. This is especially critical for those interested in PFM modeling and simulations for their problems, given that all the PFM simulations by other researchers (reviewed in Section 1.4.4.1) were carried out in their respective in-house codes; this might impede widespread (re-)use of their codes by the scientific community. Under this context, the scientific contribution by the present work stands out.

1.5.2 Droplet Wetting on Homogenous/Heterogeneous Surfaces

The aim of this topic is to simulate droplet wetting phenomena on solid surfaces in a reliable, accurate and efficient manner. As discussed in Section 1.1, precise control of micro-droplets in terms of their locations, motions and shapes is of paramount importance

for process design and optimization in fundamental and application-oriented research as well as industrial practice on areas such as micro-fluidics device, micro-reactor, lab-on-a-chip system, etc. It is beneficial to be equipped with a reliable numerical model that provides accurate access to wetting phenomena. In many circumstances, such a numerical model is not just helpful but even critical for, e.g., virtual-prototyping hundreds of design and optimization alternatives before production as well as gaining deep insights into local physics that is challenging or simply too expensive to access experimentally.

With the PFM-based *phaseFieldFoam*, a reliable numerical model for micro-droplet wetting phenomena is successfully developed and built. Its predictive capability is demonstrated by accurate simulations of a variety of droplet spreading processes on solid substrates of chemical homogeneity/heterogeneity. The numerical results agree well with corresponding analytical solutions, experimental and computational data from literature. Besides, first 3D FVM-based PFM simulations with near-interface adaptive mesh refinement are pursued in the present contribution to exploit potentials for higher computational efficiency. These will be shown in Chapter 4.

1.5.3 Bubble Motion in Periodic Open Cellular Structure (POCS)

As introduced in Section 1.1, POCS is a novel internal packing approach for innovative multiphase structured catalysts and reactors. Exploration into the utilization of POCS for bubble column reactors is one theme in the German Helmholtz Energy Alliance “Energy Efficient Chemical Multiphase Process” [143], where the present PhD work belongs. In order to better understand moving/deforming behavior of individual bubbles within POCS, high-fidelity computational investigations – alongside with experimental measurements – are of equal significance for obtaining complementary or even unprecedented insights. Such trustworthy computations are only possible with a reliable numerical model. Under this context stands the purpose of the present study: it is devoted to developing such a

high-quality numerical model for predicting hydrodynamic behavior of bubble interacting with POCS and – based on the numerical model – exploring hydrodynamics conditions beneficial to mass transfer enhancement and surface catalytic reaction.

The present study starts the development of the numerical model with the method/code validation for single air-bubble rising in a viscous quiescent liquid. In terms of bubble terminal velocity and instantaneous bubble break-up process by a solid cylinder, the numerical model-delivered results are found to be in good match with experimental data from literature. Then the numerical model is applied to predict rising process of an air bubble through a representative domain of a POCS filled with stagnant water. Solid surface wettability (i.e. equilibrium contact angle) is an input parameter to the numerical model and is varied in a series of simulations to reveal its effect on bubble interacting behavior with the solid structures. The present results provide a clear evidence that bubble deformation and rising path largely depend on the wettability. In the circumstances of industrial application of POCS, therefore, the use of structures with high surface wettability (i.e. low equilibrium contact angle) is expected to favor mass transfer enhancement and catalytic gas-liquid reactions.

1.5.4 Gas-Liquid Interfacial Flow in Sponge Structure

In addition to POCS, sponge (i.e. foam) structure as internal structured packing is also a research topic in the German Helmholtz Energy Alliance “Energy Efficient Chemical Multiphase Process” [143]. One may find in literature extensive numerical models and simulations for gas-liquid two-phase hydrodynamics in sponge structure. However, most of these computational studies are based on scale-reduced method where averaging procedure is carried out. They are able to describe macroscopically effective quantities such as phase holdup and pressure drop but – intrinsically – not to resolve local scales, like, topology of gas-liquid interface. Until so far, no numerical model/simulation aimed at

interface-resolving of gas-liquid flow in sponge structure has been reported in literature. The present contribution serves as a first attempt to fill the gap.

For this purpose, a numerical model is developed in this study. Its predictive capability for hydrodynamics in sponge structure is firstly validated by considering gas-flow through alumina sponge. Therein the present computational results appear to be in good agreement with experimental/numerical data from literature. The numerical model is then utilized for interface-resolving simulations of gas-liquid flows within a representative elementary volume (REV); this is based on a modeling strategy combining pressure decomposition in Navier-Stokes equation and mirroring procedure applied to the REV. One contribution of the present work is that it shows the possibility of interface-resolving simulation for two-phase flow in sponge structure at a feasible computational cost. By the investigation into the effect of surface wettability and interfacial tension on gas-liquid interfacial area, the numerical results suggest property-tuning approaches to enlarge interfacial area and thereby increase interfacial mass transfer rate.

1.6 Thesis Outline

The thesis has so far reviewed physical and theoretical fundamentals as well as start-of-the-art numerical simulations of wetting process and moving contact line. The remainder of this thesis is organized as follows. The mathematical formulation of the phase-field method and its numerical implementation in OpenFOAM® are described in Chapter 2. Chapter 3 presents the code verification for some fundamental interfacial phenomena. In the following chapters, the thesis will elaborate on phase-field simulations of three application-oriented wetting scenarios, namely, liquid droplet spreading on homogenous and chemically-heterogeneous surfaces (see Chapter 4), air bubble (immersed in liquid phase) rising and interacting with periodic cellular structure (see

Chapter 5) and gas-liquid interfacial flows in a representative domain of sponge structure (see Chapter 6). Chapter 7 provides summaries and outlooks.

2 Mathematical Formulation and Numerical Methodology

This chapter introduces the mathematical formulation of the phase-field method (PFM), i.e., the coupled Cahn-Hilliard and Navier-Stokes equations system. Then the chapter briefly presents the PFM implementation using foam-extend – a community-driven fork of OpenFOAM®.

2.1 Governing Equations

2.1.1 Convective Cahn-Hilliard Equation

In the phase-field method, the distribution of the liquid (L) and gas (G) phase is indicated by an order parameter C ; C is also called as phase-field variable. Here, C takes respective values $C_L=1$ and $C_G=-1$ for corresponding bulk phases and varies rapidly but smoothly in a transition layer (that is, the physically-motivated diffuse interface). The thermodynamics of the binary fluid system can be described by the following mixing energy density [74, 144]:

$$f_{\text{mix}} = \frac{1}{2} \lambda |\nabla C|^2 + \frac{\lambda}{4\epsilon} (C^2 - 1)^2 \quad (2.1)$$

Then the mixing energy of this system can be expressed as follows:

$$F_{\text{mix}} = \int_V f_{\text{mix}} \, dV \quad (2.2)$$

where V is the system domain. On the right-hand-side of Eq. (2.1), the first and second term represent the interfacial and bulk energy density respectively. λ is the mixing energy density parameter; ϵ is called as the mean-field thickness or capillary width, and it is indicative of the thickness of diffuse interface. The chemical potential ϕ is defined as the variational derivative of the mixing energy F_{mix} with respect to the order parameter:

$$\phi = \frac{\delta F_{\text{mix}}}{\delta C} = \frac{\lambda}{\epsilon^2} C(C^2 - 1) - \lambda \nabla^2 C \quad (2.3)$$

The equilibrium state of the system is obtained by minimizing F_{mix} , i.e., solving the equation $\phi(C)=0$. Its solutions are $C_L=1$ and $C_G=-1$ that represent the two bulk phases respectively, as well as a one-dimensional profile (e.g. along x direction) across the interface:

$$C_e = \tanh\left(\frac{x}{\sqrt{2}\varepsilon}\right) \quad (2.4)$$

Following Jacqmin [66], one defines the interface width L_c as the distance from $C=-0.9$ to $C=0.9$, so that $L_c = 2\sqrt{2}\varepsilon \tanh^{-1}(0.9) \approx 4.164\varepsilon$; the interface width L_c contains 98.5% of the surface tension stress. Both L_c and ε can be used to indicate the thickness of a diffuse interface. It is noted that the diffuse interface parameterized by L_c or ε arises in a physical sense rather than owing to numerical reasons as discussed in Section 1.4.4; therefore an adequate grid resolution for the interface thickness is critical for reliable numerical simulations. This issue will be examined as to corresponding interfacial flow problems in the remainder of this thesis.

In equilibrium, the interfacial tension σ can be expressed as the integral of the free energy density across the interface [145]:

$$\sigma = \alpha \int_{-\infty}^{\infty} \left(\frac{dC_e}{dx}\right)^2 dx = \frac{2\sqrt{2}}{3} \frac{\lambda}{\varepsilon} \quad (2.5)$$

Cahn and Hilliard [144, 146] extended the steady-state problem above to a transient one by approximating diffusive flux to be proportional to chemical potential gradient. The transient problem is modelled by the convective Cahn-Hilliard (CH) equation as follows:

$$\frac{\partial C}{\partial t} + (\mathbf{u} \cdot \nabla)C = \kappa \nabla^2 \phi \quad (2.6)$$

Here t denotes time, \mathbf{u} the velocity field and κ the CH mobility. The term on the right-hand-side of Eq. (2.6) represents a diffusive process of contact line motion at solid walls. With the assumption of the wall free energy being at local equilibrium, one derives a

wetting boundary condition to take into account the solid surface wettability as follows [86]:

$$\hat{\mathbf{n}}_s \cdot \nabla C = \frac{\sqrt{2}}{2} \frac{\cos \theta_e}{\varepsilon} (1 - C^2) \quad (2.7)$$

θ_e is the equilibrium contact angle and $\hat{\mathbf{n}}_s$ is the outward pointing unit normal to the solid wall.

2.1.2 Navier-Stokes Equations

The present PhD study concerns two-phase flows of immiscible, incompressible, isothermal and Newtonian fluids. Hence, one can describe two-phase flows by the following single-field Navier-Stokes (NS) equations:

$$\nabla \cdot \mathbf{u} = 0 \quad (2.8)$$

$$\rho_c \left(\frac{\partial \mathbf{u}}{\partial t} + (\mathbf{u} \cdot \nabla) \mathbf{u} \right) = -\nabla p + \nabla \cdot \left[\mu_c (\nabla \mathbf{u} + (\nabla \mathbf{u})^T) \right] + \mathbf{f}_\sigma + \rho_c \mathbf{g} \quad (2.9)$$

where p is the pressure and \mathbf{g} the gravity vector. For the interfacial tension term \mathbf{f}_σ , two formulations exist in literature: one formed with conventional continuum surface force (CSF) [147] and the other based on chemical potential (CP) [66]. He and Kasagi [148] carried out a comparative study on the two interfacial tension formulations by investigating single bubble flow problems; they showed that the CP formulation is superior to the CSF counterpart in the sense that the former can reduce the magnitude of parasitic currents to the level of truncation error while the latter brings about non-trivial parasitic currents which could even destroy the flow at small capillary number. Hence, this PhD study adopts the CP-based form which expresses the interfacial tension as:

$$\mathbf{f}_\sigma = -C \nabla \phi \quad (2.10)$$

Besides, the density and viscosity field in Eq. (2.9) are also related to the order parameter:

$$\rho_c = \frac{1+C}{2} \rho_L + \frac{1-C}{2} \rho_G \quad (2.11)$$

$$\mu_c = \frac{1+C}{2} \mu_L + \frac{1-C}{2} \mu_G \quad (2.12)$$

where $\rho_{L/G}$ and $\mu_{L/G}$ indicate the density and viscosity of the bulk phases. Eqs. (2.10), (2.11) and (2.12) couple the NS Eq. (2.9) with the CH Eq. (2.6).

2.1.3 Dimensionless Formulation

To achieve a non-dimensional formulation of the coupled CH-NS equations system above, the following dimensionless variables are defined:

$$x^* = \frac{x}{L}, \quad u^* = \frac{u}{U}, \quad t^* = \frac{tU}{L}, \quad p^* = \frac{pL}{\mu_L U}, \quad \rho^* = \frac{\rho}{\rho_L}, \quad \mu^* = \frac{\mu}{\mu_L} \quad (2.13)$$

Therein L and U denote characteristic length and velocity scale respectively. Dropping the asterisks, one arrives at a dimensionless equation system as follows:

The chemical potential field is then:

$$\phi = C^3 - C - Cn^2 \nabla^2 C \quad (2.14)$$

The convective Cahn-Hilliard equation reads:

$$\frac{\partial C}{\partial t} + (\mathbf{u} \cdot \nabla) C = \frac{1}{Pe_c} \nabla^2 \phi \quad (2.15)$$

with the wetting boundary condition of C :

$$\hat{\mathbf{n}}_s \cdot \nabla C = \frac{\sqrt{2} \cos \theta_e}{2Cn} (1 - C^2) \quad (2.16)$$

The non-dimensional form of the Navier-Stokes equations is:

$$\nabla \cdot \mathbf{u} = 0 \quad (2.17)$$

$$\rho_c Re \left(\frac{\partial \mathbf{u}}{\partial \tau} + (\mathbf{u} \cdot \nabla) \mathbf{u} \right) = -\nabla P + \nabla \cdot \left[\mu_c \left(\nabla \mathbf{u} + (\nabla \mathbf{u})^T \right) \right] + \mathbf{f}_{st} + \mathbf{f}_b \quad (2.18)$$

with the density and viscosity field:

$$\rho_c = \frac{1}{2} \left((C+1) - \frac{\rho_G}{\rho_L} (C-1) \right) \quad (2.19)$$

$$\mu_c = \frac{1}{2} \left((C+1) - \frac{\mu_G}{\mu_L} (C-1) \right) \quad (2.20)$$

and the interfacial tension and buoyance force:

$$\mathbf{f}_{\text{st}} = -\frac{1}{Ca \cdot Cn} C \nabla \phi(C) \quad (2.21)$$

$$\mathbf{f}_{\text{b}} = -\frac{1}{2} \frac{Eo}{Ca} (C+1) \hat{\mathbf{e}}_z \quad (2.22)$$

The above non-dimensional system involves five dimensionless groups:

$$Re = \frac{\rho_L LU}{\mu_L}, \quad Ca = \frac{2\sqrt{2}\mu_L U}{3\sigma}, \quad Eo = \frac{(\rho_L - \rho_G)gL^2}{\sigma}, \quad Cn = \frac{\varepsilon}{L}, \quad Pe_c = \frac{2\sqrt{2}LU\varepsilon}{3\kappa\sigma} \quad (2.23)$$

The first three are physical ones: the Reynolds number Re stands for the ratio between inertial and viscous force, the capillary number Ca for the relative importance of viscous to capillary force and the Eötvös number Eo for that of buoyance to capillary force. The other two are model parameters specific to the phase-field method: the Cahn number Cn relates the capillary width to reference length scale and the Peclet number Pe_c serves as a measure of the ratio between the convection and diffusion of the order parameter. Among these dimensionless groups Re , Ca and Eo are fairly straightforward to determine from fluid and interfacial properties as well as operating conditions; but subtlety (even puzzlement among fluid mechanics scientists and engineers) arises as to the choice of Cn and Pe_c (equivalently, ε and κ). Towards this issue, the next subsection gives macro-scale-oriented answers.

2.1.4 Considerations for Choosing ε and κ

The question on determining ε and κ might be the subtlest issue in phase-field modeling for macro-scale flow problems; this statement is limited to “for macro-scale flow problems” since phase-field modelling is rather straightforward for microscopic phenomena.

In reality, macroscopically immiscible interface is actually on-molecular-scale miscible (i.e. diffuse) with a certain amount of mixing between two phases and thereby with a non-zero thickness, according to the deep insights of van der Waals [67] back in the 19th

Century. The interfacial thickness is typically on the order of tens of nanometers. In microscopic processes such as phase transition and critical phenomena [149, 150] as well as alloy solidification [151, 152], it is of primary importance to capture local interfacial dynamics. In such a system, characteristic length scale is either roughly the same order-of-magnitude or just by a few orders-of-magnitude larger than the interfacial thickness; thus it is fairly feasible for numerical simulations to integrate all the scales of interest. However, for rather large-scale (e.g. from tens of micrometers to a few of millimeters) processes where global features (such as droplet/bubble diameter) are of interest, it is computationally prohibitive to resolve both macroscopic and interfacial thickness scales, whose disparity in order-of-magnitude can be up to 6. In short, the crux lies in a conflict between physically-thin interface and computationally-unaffordable cost.

A common practice to circumvent the above problem is to use an artificially thicker interface than its truly physical value for modelling and simulation of macroscopic interfacial phenomena. So comes the first question: how thicker interface ε is allowed so that numerical solution of large-scale flows and interfacial dynamics is still independent of ε ? Another issue is about the mobility factor κ . It quantifies the CH diffusion process that governs the motion of contact line, as Eq. (2.6) implies; characteristic length of this diffusion is on molecular scale and thus a sufficient mesh resolution for it is beyond currently available computational capacities. Hence κ is treated as a phenomenological parameter that “coarse-grains” the molecular diffusion process in a sub-grid manner. Then another question arises: how to choose such an appropriate κ that macroscopic flow and interfacial phenomena can still be properly modeled and accurately reproduced?

Since the focus of this PhD study is on interfacial phenomena at macroscopic/global scale (e.g., bubble/droplet diameter scale), it handles pragmatically the above two questions:

The choice of the capillary width ε is made in accordance with reference length scale L characteristic of a certain interfacial flow problem under consideration. The experiences from the author and coworkers [137, 138, 142] as well as other research groups [86, 92] suggest that if ε is chosen such that $Cn := \varepsilon/L \leq 0.01 \sim 0.02$, then the simulated interfacial dynamics at the scale L gets rather insensitive to ε .

The value-fixing procedure for the phenomenological κ starts with a preliminary estimate following the relation $\kappa = \varepsilon^2$. As Jacqmin [66] showed, $\kappa = O(\varepsilon^2)$ ensures that the CH diffusion approaches zero as ε goes to zero, that is, conventional sharp-interface model could be properly recovered. A dimensionless version of this relation (parameterized by Cn and Pe_c) was already adopted by Ding et al. [102]. Around this first estimate, κ is finally chosen by fitting with, if available, certain experimental or analytical data, since κ may be viewed as a material property characteristic of a specific physical system [71].

2.2 Numerical Methodology

2.2.1 Implementation Platform – OpenFOAM®

All the method implementation works as well as subsequent simulations in this PhD study are carried out on the platform of OpenFOAM®. OpenFOAM® (for “Open-source Field Operation And Manipulation”) is primarily an open-source C++ toolbox for solving continuum mechanics problems, mostly for fluid dynamics and transport phenomena. Originally named as “FOAM”, OpenFOAM® was developed principally by Weller and Jasak [153, 154], both of whom were back then working at Imperial College, London. OpenFOAM® offers an extensive portfolio of solvers for a wide range of physical processes from turbulence, heat transfer, combustion and (multiphase/complex) fluid flows to molecular dynamics, solid mechanics, electromagnetics and acoustics. The code utilizes Finite Volume Method (FVM) for discretization and is equipped with unstructured

polyhedral grid capabilities. For further details concerning the underlying numerical methodologies of OpenFOAM®, one is referred to the official OpenFOAM® guides for users [155] and programmers [156] as well as a series of PhD theses by Jasak [157], Ubbink [158], Rusche [159] and Marschall [160].

Among dozens of forks and adaptations of OpenFOAM®, the foam-extend project is a global community-driven one that welcomes and integrates contributions from developers and users worldwide [161]; the project was previously known as OpenFOAM-extend (Note: OpenFOAM® is a registered trademark of ESI Group. OpenFOAM-extend and foam-extend are a community effort not endorsed by ESI Group). In the present PhD thesis, the implementation of the phase-field method and its application into numerical simulations are performed with foam-extend.

2.2.2 Numerical Implementation of Phase-Field Method

The development and implementation of phase-field method in foam-extend are carried out jointly by Marschall (main developer) and the author of the present PhD thesis. The fruit of the collaboration is a novel top-level solver *phaseFieldFoam* [135, 136], whose capabilities have been shown for a variety of wetting-related processes [137-142].

The solver *phaseFieldFoam* is equipped with two options for solution procedure of the Cahn-Hilliard (CH) equation from time-step n to $n+1$: segregated and coupled. In a **segregated** manner, the solution procedure within a single time-step can be summed up as follows:

- [1] Solve the CH equation (see Eq. (2.6)) to obtain the order parameter field at time-step $n+1$.
- [2] Update the chemical potential (see Eq. (2.3)) using the order parameter obtained from the step [1].

- [3] Calculate the interfacial tension by Eq. (2.10), mixture density by Eq. (2.11) and mixture viscosity by Eq. (2.12).
- [4] Solve the Navier-Stokes equations (see Eqs. (2.8) and (2.9)) for the velocity field at time-step $n+1$.

Alternatively, the solution procedure can proceed in a **coupled** manner; there rather strict limitations on time-step size will be relaxed and thus higher computational efficiency be achieved. Compared to the steps in the segregated manner, step (3) and (4) remain while step (1) and (2) merge into a single one. In this single step, the chemical potential ϕ is no longer used as an intermediate variable; rather, ϕ expressed by Eq. (2.3) is substituted into the CH equation (2.6). Then the CH equation of the 4th order derivative is formulated and then numerically solved as a whole. Therein the 4th order CH equation is divided into two Helmholtz-type equations and then solved simultaneously within one linear solver sweep; similar numerical procedures were already used by Yue et al. [74] and Dong [162].

Besides the solver *phaseFieldFoam* is endowed with other start-of-the-art numerical techniques for mass conservation, numerical boundedness and computational efficiency. Similar to Ding et al. [104] and Abels et al. [163], a relative density flux term owing to diffusion of two phases is added into the momentum equation to fulfil volume conservation for two-phase flows with a large density difference. Besides, if the segregated solution is chosen, a temporal sub-cycling is switched on where the CH equation is solved with more than one sub-time-step within a single time-step. This feature is similar to what the standard OpenFOAM[®] solver *interFoam* has for the volume fraction equation [155]. For further numerical details about *phaseFieldFoam*, one is referred to Marschall et al. [135, 136].

All the simulations reported by this thesis are equipped with the following numerical schemes. Spatial derivative is handled by a high resolution scheme (Gauss Gamma) and

time integration by a 2nd order two-time level backward scheme (Gear's method). The time step is adaptively set during simulations where the maximum Courant number is fixed to 0.1. For details on the adaptive time step control in OpenFOAM®, one is referred to Berberović et al. [164]. The coupling between velocity and pressure is dealt with by the Pressure Implicit with Splitting of Operators (PISO) algorithm [165].

2.3 Summary of Chapter 2

In this chapter, the governing mathematical equations of the PFM are introduced. Special care is taken for choice of the capillary width ε and mobility κ . Besides the method implementation in foam-extend is shortly introduced. Verification of the implementation is to be shown in the subsequent Chapter 3.

3 Verification for Fundamental Interfacial Phenomena

In this chapter, *phaseFieldFoam* is verified for some fundamental interfacial phenomena against corresponding analytical solutions; its predictive capability is therewith demonstrated for elementary interfacial or capillary-driven flow problems. The results and figures presented in this chapter have been published in Cai et al. [137, 142].

3.1 Phase-Field Diffusion

Owing to the free energy formulation, the CH diffusion consists of in-total fourth order derivative; see Eqs. (2.3) and (2.6). This is rather unusual for typical fluid mechanics and transport phenomena problems and therefore has not yet been handled by OpenFOAM® or its forks. Hence the implementation of this diffusion term in this study is to be verified here. For this purpose, a 1D test-case will be performed for a flat interface where the following CH equation without the convection term is solved:

$$\frac{\partial C}{\partial t} = \nabla^2 (C^3 - C - Cn^2 \nabla^2 C) \quad (3.1)$$

The numerical results for steady state will be compared with the corresponding analytical solution expressed in the following dimensionless form of Eq. (2.4):

$$C = \tanh\left(\frac{x}{\sqrt{2}Cn}\right) \quad (3.2)$$

The simulations are carried out in a 1D domain of dimensionless length 1 with varying grid resolutions (i.e., different dimensionless cell size h) of $h=0.02$, $h=0.01$ and $h=0.005$. With dimensionless thickness of the interfacial region $\varepsilon = 0.04164$, these mesh resolutions correspond to the number of cells for the diffuse interface region $N_C = \varepsilon/\Delta x$ being $N_C = 2$, 4 and 8. At both end of the 1D domain, zero gradient boundary conditions are used for the order parameter C . As depicted in Figure 3.1, a good march between the numerical and analytical solution can be fulfilled provided $N_C \geq 4$.

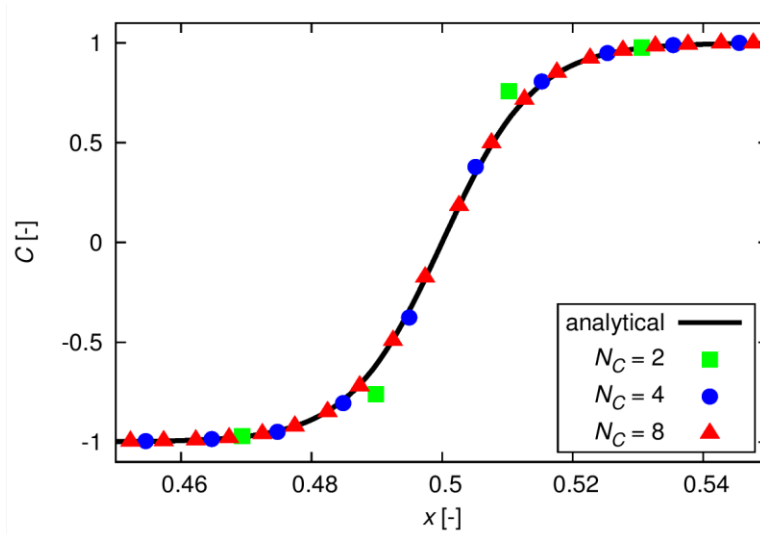


Figure 3.1: Analytical and simulated order parameter C profile across the diffuse interface with differing mesh resolutions. The Cahn number is $Cn = 0.01$. Adapted from Cai et al. [142].

Next, the verification goes further to a 2D test case. At all the boundary patches, zero gradient conditions are applied for C . Physically, the order parameter C should be $-1 \leq C \leq 1$, as introduced in Section 2.1.1. However, the 2D simulation made in the present study delivers an order parameter field ranging in $[-1 + \Delta C, 1 + \Delta C]$ with a shift of $\Delta C = 0.0052$; see Figure 3.2.

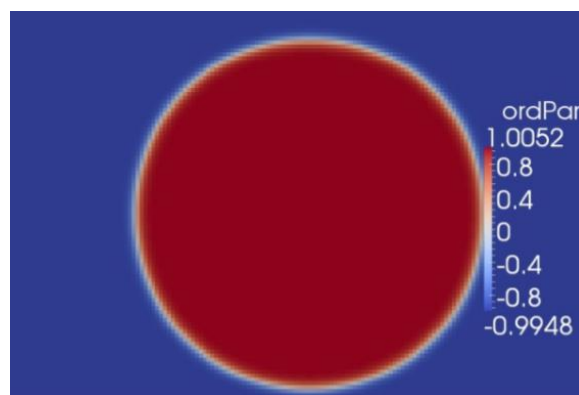


Figure 3.2: Order parameter field (shown as “ordPar”) from the 2D PF simulation with $Cn = 0.01$, $N_C = 4$ and $N_D = 100$. Taken from Cai et al. [142].

By the theoretical analysis of Yue et al. [97], such bound shifts were found to be intrinsic to 2D or 3D phase-field mathematical modeling, thereby being independent of numerical implementations or solution procedures. For a 2D problem, Yue et al. [97] related the shift ΔC to the Cahn number Cn as follows:

$$\Delta C = \frac{\sqrt{2}}{3} Cn \quad (3.3)$$

To verify the code against the analytical estimate above, numerical simulations are made for differing Cn .

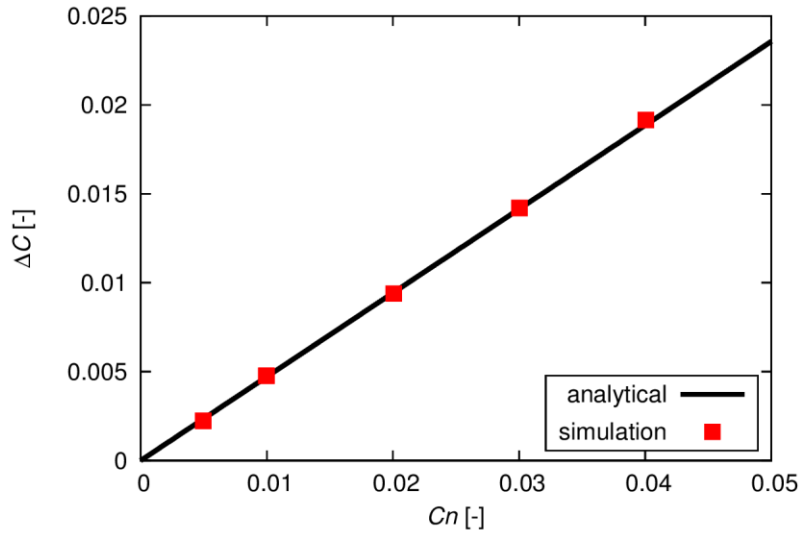


Figure 3.3: Comparison of the analytical estimate from Yue et al. [97] and present numerical results with respect to the Cahn number Cn versus the shift in order parameter ΔC . Adapted from Cai et al. [142].

Figure 3.3 shows an excellent match between the theoretical estimate and present computational results. As Cn decreases, the shift ΔC gets smaller and the upper/lower limits of the order parameter approach the physically “should-be”. Thus having Cn as small as possible favors mass conservation and helps prohibit spontaneous shrinkage that is bound to occur if too large shift ΔC arises. On the other hand, since Cn denotes

interface thickness, it is very computationally expensive to have a very small Cn where extremely fine mesh would be required. As a compromise between computational accuracy and expense, $Cn = 0.01$ is used in all the upcoming simulations reported in this present chapter.

3.2 Droplet Deformation in Unbounded Shear Flow

As discussed in Section 2.1.2, the interfacial tension is formed with chemical potential (CP) in the present PhD study. This is essentially distinct from other conventional interfacial tension formulations such as continuum surface force (CSF) [166] or continuous surface stress (CSS) [167]. Thus, it is necessary to verify the implementation of the CP-based interfacial tension (see Eq. (2.10)). For this purpose, a 2D interfacial flow problem is considered: by imposing wall velocity U and $-U$ to top and bottom boundary respectively, a shear flow forms in the computational domain (as shown in Figure 3.4). Due to this shear flow, an initially circular droplet (diameter D_0 and radius $R_0 = D_0 / 2$) at the center of the domain deforms to an elliptic one. The elliptic droplet at equilibrium features a balance between shear and interfacial forces, and its shape is quantified by the deformation parameter $D_{\text{def}} = (L_{\text{long}} - L_{\text{short}}) / (L_{\text{long}} + L_{\text{short}})$ where L_{long} and L_{short} are the respective length of the long and short axis of the ellipsoid; see Figure 3.4. For this flow problem, Taylor [168] derived an analytical solution for D_{def} :

$$D_{\text{def}} = \frac{35}{32} \cdot \frac{\mu_L \dot{\gamma} R_0}{\sigma} \quad (3.4)$$

where $\dot{\gamma}$ is the shear rate. It is noted that Eq. (3.4) was derived with the assumptions of (i) viscosity-matched binary fluids and (ii) creeping flows. In the present test case, the shear rate can be expressed as:

$$\dot{\gamma} = \frac{2U}{H} = \frac{U}{2R_0} \quad (3.5)$$

Substituting Eq. (3.5) into Eq. (3.4), one obtains:

$$D_{\text{def}} = \frac{35}{32} \cdot \frac{\mu_L (U / 2R_0) R_0}{\sigma} = \frac{35}{64} \cdot \frac{\mu_L U}{\sigma} \quad (3.6)$$

The definition for the capillary number in Eq. (2.23) is rewritten here:

$$Ca = \frac{2\sqrt{2}}{3} \frac{\mu_L U}{\sigma} \quad (3.7)$$

Combining Eqs. (3.6) and (3.7), one finally arrives at:

$$D_{\text{def}} = \frac{105}{128\sqrt{2}} Ca \quad (3.8)$$

Equation (3.8) serves as the analytical profile with which the computational results are compared.

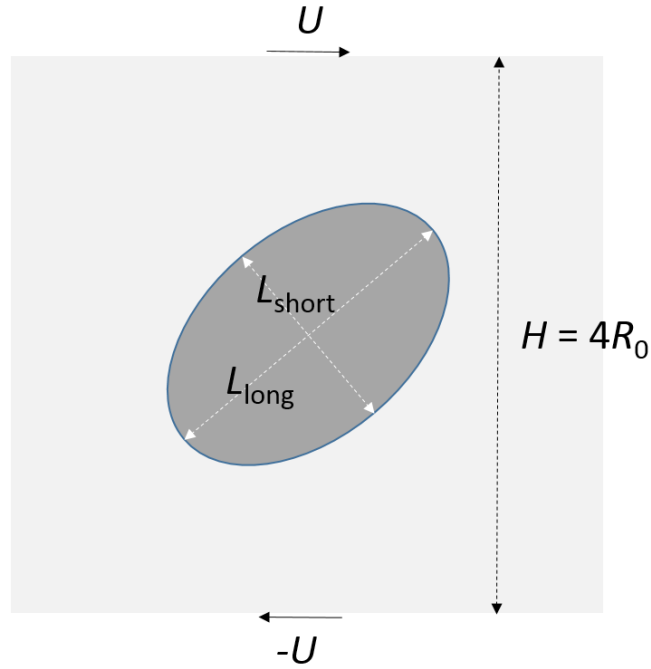


Figure 3.4: Due to the shear flow, an initially spherical droplet of radius R_0 deforms to an ellipsoid with long axis L_{long} and short axis L_{short} . Adapted from Cai et al. [142].

Before the primary simulation, a precursor computation is carried out. There by numerically solving CH equation without convective term, one obtains an equilibrium state of C with a hyperbolic tangent profile — as shown by Eq. (2.4) or its non-dimensional

counterpart Eq. (3.2) — across the interface. This equilibrium field of C is then used as initial condition for the upcoming primary simulation. A similar approach was already used by Badalassi et al. [169].

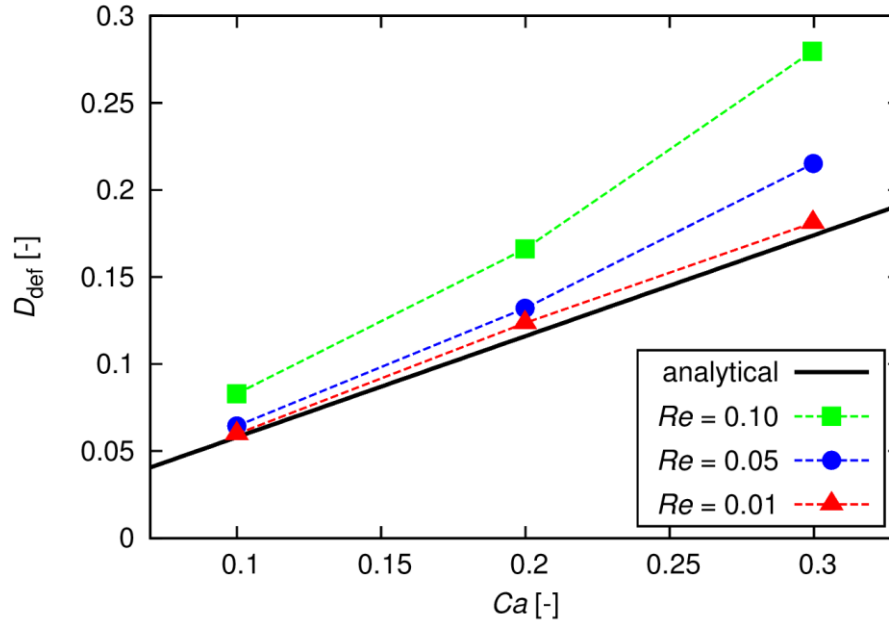


Figure 3.5: Comparison between the computational results for differing Reynolds number Re and Taylor’s analytical solution (Eq. (3.8)) with respect to the deformation parameter D_{def} versus the capillary number Ca . Adapted from Cai et al. [142].

The primary simulations are then performed. Therein wall velocity U and $-U$ are specified for the top and bottom boundary respectively (as shown in Figure 3.4) and free slip conditions are set for the left and right boundary. For the order parameter field, zero gradient conditions are applied at all boundary patches. The computational results in comparison with Taylor’s analytical solution (Eq. (3.8)) are shown in Figure 3.5. As Re (see Eq. (2.23) for the definition) is decreasing and approaching zero, the computational results are approximating the analytical profile. This trend is reasonable considering that

Taylor's analytical solution was derived with creeping (Stokes) flow assumption (where Re is limiting to zero).

3.3 Capillary Rise in Vertical Channel

The main objective of this PhD study is to describe wetting-related processes where a gas-liquid interface is in contact with a solid surface. Thus, it is necessary to verify the code for capillary-driven interfacial problems at a wall. For this purpose, a test-case on capillary rise of a liquid in a vertical narrow channel is performed. Based on the force balance between capillarity and gravity at final equilibrium state, the final height of the liquid column (H_{col}) and the channel width (d) obey the following analytical relation [170]:

$$\frac{H_{col}}{d} = \frac{2\sigma \cos(\theta_e)}{\rho_L g d^2} \quad (3.9)$$

In the present study, the liquid and gas are water ($\rho_L = 998 \text{ kg m}^{-3}$ and $\mu_L = 10^{-3} \text{ Pa s}$) and air ($\rho_G = 1.2 \text{ kg m}^{-3}$ and $\mu_G = 1.81 \times 10^{-5} \text{ Pa s}$) with interfacial tension $\sigma = 0.072 \text{ N m}^{-1}$. The channel width $d = 2 \text{ mm}$ and the gravitational acceleration $g = 9.81 \text{ m s}^{-2}$.

For phase field specific parameters, $Cn = 0.025$ and $Pe_c = 327$ are adopted. A homogenous Cartesian grid is generated for the computational geometry; there 40 mesh cells are used to resolve d and correspondingly 4 mesh cells for diffuse interface width L_C (i.e., where $-0.9 \leq C \leq 0.9$). In this test case the interfacial flow system evolves to a steady state and no characteristic velocity U could be directly identified from the physical system. Thus U is chosen indirectly by following $Re = 1$. At the channel walls, the boundary conditions are set as no-slip for the flow field and Neumann condition (expressed by Eq. (2.7), where the equilibrium contact angle θ_e is specified) for the order parameter field; at the top, they are configured as *pressureInletOutletVelocity* with zero relative pressure for the flow field and *zeroGradient* for the order parameter field. Figure 3.6 illustrates a series of snapshots visualizing a simulated capillary rise process of water within the channel with surface wettability $\theta_e = 45^\circ$.

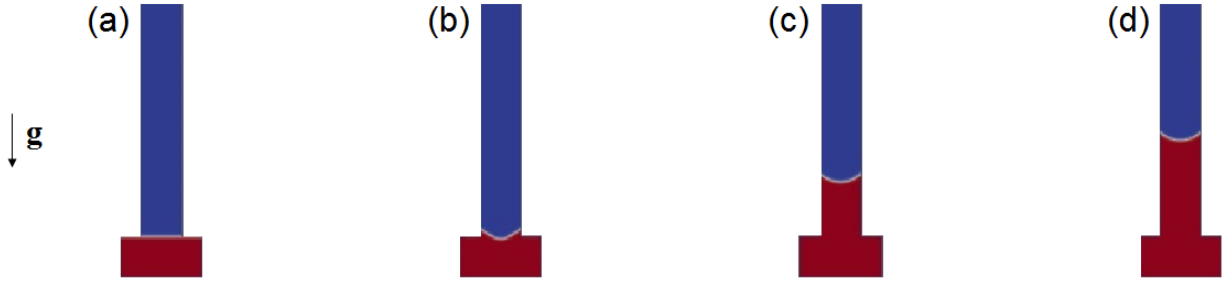


Figure 3.6: Simulated capillary rise of water into a vertical narrow channel at four instants: (a) 0 ms (initial state), (b) 3 ms, (c) 30 ms, (d) 100 ms (final state). The channel width $d = 2\text{mm}$ and the equilibrium contact angle $\theta_e = 45^\circ$. Adapted from Cai et al. [137].

At the beginning the vertical channel contains only the air while the water is in the horizontal container (Figure 3.6 a). Due to wall adhesion force, the water is slightly creeping up along the wall so that the prescribed equilibrium contact angle $\theta_e = 45^\circ$ is met (Figure 3.6 b). The curved interface gives rise to a pressure difference that pushes the water upward (Figure 3.6 c). The water column keeps rising until the gravity force reaches balance with the capillary force (Figure 3.6 d).

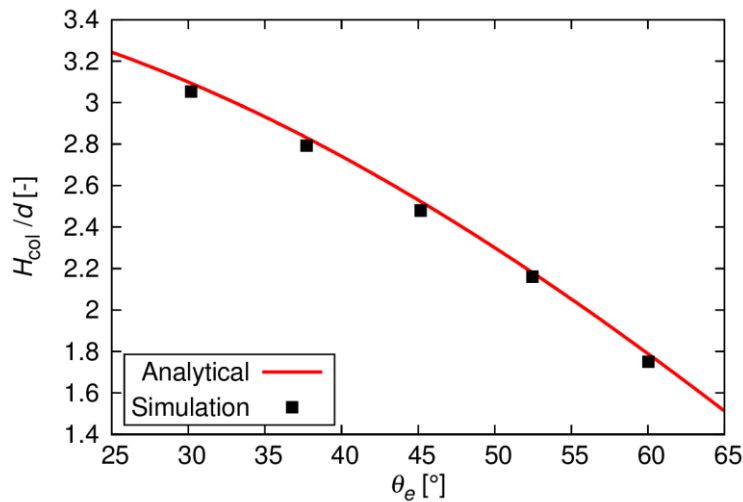


Figure 3.7: Computed and analytical water column equilibrium height for different equilibrium contact angles. Adapted from Cai et al. [137].

Further simulations are made for other four values of θ_e in the range $30^\circ \leq \theta_e \leq 60^\circ$. As illustrated in Figure 3.7, the predicted static water column height (assessed halfway between the channel centerline and the right wall) is in good match with the analytical solution in Eq. (3.9) for all the considered equilibrium contact angles.

3.4 Summary of Chapter 3

This chapter has presented code verification for several fundamental interfacial or capillary-driven phenomena, namely, phase-field diffusion, droplet deformation in shear flow and capillary rise in vertical channel. For all the above flow problems, the numerical results prove in good match with corresponding analytical solutions. With the gained experience and confidence in *phaseFieldFoam*, the code is to be employed to describe wetting-related processes; these will be presented in the succeeding chapters.

4 Droplet Wetting on Flat Solid Surfaces

This chapter presents numerical investigations into a series of droplet wetting phenomena on horizontal surfaces, being either homogenous or chemically heterogeneous. The numerical results shall be compared with analytical, experimental or reference computational data from literature. The results and figures presented in this chapter have been published in Cai et al. [137].

4.1 Equilibrium Shape

Equilibrium shapes of droplets resting on ideal surface are brought firstly under examination. Simulated steady-state dimensions of the droplets are compared with analytical solutions. A semi-circular droplet with initial radius $R_0 = D_0/2$ and contact angle $\theta_0 = 90^\circ$ (Figure 4.1 a) is taken as initial conditions for simulations. For the final steady state, a specific equilibrium contact angle θ_e corresponds to a certain equilibrium droplet shape with height H_e and base length L_e (Figure 4.1 b).

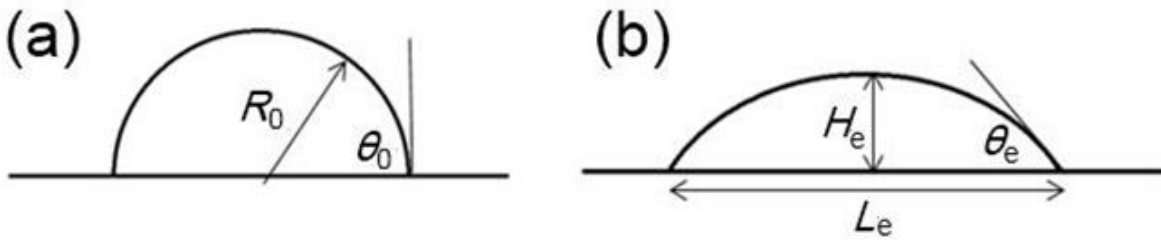


Figure 4.1: (a) Initial shape of a droplet deposited on surface. (b) Its equilibrium shape for a given equilibrium contact angle θ_e . Adapted from Cai et al. [137].

For the present 2D simulations, a computational domain of the dimensions $3D_0 \times D_0$ is set up, and uniform Cartesian grid is generated with mesh resolution for D_0 being 50 cells (i.e., that for diffuse interface thickness L_c being 4 cells). Here $Cn = 0.01$, $Pe_c = 1000$ and characteristic length scale L is chosen as D_0 . At the base solid surface, the boundary

conditions are set as no-slip for the flow field and Neumann condition (expressed by Eq. (2.7), where the equilibrium contact angle θ_e is specified) for the order parameter field; at the top and side boundary patches, they are configured as *pressureInletOutletVelocity* with zero relative pressure for the flow field and *zeroGradient* for the order parameter field.

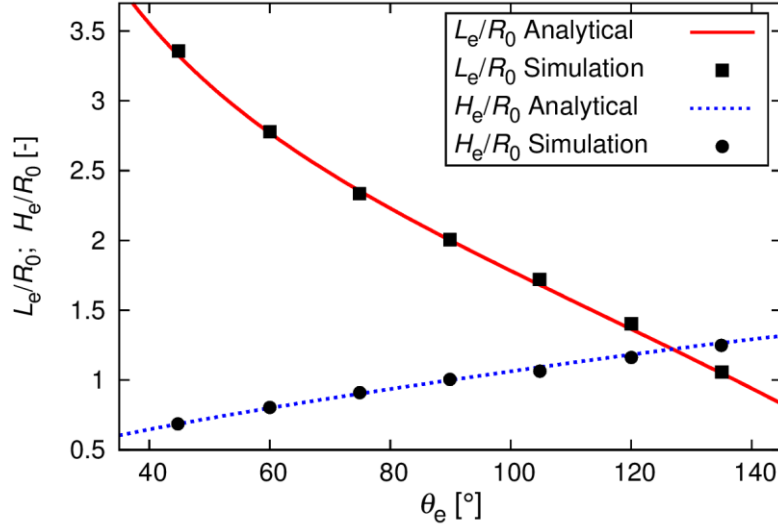


Figure 4.2: Comparison of the present simulation results and the analytical solutions [47] in terms of H_e/R_0 and L_e/R_0 versus θ_e . Adapted from Cai et al. [137].

Akin to numerical simulations using other interface-capturing approaches such as VOF [47] and Level-Set [116], the present numerical investigation firstly concerns the case when gravity is assumed to be negligible ($Eu = 0$), so that droplet equilibrium shape is governed by capillary force alone. Here the droplet is wetting/spreading for $\theta_e < \theta_0$ and is de-wetting/recoiling for $\theta_e > \theta_0$. For both processes, the steady-state droplet forms a circular cap. Following geometrical constraints one has [47]:

$$L_e = 2R_0 \sin \theta_e \sqrt{\frac{\pi}{2(\theta_e - \sin \theta_e \cos \theta_e)}} \quad (4.1)$$

$$H_e = R_0(1 - \cos \theta_e) \sqrt{\frac{\pi}{2(\theta_e - \sin \theta_e \cos \theta_e)}} \quad (4.2)$$

A line-up of simulations are carried out for seven distinct equilibrium contact angles in the range $45^\circ \leq \theta_e \leq 135^\circ$. Figure 4.2 demonstrates the comparison of the simulation results and the analytical solutions from Eqs. (4.1) and (4.2) in terms of H_e/R_0 and L_e/R_0 versus θ_e . A very good agreement is found for such a wide range of wettability covering hydrophilicity and hydrophobicity.

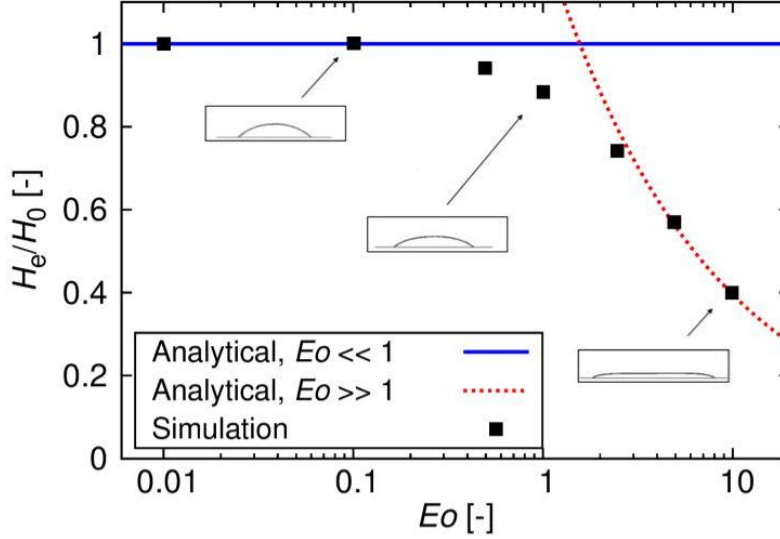


Figure 4.3: Comparison of the present simulation results and the analytical solutions [47, 171] in terms of normalized droplet height as function of the Eötvös number for $\theta_e = 60^\circ$. The insets show the final droplet shape for the respective Eötvös number. Adapted from Cai et al. [137].

If $Eo > 0$, then the equilibrium droplet shape is determined by a competition between gravity and capillarity: the former attempts to further spread out (flatten) the droplet while the latter tends to keep its form as a circular cap. Provided the Eötvös number is sufficiently large (i.e. $Eo \gg 1$), the gravitational force dominates over its capillary counterpart and then the droplet appears as a puddle. The height of such a droplet puddle is analytically expressed by [171]:

$$H_\infty = \frac{2R_0}{\sqrt{Eo}} \sin\left(\frac{\theta_e}{2}\right) \quad (4.3)$$

The present simulations are carried out for a fixed equilibrium contact angle $\theta_e = 60^\circ$ and a group of varying Eötvös numbers in the range $0.01 \leq Eo \leq 10$. Figure 4.3 depicts the normalized droplet height H_e/H_0 as a function of the Eötvös number Eo . If $Eo \leq 0.1$ (that is, capillary-dominated regime), the numerical results appear in good match with the asymptotic solutions given by Eq. (4.2). For $Eo \geq 5$ (gravity-dominated regime), the numerical data are found in agreement with the asymptotic solution given by Eq. (4.3). $Eo \approx 1$ implies a transitional regime between the above two. The insets in Figure 4.3 show respective droplet shapes in these three regimes: a circular cap for $Eo = 0.1$, an elongated circular cap for $Eo = 1$ and a puddle for $Eo = 10$.

4.2 Spreading Dynamics

This section puts into examination wetting dynamical process of a droplet spreading on a hydrophilic surface. In the following presentation of instantaneous numerical results, physical time is normalized by the capillary time-scale $t_{\text{cap}} = \mu_A L / \gamma = \mu_A D_0 / \gamma$.

4.2.1 2D Axisymmetric Simulations

To reproduce dynamic wetting behavior in reality, 2D axisymmetric simulations are carried out and the results are compared with the experimental data from Zosel [172]. In his experiment, spreading processes of droplets of varying viscosities were investigated and corresponding transient spreading factors were measured. The droplet diameters ranged from 2.4 to 3 mm. Considering such a size range, gravitational effects are assumed negligible in the present simulations. Through the tip of a syringe needle, the droplets of nearly spherical shape were slowly deposited onto surfaces, so that impact effect (initial kinetic energy) of the droplets was minimized in the experiment. Thus inertial forces are also neglected and density ratio between the two phases is specified to unity in the current numerical study.

For the experiment-simulation comparison, a specific experiment from Zosel [172] is selected. There, the droplet consisted of polyisobutylene ($\mu_L = 25 \text{ Pa s}$, $\rho_L = 920 \text{ kg m}^{-3}$ and $\sigma = 0.0426 \text{ N m}^{-1}$). Its initial diameter was $D_0 = 2.6 \text{ mm}$ and the base surface was polymer PTFE with the equilibrium contact angle $\theta_e = 58^\circ$. In the experiment, the viscosity ratio between the surrounding air and droplet was $\lambda_\mu = \mu_G / \mu_L \approx 10^{-6}$. Yet in the present numerical study, $\lambda_\mu = 0.05$ is used to alleviate computational burdens. This choice is justified by a preliminary sensitivity investigation which shows that the computational results get independent of λ_μ when $\lambda_\mu \leq 0.05$. In the 2D axisymmetric simulations, the computational domain is of the dimension $2D_0 \times 1.5D_0$. The mesh resolution for initial droplet diameter and diffuse interface thickness is $N_D = 100$ and $N_C = 6$. With the Cahn number being fixed as $Cn = 0.01$, numerical simulations are carried out for two Peclet numbers $Pe_C = 200$ and 1000 respectively. The boundary conditions are the same as those used in the test cases reported in Section 4.1.

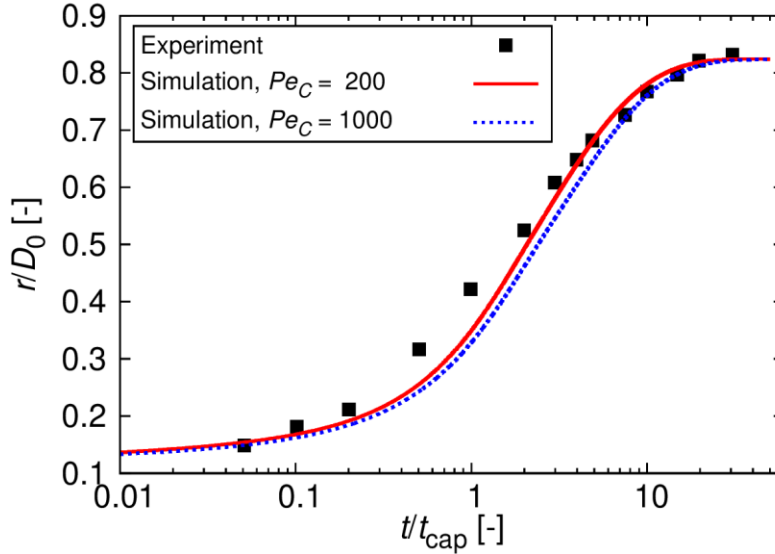


Figure 4.4: Comparison of the simulation ($Pe_C = 200$ and 1000) and the experiment [172] with respect to instantaneous droplet base radius. Taken from Cai et al. [137].

Figure 4.4 presents the comparison of the simulation results and experimental data [172] with respect to instantaneous base radius of the droplet. One finds a very good

agreement especially for the final spreading stage before the droplet reaches the equilibrium state. Another feature to note is that when Pe_c reduces, the base radius is enlarging at a slightly higher speed, implying a faster motion of contact line. This trend is reasonable considering that contact line motion is modeled in PFM as a diffusion process as discussed in Section 1.4.4; hence a stronger diffusion achieved through a smaller value of Pe_c — see Eq. (2.15) — gives rise to a faster spreading.

4.2.2 3D Simulations with Adaptive Mesh Refinement

Adaptive mesh refinement (AMR) is an important means to fulfil high computational efficiency especially for 3D PFM simulations that are typically computationally expensive. During an AMR simulation, sufficiently fine mesh is generated for interface neighborhood while relatively coarse grid may be applied for bulk regions. This is of special importance for PFM simulations where the interface is diffuse by its nature. As stated by Zhou et al. [98], the diffuse interface thickness should be small enough so that the sharp interface limit could be approached whilst sufficient mesh resolution for the thickness must be guaranteed to accurately capture interfacial phenomena.

Here the capability of the numerical method/code for 3D AMR is showcased. The AMR function is dealt with by the class *dynamicRefineFvMesh* in the standard OpenFOAM® library. The present demonstrating test-case is carried out with initially specified two-level mesh refinement for the interface neighborhood compared to the bulk regions (Figure 4.5). During the simulation the AMR is performed at each time step for the interfacial zone where $-0.9 < C < 0.9$. The boundary conditions in the present 3D AMR simulation are the same as those used in the test cases reported in Section 4.1.

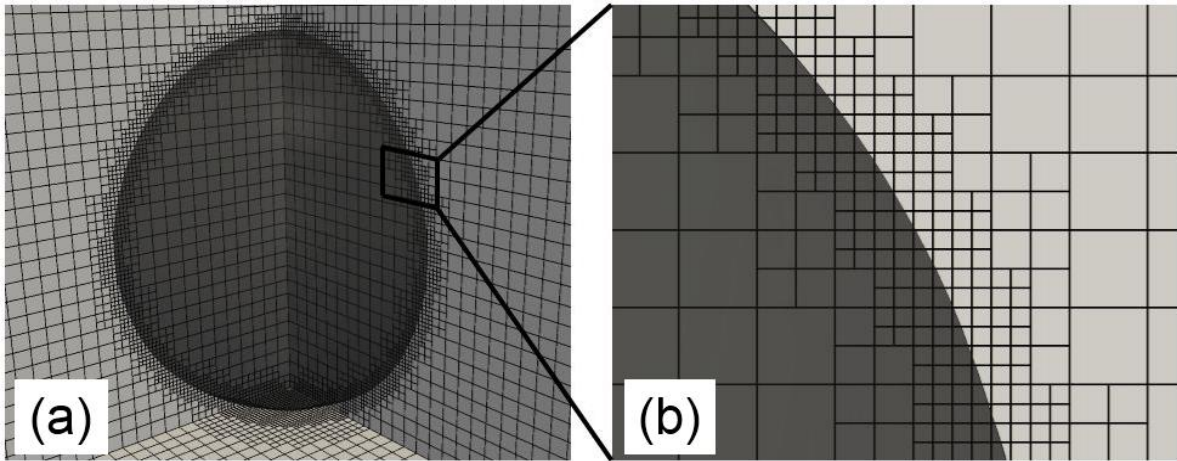


Figure 4.5: (a) Initial state of the 3D AMR simulation (one-quarter geometry and hexahedral grid) of a droplet wetting on a solid surface (equilibrium contact angle $\theta_e = 75^\circ$). (b) A close-up into the interfacial zone where two-level AMR is applied. Taken from Cai et al. [137].

Figure 4.6 shows the total wetting process delivered by the 3D AMR simulation. The process starts from the initial droplet shape where $\theta_0 = 170^\circ$ (Figure 4.6 a). As time proceeds, the droplet spreads out (Figure 4.6 b and c) and finally converges to the equilibrium state where $\theta_e = 75^\circ$ is achieved (Figure 4.6 d). In addition to the case $\theta_e = 75^\circ$, another 3D AMR simulation is carried out for $\theta_e = 90^\circ$.

In order to validate the accuracy of the 3D AMR simulations, reference 2D axisymmetric stationary-grid simulations are made with exactly the same mesh resolution for interface as well as physical and numerical parameters ($Ca = 0.94$, $\lambda_\mu = 0.1$, $Cn = 0.01$ and $Pe_c = 1000$). Figure 4.7 presents the comparison of the 3D AMR and 2D simulation results in terms of base radius versus time. Perfect agreements are observed for the both cases $\theta_e = 75^\circ$ and 90° . If comparing the curves from the two different equilibrium contact angles, one sees the influence of the surface wettability on the wetting process, which is already obvious from the very beginning: therein the droplet spreads at a higher rate on a more hydrophilic surface (smaller equilibrium contact angle). This trend is owing to the

fact that the difference between θ_0 and θ_e can be phenomenologically viewed as the driving force for a spreading process; therewith a larger mismatch gives rise to a faster spreading.

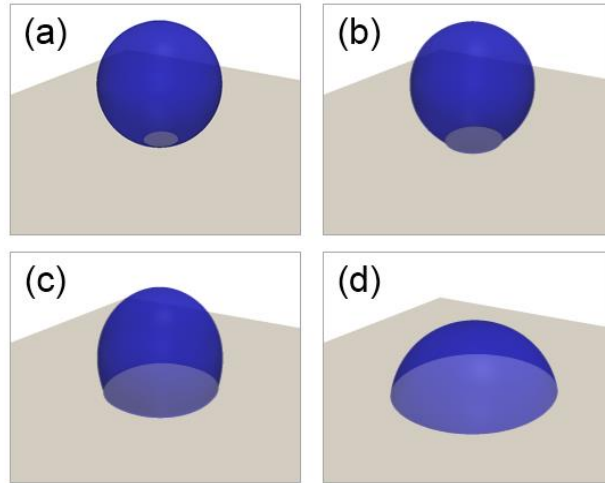


Figure 4.6: 3D AMR simulation of a droplet spreading process on a solid surface with $\theta_e = 75^\circ$ at different instants of (a) $t/t_{\text{cap}} = 0$ (initial state), (b) $t/t_{\text{cap}} = 2$, (c) $t/t_{\text{cap}} = 8$ and (d) $t/t_{\text{cap}} = 30$ (equilibrium shape). Taken from Cai et al. [137].

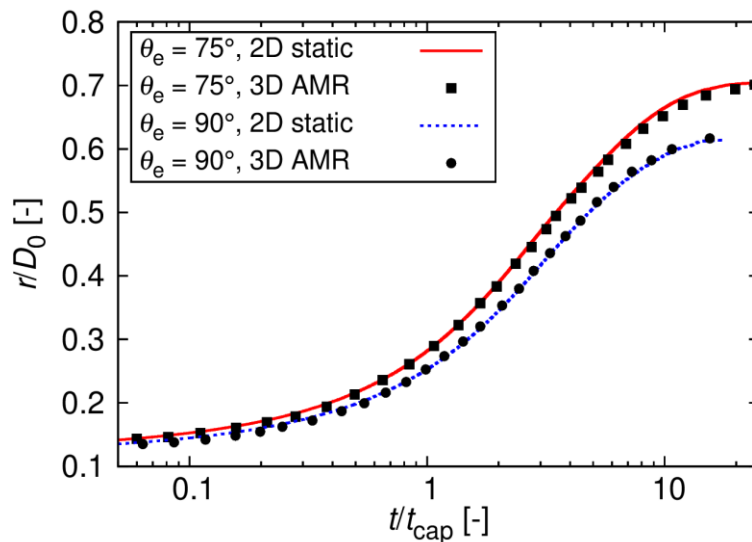


Figure 4.7: Comparison of 3D AMR and 2D axisymmetric stationary-grid simulations with respect to instantaneous droplet base radius. Taken from Cai et al. [137].

4.3 Droplet Spreading on Chemically-Heterogeneous Surfaces

The PhD thesis has so far investigated droplet wetting on a chemically homogeneous substrate where θ_e is unique. This section puts into consideration a chemically heterogeneous surface that is made up of alternating hydrophilic and hydrophobic stripes. The aim here is to demonstrate the predictive capability of the numerical method/code for directional droplet spreading and slick-slip motion of contact line that one expects for such an anisotropic wetting problem.

For the above-mentioned purpose, the present study considers a test-case similar to Jansen et al. [173] who investigated droplet directional wetting on chemically-patterned surfaces through their experiment and lattice Boltzmann method (LBM)-based simulation. There the base substrate consists of alternating hydrophobic perfluorodecyltrichlorosilane (PFDTs) ($\theta_e = 110^\circ$) and hydrophilic SiO₂ ($\theta_e = 40^\circ$) stripes, with their width ratio being 0.5. The present PF numerical results are to be compared with the experimental and LBM numerical counterparts from Jansen et al. [173]. It is noted that in the experiment the droplet at equilibrium spanned around 77 stripes beneath it; each stripe was very narrow. Sufficient mesh resolution of each stripe is thus rather prohibitive for any practical 3D simulations. Thus the LBM simulations by Jansen et al. [173] were carried out for wider stripes and accordingly a smaller number of stripes below the droplet than the experiment. The present PFM simulation adopts the same manner to alleviate computational burdens.

Jansen et al. [173] mention no physical properties but only dimensionless droplet/gas density for their LBM simulations; there the fluid pair were set to be of roughly identical kinematic viscosity. These parameters do not suffice for a quantitative recalculation with the present PFM numerical model. Therefore the polyisobutylene droplet studied in Zosel's experiment (see Section 4.2.1) is under consideration in the current simulations. Owing to the different physical properties, the LBM and PF simulation results are compared here in a qualitative manner.

In the present numerical investigation $Ca = 0.94$, $Pe_C = 1000$, $Cn = 0.02$ and $\lambda_\mu = 0.1$ are adopted. The corresponding mesh resolution for the diffuse interface and droplet diameter is $N_C = 4$ and $N_D = 50$; four and two mesh cells are used to resolve each SiO₂ stripe and PFDTs stripe respectively. Two equilibrium contact angles $\theta_e = 110^\circ$ and $\theta_e = 40^\circ$ are specified to the solid substrate following the stripe pattern. Except for this, the boundary conditions are the same as those used in the test cases reported in Section 4.1.

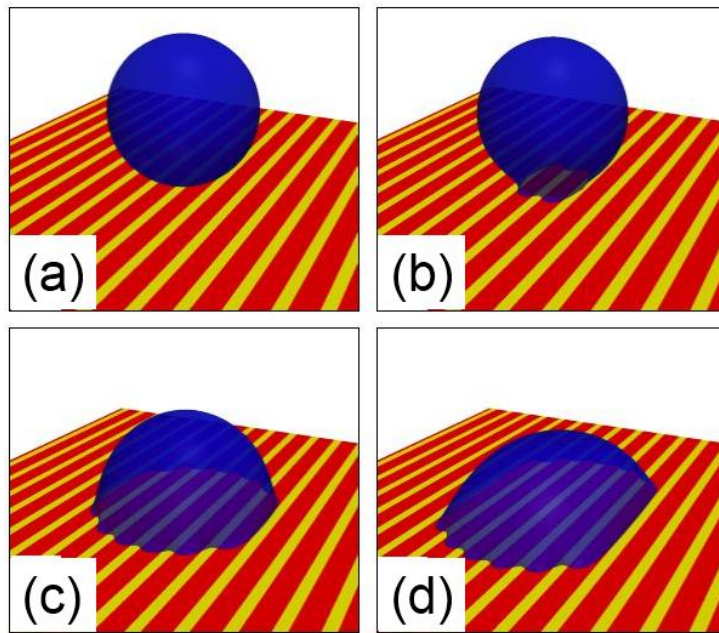


Figure 4.8: PFM simulation of a droplet spreading process on the chemically-patterned surface (red stripes: SiO₂, $\theta_e = 40^\circ$ and yellow stripes: PFDTs, $\theta_e = 110^\circ$) at different instants of (a) $t/t_{\text{cap}} = 0$ (initial state), (b) $t/t_{\text{cap}} = 40$, (c) $t/t_{\text{cap}} = 200$ and (d) $t/t_{\text{cap}} = 1000$ (equilibrium state). Taken from Cai et al. [137].

The simulated wetting process on the chemically-patterned surface is shown in Figure 4.8. At the beginning the three-microliter glycerol droplet is deposited on the surface (Figure 4.8 a). As time proceeds, the droplet spreads out over the substrate (Figure 4.8 b) and its wetting behavior is different from that observed on a homogenous

surface: owing to the base stripe pattern, its spreading along the stripes is favored while that perpendicular to the stripes is hindered (Figure 4.8 c). As a result, the droplet at equilibrium forms a shape elongated along the stripe direction (Figure 4.8 d).

Figure 4.9 shows instantaneous moving distance of the contact line in both the directions. At equilibrium state, the value for the parallel direction to the stripes is larger than that in the perpendicular direction; this is also implied by Figure 4.8 d. Besides if looking at the temporal evolution, the contact line is found to travel fairly smoothly in the parallel direction while rather stick-slip-like in the perpendicular direction. This phenomenon can be attributed to a line-up of discrete energy barriers that the contact line has to overcome when it moves through hydrophobic stripes. Therewith, pinning (i.e. stick-slip-like) behavior and resulting limited spreading are found in this direction. By comparison, the contact line in the parallel direction does not experience such energy barriers and thus advances smoothly and reaches a longer distance.

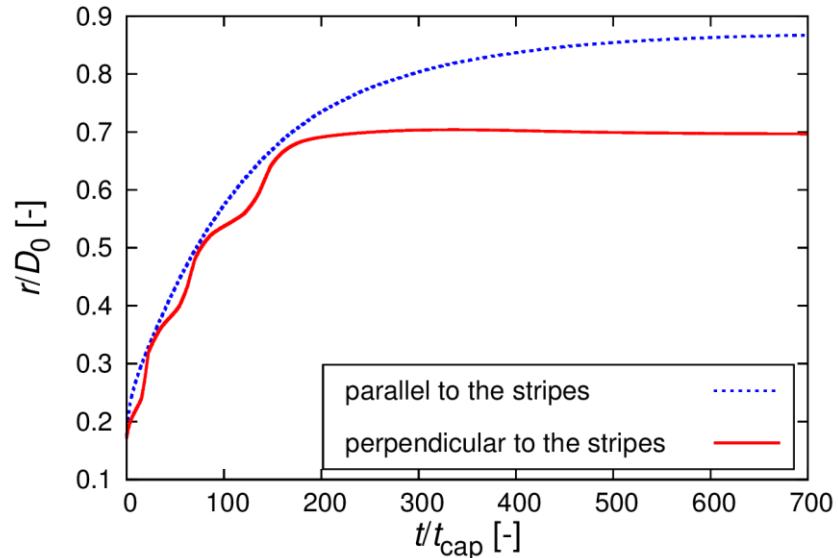


Figure 4.9: Instantaneous base radius of the droplet in the parallel and perpendicular direction to the stripes. Taken from Cai et al. [137].

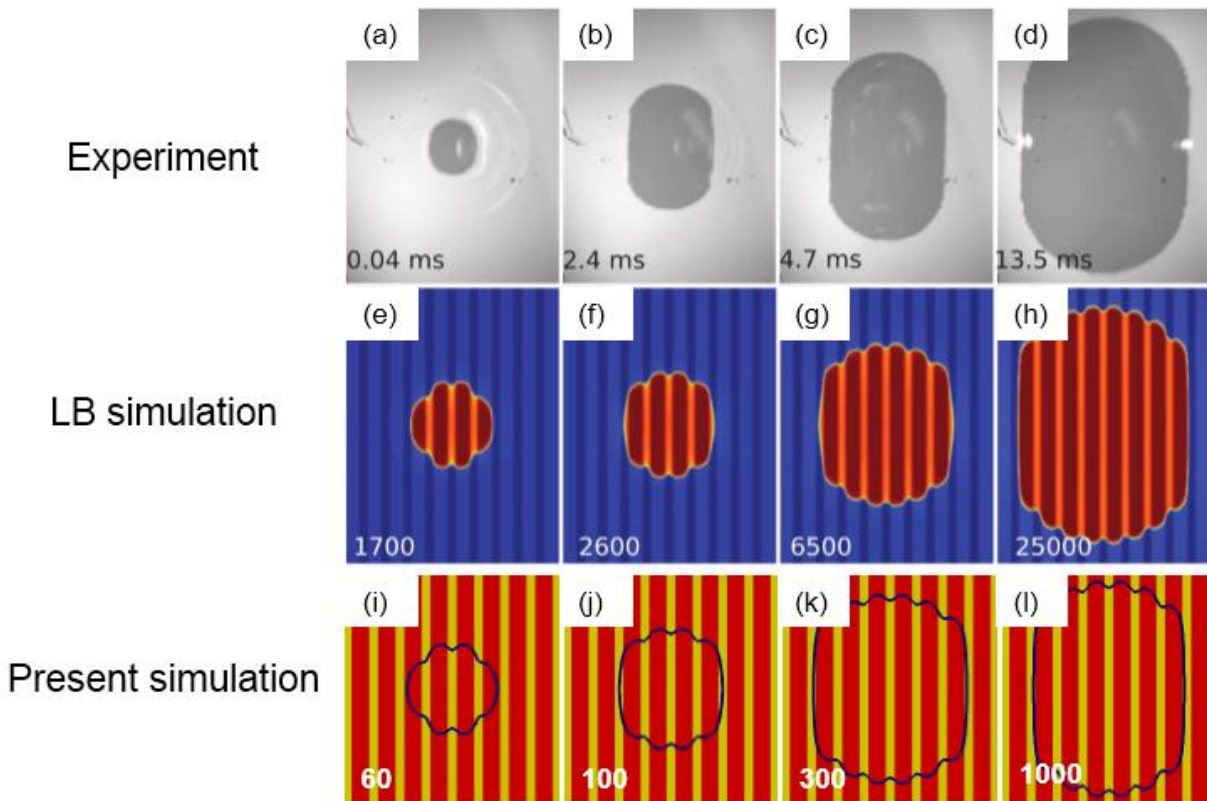


Figure 4.10: Temporal evolution of the droplet from a bottom-view. (a) – (h): the experiment and LB simulation from Jansen et al. [173]; (i) – (l): the present PF simulation. The numbers at the bottom left corner in subfigures (e) – (h) denote time step while those in subfigures (i) – (l) refer to t/t_{cap} . Taken from Cai et al. [137].

Figure 4.10 compares the experimental and LBM [173] as well as the present PF numerical results with respect to temporal evolution of the droplet shape from the bottom-view. At the earlier spreading stage the droplet appears a slightly elongated owing to the base surface pattern (Figure 4.10 a, e and i). As time proceeds, the drop spreads out along the stripe direction while its wetting in the perpendicular direction is confined. Therewith the shape elongation goes further until the equilibrium state (Figure 4.10 d, h and l). For the whole spreading process, the PF simulations deliver results in qualitative agreement with those by LBM.

In terms of the droplet profile, difference is found between the experiment and simulations: the contact line is smooth in the former while corrugated in the latter. The distinction is attributed to the different number of stripes beneath the droplet as discussed before. Such wave-like profiles were also reported by other numerical investigations [174] which also considered a relatively small number of stripes below the droplet.

4.4 Summary of Chapter 4

This chapter has presented PF-simulations for different droplet spreading processes on chemically homogenous/heterogeneous substrates. Steady-state or transient numerical results are in good agreement with the analytical solution, experimental or reference computational data. The use of local adaptive mesh refinement near interface is also demonstrated.

5 Interaction of a Rising Bubble with Solid Structures

This chapter presents numerical studies on an air bubble (immersed in liquid phase) rising and interacting with solid structures. The numerical method/code is first validated for terminal bubble rise velocity and solid cylinder-induced breakup process of bubble. Then numerical investigations are performed towards bubble rising and deforming behavior inside a representative domain of a periodic open cellular structure (POCS). The results and figures presented in this chapter have been published in Cai et al. [138].

5.1 Introduction

In the German Helmholtz Energy Alliance “Energy Efficient Chemical Multiphase Processes” [143], it is a core scientific topic to explore the use of POCS as internal structured packing. POCS of different types are produced via additive manufacturing at Institute of Chemical Reaction Engineering, Friedrich-Alexander-University Erlangen-Nürnberg (FAU), Germany [8, 9]. Experimental studies on interfacial mass transfer around bubbles in POCS for bubble column reactor are carried out at Institute of Multiphase Flows, Hamburg University of Technology (TUHH), Germany [175]. Numerical investigations on hydrodynamics behavior of bubbles in POCS are carried out in the present PhD study at KIT.

The benefit of using POCS as internal packing for bubble column reactor mainly lies in its favorability for interfacial mass transfer enhancement and for catalytic reactions (if catalysts are deposited onto POCS surface). The present study is focused on a fundamental process, that is, hydrodynamics interaction between a single bubble and POCS; the interaction process will be shown to strongly depend on the structure surface wettability. In manufacturing processes, surface properties of POCS can be modified and thus different surface wettability (i.e. different equilibrium contact angle) can be fulfilled. Along with the POCS geometry, therefore, tuning surface wettability affects significantly

hydrodynamic interaction between bubble and structure and thereby serves as a very promising means to further promote interfacial mass transfer.

5.2 Terminal Bubble Rise Velocity

In this section, the numerical method/code is validated – with respect to terminal bubble rise velocity and cylinder-induced bubble breakup process – against corresponding experimental data from Segers [176]. The validation is carried out in two steps. Firstly through 2D axisymmetric simulations, the respective effect of grid resolution, Cahn number Cn and Peclet number Pe_c on predicted bubble rise velocity is shown. Numerical results from a suitable combination of these parameters are then compared with the experimental data. Secondly cylinder-triggered bubble breakup (i.e. cutting) process is reproduced in 3D simulations and their results are compared with the experimental and numerical data from Segers [176].

5.2.1 Physical Properties and Computational Set-up

In the experiments of Segers [176], glycerin-water mixtures of differing compositions were used; the Morton number $Mo = (\rho_L - \rho_G)g\mu_L^4 / \sigma^2\rho_L^3$ was varied through the liquid viscosity μ_L . The present study considers a specific case where $Mo = 0.064$. For this experimental case, density/viscosity of liquid/gas are $\rho_L = 1237.42 \text{ kg m}^{-3}$, $\rho_G = 1.0 \text{ kg m}^{-3}$, $\mu_L = 0.219 \text{ Pa s}$ and $\mu_G = 2 \times 10^{-5} \text{ Pa s}$; the interfacial tension is $\sigma = 0.0658 \text{ N m}^{-1}$. Thus the liquid-to-gas viscosity ratio is about $\lambda_\mu = \mu_L / \mu_G \approx 10^4$. To save computational cost, $\mu_G = 2.74 \times 10^{-4} \text{ Pa s}$ is set in the present numerical simulations so that $\lambda_\mu = 800$. It has been examined that the computational results get independent of λ_μ when $\lambda_\mu > 800$.

As initial conditions for the present simulations, a spherical bubble (diameter D and radius $R = D/2$) is released in the lower part of the 2D axisymmetric computational domain (Figure 5.1 a); therein both phases are quiescent. The height H and width W of the computational domain are $8R$ and $6R$. A sensitivity study on W showed that a further

increase from $6R$ has no influence on the numerical results. An isotropic Cartesian grid of uniform mesh size h is generated within the domain. $N_D = D/h$ mesh cells are used to resolve the initial bubble diameter D . As introduced in Section 2.1.1, the interfacial width L_C is defined as the distance over which the variation $-0.9 \leq C \leq 0.9$ takes place, therefore $L_C \approx 4.164\varepsilon$. For the formulation of Cahn number Cn in the present test case, the reference length scale L is chosen as the bubble initial diameter. Hence, the mesh resolution for L_C is $N_C \approx 4\varepsilon/h = 4CnN_D$.

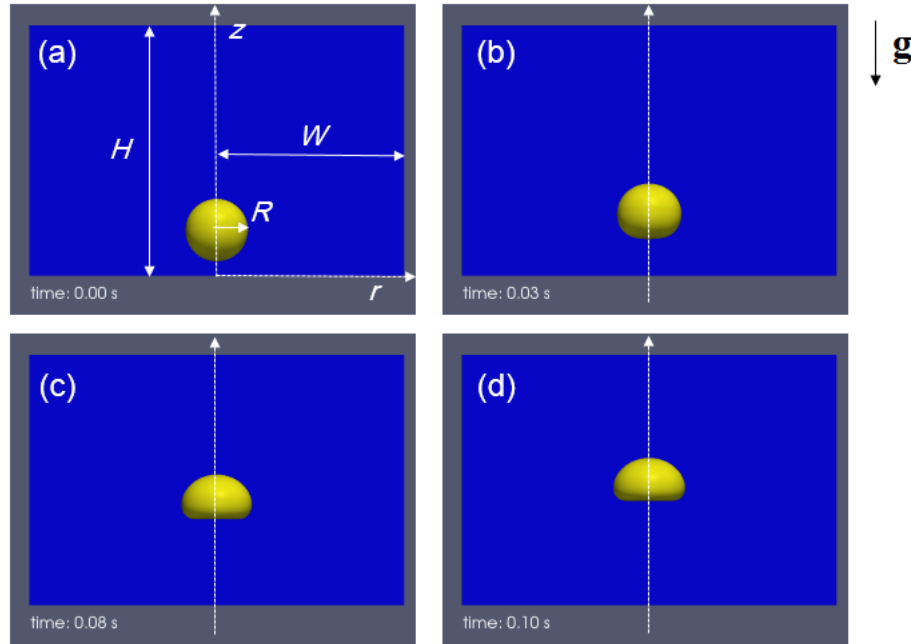


Figure 5.1: 2D axisymmetric phase-field simulation of an air bubble rising in quiescent liquid with $Cn = 0.02$, $Pe_c = 1008$, $N_C = 6$ and $N_D = 75$. Taken from Cai et al. [138].

The boundary conditions for fluid flow are configured as *pressureInletOutletVelocity* with zero relative pressure at the top and bottom of the computational domain and free slip at side boundary patch. Zero gradient boundary conditions are used for order

parameter since no interaction between bubble and solid surface is considered in the current validation stage.

As a baseline numerical test case, one specific experiment (the initial bubble diameter D of 10.3 mm and Eötvös number $Eu = (\rho_L - \rho_G)gD^2 / \sigma$ of 19.6) from Segers [176] is put under consideration. The terminal bubble velocity U_B is measured as 0.172ms^{-1} ; the terminal Reynolds number $Re = \rho_L D U_B / \mu_L$ is 9.85. The simulated bubble rising process at four temporal instants is demonstrated in Figure 5.1. Within a rising distance of roughly one initial diameter, the bubble forms a steady shape and reaches a constant (i.e., terminal) rise velocity; see Figure 5.1 d. In this dynamic equilibrium state, the buoyance force is in balance with the drag force applied to the bubble surface by the ambient liquid. For the present combination of Eu , Mo and Re , the simulated steady bubble shape is in good match with the established shape regime map in Clift et al. [177].

5.2.2 Numerical Parameter Study

This section investigates the respective influence of three numerical parameters on the predicted bubble rising velocity. Through this parameter study, an appropriate combination of these parameters is ascertained for the subsequent comparison of the numerical results and experimental data.

First, the effect of mesh resolution is put under examination. The baseline test case (presented in Section 5.2.1) is run for other three grid resolutions. Figure 5.2 presents simulated temporal evolution of bubble rising velocity under the influence of mesh. The number of cells to resolve interface width L_C is $N_C = 2, 4, 6$ and 8 respectively; considering $Cn = 0.02$, corresponding number of cells per bubble diameter D is $N_D = 25, 50, 75$ and 100 . As shown in Figure 5.2, the computational results get mesh-independent as $N_C \geq 6$ (i.e., $N_D \geq 75$).

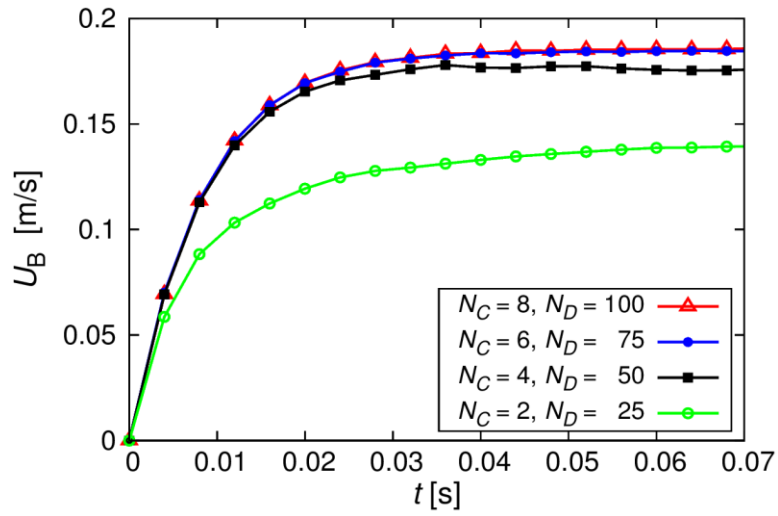


Figure 5.2: Simulated bubble rise velocity ($Cn=0.02$ and $Pe_c=1008$) with different mesh resolutions. Adapted from Cai et al. [138].

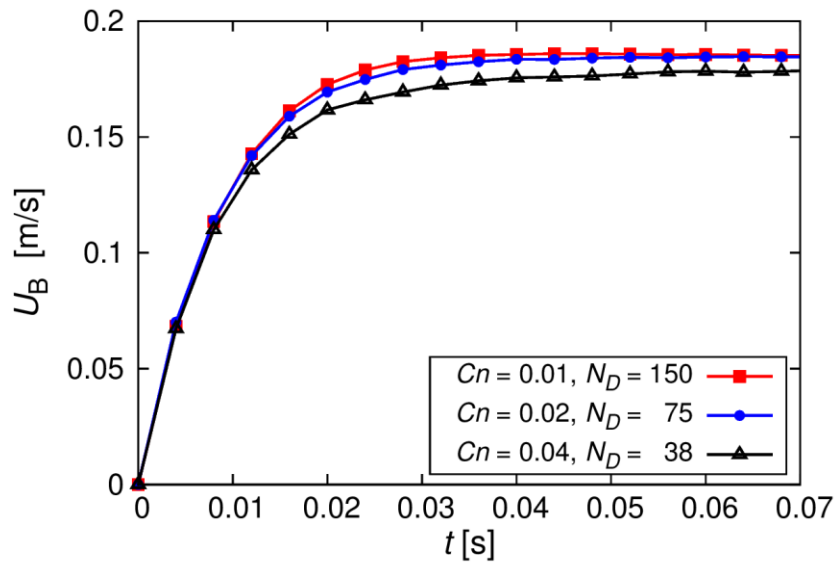


Figure 5.3: Simulated bubble rise velocity ($Pe_c=1008$ and $N_c=6$) with different Cahn numbers. Adapted from Cai et al. [138].

With $N_c = 6$ being fixed for interface mesh resolution, the Cahn number Cn is varied to examine its effect. Figure 5.3 shows simulated instantaneous bubble rise velocity for $Cn = 0.01$, $Cn = 0.02$ and $Cn = 0.04$. These values correspond to $N_c = 150$, 75 and 38 , respectively. As Cn is going smaller, the numerical results are converging. The predicted terminal velocity is insensitive to Cn provided $Cn \leq 0.02$. Since the terminal velocity is of focus in the present study, all the following 2D simulations are performed with $Cn = 0.02$ to save computational cost.

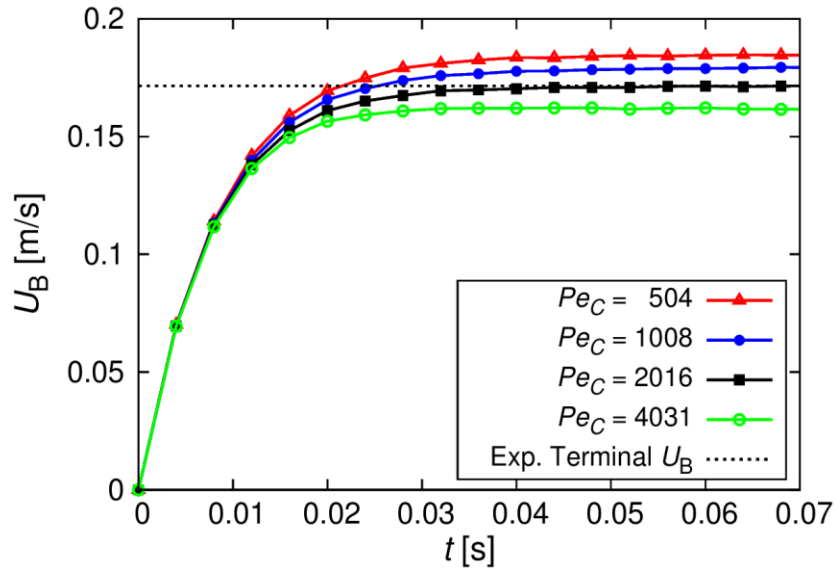


Figure 5.4: Simulated bubble rise velocity ($Cn = 0.02$, $N_c = 6$ and $N_d = 75$) with different Peclet numbers. The dashed horizontal line indicates the terminal bubble velocity measured by the experiment. Adapted from Cai et al. [138].

Lastly, the influence of the Peclet number Pe_c is studied. In PF methods, Pe_c serves as quantifier for a diffusion process (see RHS of Eq. (2.15)). As discussed in Section 2.1.4, the characteristic length scale (molecular scale) of the diffusion process is by several orders-of-magnitude smaller than bubble diameter (millimeter scale). Resolving the

diffusion process requires a prohibitive computational cost and thus this is not attempted in this study. Instead, the diffusion process is coarse-grained into the continuum model and accordingly its quantifier Pe_c is treated as a phenomenological parameter. Following Ding et al. [102], the relation $Pe_c = Cn^{-2}$ is used to roughly estimate its value. Within one order-of-magnitude around this first estimate, Pe_c is varied. Figure 5.4 juxtaposes the computational results for differing Pe_c , which shows a notable influence on the simulated bubble (terminal) rise velocity. As a phenomenological parameter, Pe_c may be regarded as an intrinsic material property characterizing a given flow system [94]. Thus for the present physical system, $Pe_c = 2016$ is selected for the upcoming simulations because it gives the best match with the experimental terminal velocity of 0.172 ms^{-1} ; see Figure 5.4.

5.2.3 Validation

Section 5.2.2 has identified a suitable numerical parameter combination of $N_c = 6$, $Cn = 0.02$ and $Pe_c = 2016$. Using these parameters, the simulated bubble terminal velocity is in good match with the measured value for the specific experiment where the bubble diameter is $D = 10.3 \text{ mm}$ and meanwhile high computational efficiency is guaranteed. With these numerical parameters unchanged, further simulations are made for other four different bubble diameters $D = 7.4 \text{ mm}$, 12.4 mm , 14.2 mm and 15.7 mm respectively, as performed in the experiment of Segers [176]. These respective values of bubble diameters correspond to the Eötvös number $EO = 10.2$, 28.3 , 37.3 , and 45.6 .

Figure 5.5 presents the comparison of the experimental data and current numerical results in terms of the relation between the Eötvös number EO and terminal Reynolds number Re . There a perfect agreement is found for $EO = 19.5$, because the Peclet number $Pe_c = 2016$ is chosen by reference to the experimental data for this Eötvös number/bubble diameter (see Figure 5.4). However, the numerical simulation slightly under-predicts the experimental terminal Reynolds number for $EO = 10.2$ whilst the former slightly over-

estimates the latter for the cases where $Eo > 20$. These results imply that the optimal value of Pe_c (i.e., one which produces the best agreement between the computational and experimental data) is weakly depending on the Eötvös number Eo . It is expected from Figure 5.4 that the most suitable value of Pe_c should be slightly elevated as Eo gets larger. Yet no efforts are made in this study to quantitatively investigate the relationship. As a whole, the match between the experimental and simulated bubble terminal velocity is reasonably good for a wide spectrum of Eo .

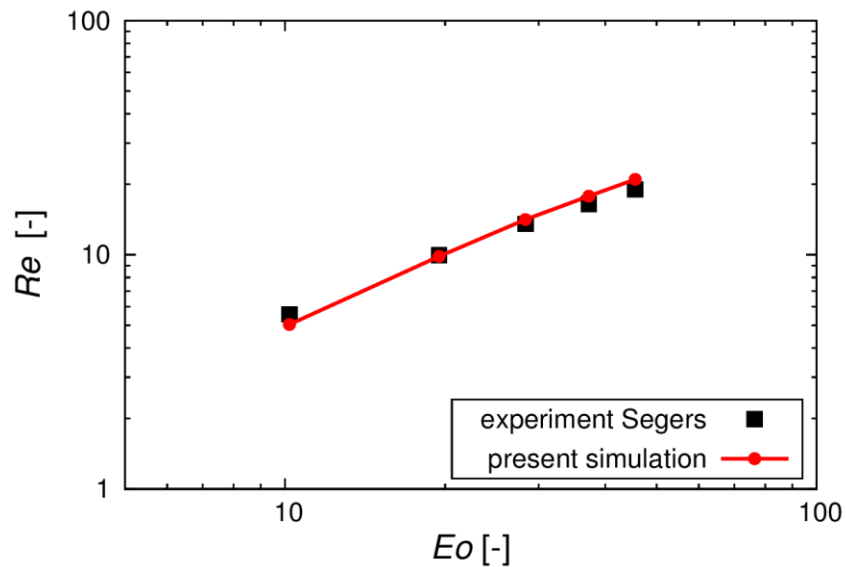


Figure 5.5: Comparison of the present numerical results with the experimental data from Segers [176], with respect to the terminal bubble Reynolds number versus the Eötvös number. Adapted from Cai et al. [138].

5.3 Cylinder-induced Bubble Cutting

Having examined the predictive capability of the numerical model for bubble terminal velocity in Section 5.2, the study proceeds with the validation for breakup/cutting behavior of a bubble interacting with a solid cylinder. Considering the nature of this physical process, 3D simulations are required here.

5.3.1 Computational Set-up

In an attempt to reduce computational cost, one quarter of the problem domain with two symmetry-planes is under consideration in the present 3D simulations. The utilization of symmetry is justified given that the bubble rises rectilinearly under the physical conditions considered in the current study. A rectangular domain of a square cross-section $4R \times 4R$ and height $12R$ is used. A horizontal solid cylinder with diameter D_{cyl} is put in the upper part of the domain. As initial numerical conditions, a spherical bubble of diameter D is positioned sufficiently far away below the cylinder to make sure that the bubble has formed its equilibrium shape and reached the terminal rise velocity before it approaches the cylinder. In accordance with the experiment of Segers [176], $D_{\text{cyl}} = 3.1\text{mm}$ and $D = 9.14\text{mm}$ are adopted in the current numerical study.

Boundary conditions are set up as follows. On the surface of the solid cylinder, no-slip is imposed to velocity while wetting condition with a specified equilibrium contact angle (see Eq. (2.7)) is applied for order parameter. The top, bottom and side boundary patches are configured the same as the test case in Section 5.2.1. The physical and interfacial properties of both the phases are also identical to those in the test case reported by Section 5.2.1.

5.3.2 Mesh Resolution Study

Phase-field specific parameters Cn and N_C play an important role here. They determine on the degree of details one could numerically access to thin liquid film between the bubble and solid surface when the former approaches the latter. On one hand, using a smaller Cn , local interfacial physics and topology can be more accurately reproduced. On the other hand, reducing Cn normally amounts to higher computational cost, since the total number of mesh cells in a 3D simulation is on the magnitude of $(N_C / Cn)^3$ with $N_C = 4$ being as minimum mesh resolution for diffuse interface width L_C . The present

investigation concentrates on the validation of the numerical model for its predictive capability of the global bubble deformation and break-up process. Therefore $Cn = 0.04$ is adopted to save computational cost. As the simulations in Section 5.2 suggest, the computed bubble shape is rather insensitive to this choice. The variation in the value of Pe_c (shown in Figure 5.4) significantly affects predicted bubble rise velocity but does not have notable influences on predicted bubble shape. Thus $Pe_c = 1000$ is used in the following 3D simulations.

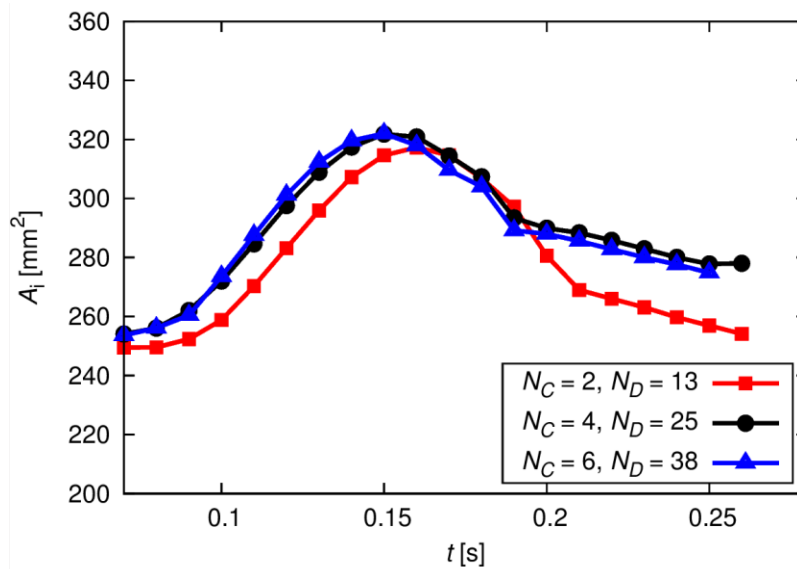


Figure 5.6: Instantaneous gas-liquid interfacial area during the bubble splitting process, delivered by the phase-field simulations ($\theta_e = 30^\circ$, $Cn = 0.04$ and $Pe_c = 1000$) with different mesh resolutions. Adapted from Cai et al. [138].

With the above-chosen values of Cn and Pe_c , grid dependence is studied through simulations of varying mesh resolution $N_C = 2, 4$ and 6 . Figure 5.6 illustrates the mesh influence on temporal evolution of gas-liquid interfacial area (i.e. bubble surface area) A_i during the whole process of the bubble interacting with the solid cylinder. Here A_i is

calculated as the area of the iso-surface $C = 0$. As shown in Figure 5.6, when the bubble is approaching the cylinder, the interface is enlarging in area – owing to cylinder-induced bubble concave deformation – until the moment $t \approx 0.15\text{s}$. At that time, the bubble is eventually split into two bubbles and then the total interfacial area is declining over time. From Figure 5.6, $N_c = 4$ appears as a good compromise between computational accuracy and effort. Hence, this mesh resolution is adopted in the following 3D simulations.

5.3.3 Validation

To represent surface wettability, the numerical model needs the equilibrium contact angle θ_e as an input; see Eq. (2.7). However neither θ_e nor cylinder material was given in Segers [176]. Through personal communication [178], the author got to know that the cylinder was made of stainless steel. From the experimental measurement of Wang et al. [179], the contact angle θ_e for different liquids on stainless steel ranges from 32° to 54° . In the following, $\theta_e = 60^\circ$ is used in the first test case and then numerical results using other values of θ_e are presented to reveal the influence of θ_e .

In Figure 5.7, the present phase-field (PF) simulation results are compared with the experimental measurement and the simulation based on a hybrid immersed-boundary volume-of-fluid (IBM-VOF) method [176]. For the comparison, the initial instant in time $t = 0$ is chosen so that – in the experiment and both the numerical simulations – the vertical distance of the bubble away from the cylinder is roughly the same and an equilibrium bubble shape has been reached (Figure 5.7 a, f and k). As the bubble is approaching the solid cylinder, it becomes flattened (Figure 5.7 b, g and l). When the bubble gets closer, its deformation is amplified and therein a thin liquid film forms below the cylinder (Figure 5.7 c, h and m). Shortly before the breakup, two daughter bubbles are emerging which are still bridged by a thin gas filament (Figure 5.7 d, i and n). After the

breakup process, both the daughter bubbles keep rising away from the cylinder (Figure 5.7 e, j and o).

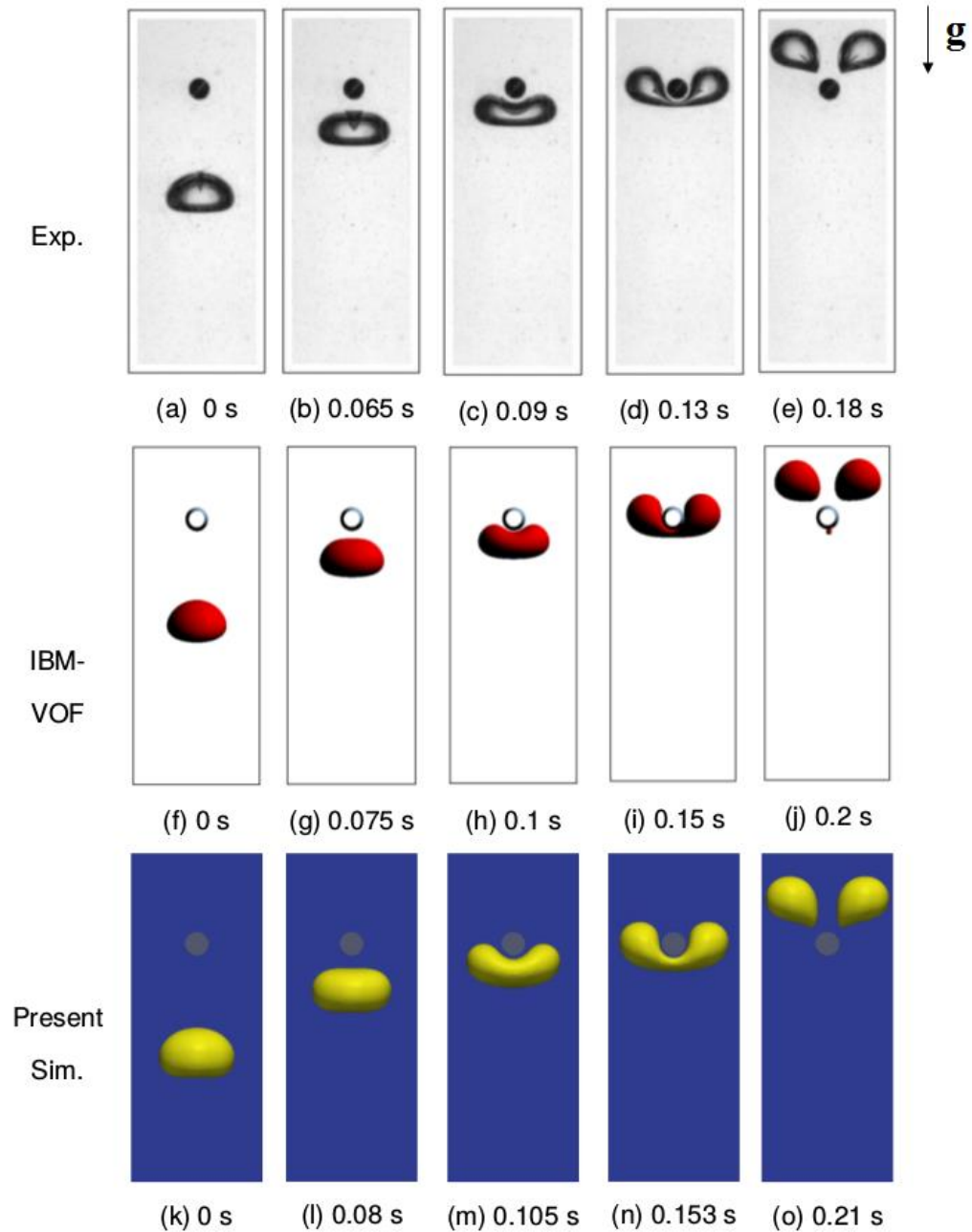


Figure 5.7: Cylinder-induced bubble cutting process. (a) – (j): experimental and numerical results from Segers [176]. In the adapted presentation here, 0.15 s is deducted from the original time frame used by Segers [176], so that a shorter computational domain needs to be considered by the present phase-field simulation ($\theta_c = 60^\circ$) shown in (k) – (o). Adapted from Cai et al. [138].

The present PF simulation is found in very good qualitative agreement with the experiment and IBM-VOF computational study from Segers [176]. However, the whole process of bubble deforming and splitting predicted by the present simulation is slightly longer than that by Segers [176]. The reason lies in the under-prediction of the bubble terminal velocity by the 3D PF simulation with $Cn = 0.04$ and $N_c = 4$, as suggested by Figure 5.2 and Figure 5.3. Besides, the gas filament below the cylinder in the PF simulation (Figure 5.7 n) appears noticeably thicker than that from the experiment and IBM-VOF simulation (Figure 5.7 d and i), also owing to relatively large value of Cn adopted in the PF simulation. In the experiment, Segers [176] found some very small gas residuals from the gas filament left beneath the cylinder (yet not shown in the experimental recordings there). Capturing sufficiently these tiny gas pockets requires extremely fine meshes and thus is not pursued in the present numerical investigation. Though such a residual gas bubble was found in his IBM-VOF simulation (Figure 5.7 j), Segers [176] also reports that such tiny bubbles cannot be resolved well numerically, owing to the limitation of mesh resolution.

5.3.4 Influence of Cylinder Wettability

To investigate the effect of the surface wettability of the cylinder, further simulations are made for other two equilibrium contact angles 30° and 90° in addition to 60° . Figure 5.8 juxtaposes the predicted bubble cutting process for these individual contact angles. Until $t = 0.11\text{s}$ the bubble deformation is still insensitive to the surface wettability (Figure 5.8 a, f and k). The influence of the wetting condition emerges at $t = 0.15\text{s}$. For $\theta_e = 30^\circ$, the gas has not yet touched directly the cylinder and a thin liquid film is found in-between (Figure 5.8 b) whilst a direct contact has arisen for $\theta_e = 90^\circ$ (Figure 5.8 l). This distinction can be attributed to the surface hydrophilicity: $\theta_e = 30^\circ$ corresponds to a more hydrophilic surface where the cylinder has a strong tendency to attract liquid rather than gas. This

also explains the distinction among the different cases at $t = 0.19\text{ s}$, where two daughter bubbles have been disconnected (Figure 5.8 c, h and m).

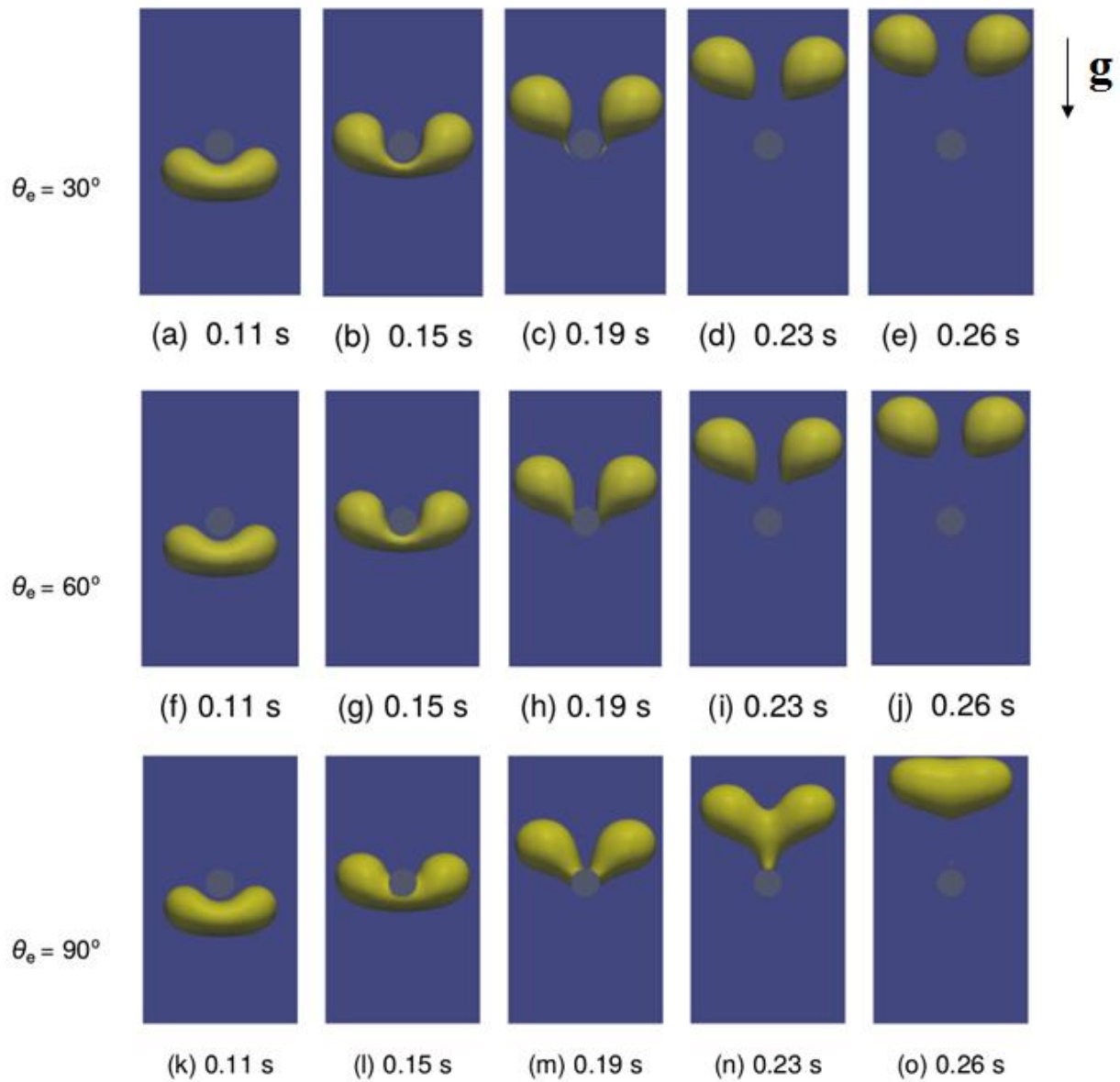


Figure 5.8: Bubble breakup process under differing surface wettability of the cylinder. Adapted from Cai et al. [138].

The simulations with $\theta_c = 30^\circ$ and $\theta_c = 60^\circ$ predict roughly the same evolution of the twin bubbles when they depart from the cylinder (Figure 5.8 d and i) and continue to rise (Figure 5.8 e and j). In the case $\theta_c = 90^\circ$, however, the daughter bubbles appear a very different behavior: because of a larger adhesion force on the gas exerted by the solid phase, the bubbles are being hold longer by the cylinder. The bottom ends of the daughter bubbles keep in direct contact with the cylinder surface and are sliding upwards over it (Figure 5.8 m). Eventually their lower ends meet and the twin bubbles are reunited to a single bubble (Figure 5.8 n). When the re-coalesced bubble gets detached from the cylinder, it is not axisymmetric (Figure 5.8 o); From a 3D perspective of the simulation (not shown in here), the bubble appears roughly ellipsoid-like where its dimension is much bigger perpendicular to the cylinder axis than parallel to the axis. Expectedly the bubble would be recovering to an axisymmetric one as it rises further. This process, however, is beyond the scope of the present numerical study since a higher computational domain is then needed.

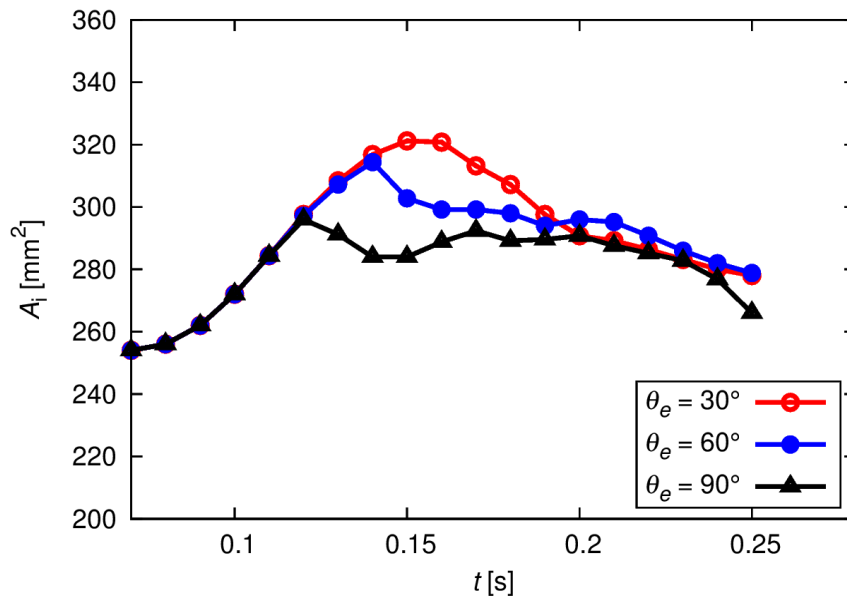


Figure 5.9: Influence of cylinder surface wettability on temporal evolution of bubble interfacial area during the bubble splitting process. Adapted from Cai et al. [138].

In Figure 5.9, one checks the effect of θ_c on instantaneous gas-liquid interfacial area A_i during the bubble deforming and break-up process. One may notice two characteristics. First, the peak value of A_i for $\theta_c = 30^\circ$ is larger than the other two cases. Second, for each case the moment of bubble break-up is indicated by the instant in time when the peak value of A_i arises (see Section 5.3.2). Judging from this, the bubble breaks up earliest for $\theta_c = 90^\circ$ and latest for $\theta_c = 30^\circ$. All these trends can be attributed to strengthening hydrophilicity and – meanwhile – weakening adhesion exerted by the solid onto the gas phase as θ_c is decreasing.

5.4 Bubble Rise through a Periodic Open Cellular Structure

With the numerical model, PF simulations of a bubble rising and deforming inside a periodic open cellular structure (POCS) are presented in this section. The investigation focuses on the wettability dependence of bubble interacting behavior with the POCS, since in Section 5.3.4 the wettability has been demonstrated to have a noticeable impact on solid cylinder-induced bubble deforming and splitting process.

5.4.1 Fluid Properties and Computational Set-up

In most industrial applications of bubble column reactors, the liquid phase is water, or its density/viscosity are similar to those of water. Hence, an air-water system is considered here. The physical properties of the two-phase system are: $\rho_L = 998 \text{ kg m}^{-3}$, $\rho_G = 1.205 \text{ kg m}^{-3}$, $\mu_L = 8.9 \times 10^{-4} \text{ Pa s}$, $\mu_G = 1.81 \times 10^{-5} \text{ Pa s}$ and $\sigma = 0.072 \text{ N m}^{-1}$; the corresponding Morton number is $Mo = 1.65 \times 10^{-11}$. The computational geometry (Figure 5.10) – as a representative domain of the POCS – was provided through a STL-format file by Institute of Chemical Reaction Engineering at FAU and Institute of Multiphase Flows at TUHH. To make sure head-on interactions of the vertically-rising bubble with the POCS struts, the whole computational geometry is inclined around the Y -axis by 45° away from the horizontal level, as shown in Figure 5.10.

As initial conditions, a spherical bubble ($D = 4$ mm and $Eu = 2.2$) is released in the lower part of the domain (Figure 5.11 a, b and c). To make the studied scenarios relatively general, the bubble center is slightly deviated from the vertical centerline of the domain, given that a perfect vertical alignment is rather rare for the collision of bubbles onto struts in real applications. The boundary condition setups are identical to those in the test case reported in Section 5.3. An isotropic mesh is generated for the given computational domain. The number of cells to resolve the bubble diameter D is $N_D = 25$; $Cn = 0.04$ and $Pe_c = 1000$ are used.

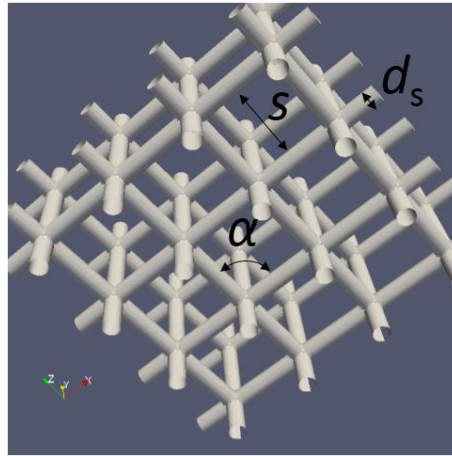


Figure 5.10: The representative domain of a POCS considered in the present simulation with window size $s = 4$ mm, strut diameter $d_s = 1$ mm and grid angle $\alpha = 90^\circ$. The whole structure is tilted by 45° . Adapted from Cai et al. [138].

5.4.2 Results

The study is devoted to revealing the influence of POCS surface wettability on bubble behavior. For this purpose, five simulations are carried out with the respective equilibrium contact angle θ_c being 0° , 30° , 60° , 90° and 120° in the present investigation. Figure 5.11 displays the simulated bubble-strut interacting process for $\theta_c = 0^\circ$, 90° and 120° in a 3D view. Due to buoyancy force, the bubble starts to go upward (Figure 5.11 a,

b and c) and arrives at the first horizontal strut in a short time. For these different θ_c (i.e. surface wettability) the subsequent processes of the bubble interacting with the strut appear very distinct to each other. In the case $\theta_c = 0^\circ$, the bubble is forming as a concave shape and trying to avoid direct contact with the horizontal strut (Figure 5.11 d). For $\theta_c = 90^\circ$ – by contrast – one observes a direct contact of the bubble not only with the horizontal strut but also with the lateral struts (Figure 5.11 e); this is attributed to an augmented tendency of the solid strut to hold the gas phase. For $\theta_c = 120^\circ$, such an aerophilic effect is even stronger so that the bubble is enwrapping the horizontal strut (Figure 5.11 f). For both the cases $\theta_c = 0^\circ$ and 90° the bubble keeps rising after its interaction with the first horizontal strut, yet showing different behaviors. For $\theta_c = 0^\circ$ the bubble is going up in a “detached” manner from the POCS struts, either being as an untouched ellipsoid (Figure 5.11 g and m) or being a cashew-like shape when it is getting close to the horizontal struts (Figure 5.11 j and p). For $\theta_c = 90^\circ$, however, an “attached” mode arises: the bubble is always touching directly horizontal/lateral struts as if it is a “ladder-climber” in the structure. The bubble dynamics for $\theta_c = 120^\circ$ differs essentially from the above two cases: instead of continuing to move upwards, the bubble is eventually hold by the POCS struts (Figure 5.11 l, o and r). This is due to a strong adhesion from the surface acting onto the bubble – under this surface wettability – which dominates over the upward buoyance force.

To make easier the analysis, a 2D view of the computational results is presented in Figure 5.12. There the case $\theta_c = 120^\circ$ is not shown anymore; rather the simulation results for $\theta_c = 60^\circ$ are displayed in addition to the cases $\theta_c = 0^\circ$ and 90° whose 3D views have been shown in Figure 5.11. The time-scale in Figure 5.12 is identical with that in Figure 5.11. The first trend to note in Figure 5.12 is that as θ_c decreases from 90° to 0° – for example, at $t = 0.045s$ – the concave shape is more noticeable (Figure 5.12 f, e and d).

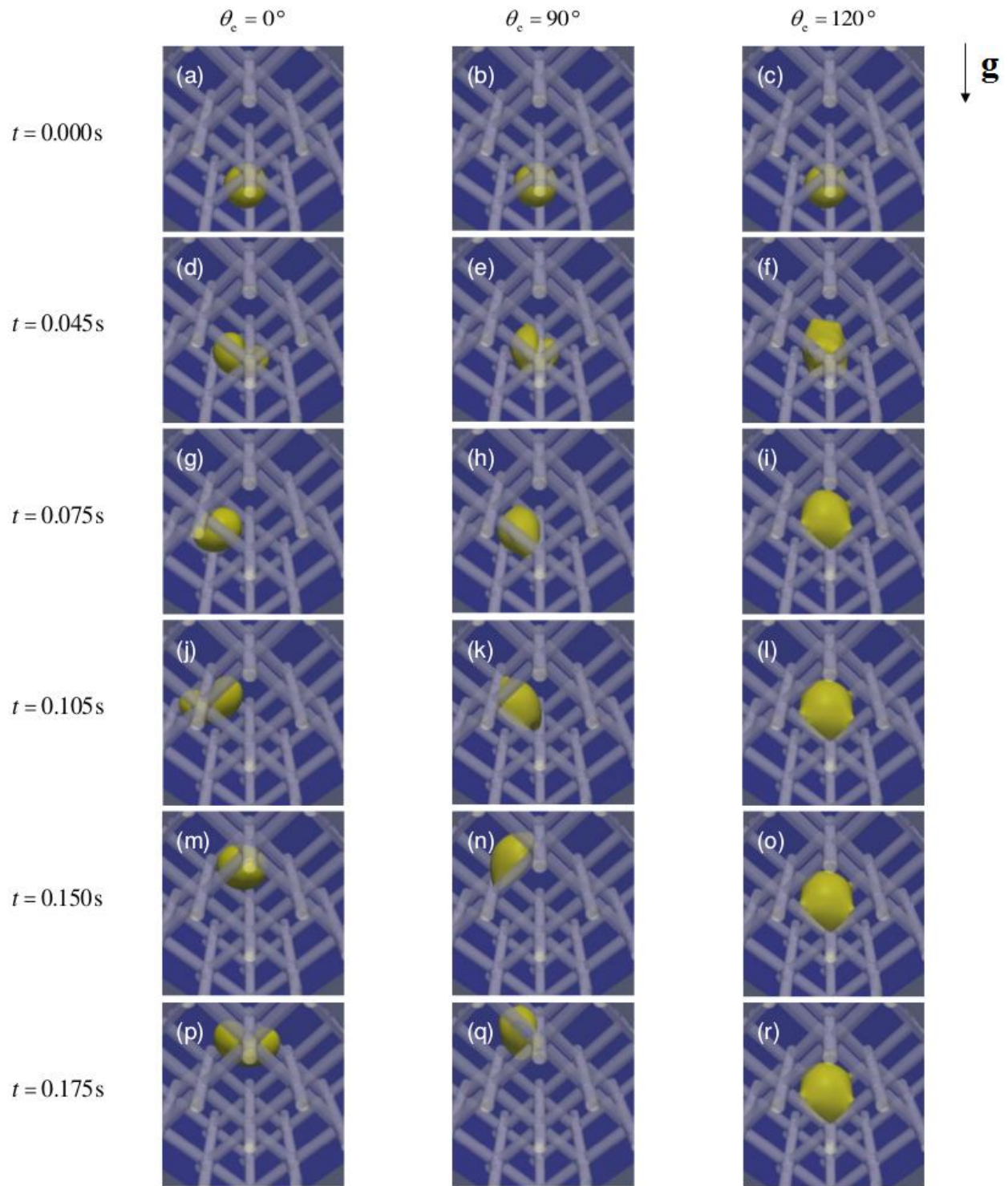


Figure 5.11: 3D view of the phase-field simulations of the bubble interacting process with the POCS under different surface wettability of the POCS. Adapted from Cai et al. [138].

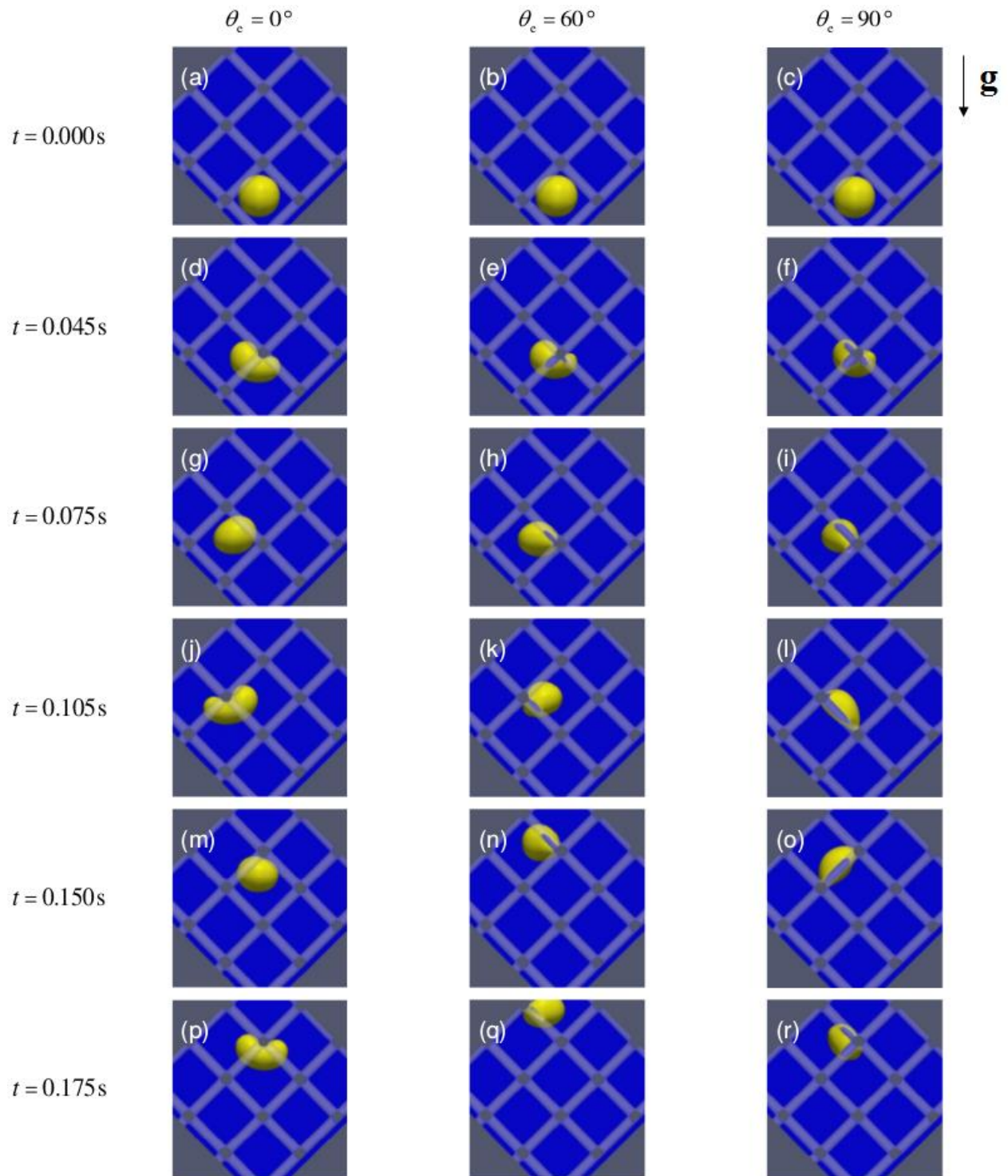


Figure 5.12: 2D lateral view of the phase-field simulations of the bubble interacting process with the POCS under different surface wettability of the POCS. Adapted from Cai et al. [138].

At subsequent temporal instants, cashew-like bubble shapes can be observed for $\theta_c = 0^\circ$ (Figure 5.12 j and p), but not for the other two contact angles $\theta_c = 60^\circ$ and 90° . For the latter two cases, on the other hand, the bubble shows direct contact with the horizontal and lateral struts whilst this phenomenon does not emerge for $\theta_c = 0^\circ$. In the present study a simulation with $\theta_c = 30^\circ$ is also performed and the results are roughly similar to those with $\theta_c = 0^\circ$; thus they are not shown here.

5.4.3 Discussion

The computational results in Section 5.4.2 have clearly shown that the bubble deformation and its rising path do largely depend on the surface wettability (i.e., equilibrium contact angle) of POCS struts. In this section, the practical implications of the results for industrial applications are discussed.

The numerical results for $\theta_c = 120^\circ$ suggest that hydrophobic POCS are unfit for internal structured packing in bubble column reactors, since a strong hydrophobicity-induced adhesion leads to the eventual bubble immobilization (Figure 5.11 l, o and r). Since a large number of bubbles (e.g. bubble swarms) are typically found in an industrial bubble column reactor, the bubble immobilization potentially gives rise to bubble agglomerates, where original small bubbles are forming larger bubbles through coalescence. This phenomenon should be avoided due to the following two reasons. First during bubble coalescence the total volume-specific gas-liquid interfacial area is declining, thereby lowering interfacial mass transfer rate. Second in many technical bubble column reactors, bubbles are purely or partly composed of oxygen. Large accumulations of oxygen (induced by structure surface hydrophobicity) may lead to explosions; such a potential security threat must be absolutely prevented in chemical plants.

In the case $\theta_c = 90^\circ$, the bubble is climbing up the struts and so is not captured by them. However, temporal bubble filling of a whole cell window (e.g. Figure 5.11 k and n)

may also result in unwanted cross-interaction and coalescence between bubbles in laterally neighboring cell windows. Therefore POCS with surface wettability $\theta_c = 90^\circ$ is also deemed as inappropriate for bubble column internals.

Although the distinctions among the cases $\theta_c = 60^\circ$, 30° and 0° are less marked than those among $\theta_c = 60^\circ$, 90° and 120° , several features can still be observed as θ_c varies from 60° to 0° ; all these favor the adoption of $\theta_c = 0^\circ$. First, as the equilibrium contact angle gets smaller, the bubble forms as a concave shape to a larger extent when it interacts with a horizontal strut. Such a deforming process of the bubble helps renew the concentration (species) boundary layer at liquid side. Therein liquid of smaller concentration profile can access to gas-liquid interface. Hence, interfacial concentration gradient becomes larger and thereby interfacial mass transfer speeds up. In this sense, the surface wettability $\theta_c = 0^\circ$ is preferred. Second, in the case $\theta_c = 0^\circ$ the bubble experiences alternating acceleration (in the middle of a cell window) and deceleration (when approaching a horizontal strut). Such a cyclic switch also improves interfacial mass transfer. Third, in the simulation of $\theta_c = 60^\circ$ the bubble shows a roughly rectilinear rising path when $t \geq 0.075\text{s}$. By comparison, for $\theta_c = 0^\circ$ one finds a zigzag-like trajectory of the bubble: after each head-on collision with horizontal struts, it gets re-bounced slightly and redirected from its previous course. Such a meandering pathway implies a lower effective rise velocity and accordingly a longer residence time; therewith a larger timeframe is given to certain mass transfer or chemical reactions.

Overall, adopting a more hydrophilic surface wettability (i.e. smaller equilibrium contact angle) creates a hydrodynamic condition that favors interfacial mass transfer enhancement. Besides, a more hydrophilic condition is preferred when the POCS serves as catalytic support for heterogeneous catalytic reactions. As the present computational results suggest, a thin liquid film forms between the bubble and solid strut with sufficiently hydrophilic wettability $\theta_c \leq 30^\circ$. This thin film implies that gaseous surfactants only need

to diffuse a very short path before they reach active catalytic sites on solid surface. Therefore the total system efficiency of a catalytic reaction is improved.

5.5 Summary of Chapter 5

In this chapter, the PF-based numerical model is first validated for the terminal rise velocity of a single bubble and its break-up behavior caused by a horizontal cylinder. The numerical results are found in good agreement with experimental data from literature. For the cylinder-induced bubble splitting process, the influence of surface wettability is numerically studied and it is shown to have a marked effect on bubble deforming and cutting behavior. Then the chapter presents numerical simulations of rising dynamics of an air bubble within a water-filled POCS. It is demonstrated that the POCS surface wettability largely affects bubble hydrodynamics behavior. By tuning a more hydrophilic surface, one can create a favorable hydrodynamic condition where interfacial mass transfer/heterogeneous catalytic reactions can be greatly enhanced.

6 Gas-liquid Two-phase Flows in Sponge Structures

In the previous chapters, the solid structures involved in the interfacial two-phase flows problems are relatively simple: either smooth surfaces or topologically regular structures. This chapter takes complicated geometry into account and presents applications of the numerical method for interface-resolving simulations of gas-liquid flows in complex and irregular sponge structure.

6.1 Introduction and Motivation

Solid sponges (also called open-cell foam in literature) are cellular three-dimensional network structures, as shown in Figure 6.1 a. They are characterized by high porosity, low pressure drop, large specific surface area, high heat and mass transfer rates as well as favorability for catalytic activity [10, 180-183]. These advantages make sponge structures very attractive as internal packing for innovative chemical reactors [6]. Such sponge-packed reactors usually involve gas-liquid two-phase flows, where gas-liquid reactions (such as oxidation, hydrogenation, hydrodesulfurization) take place [184]. For reactions in multiphase systems, reactor efficiency is largely determined by interfacial mass transfer rate [10]. For enhancing the latter, gas-liquid interfacial area is a deciding factor among others. Thus, it is beneficial to gain deep understanding of two-phase hydrodynamics and quantitative knowledge of gas-liquid interfacial area for design and optimization of such sponge-packed multiphase reactors.

In recent years, CFD has developed into a very valuable and promising tool to obtain insights into two-phase hydrodynamics in sponge structure or specifically for the sponge-packed reactor. The majority of the CFD simulations in literature are based on volume-averaging models, e.g. [185-189]. They are able to predict such macroscopically effective hydrodynamic properties as liquid-phase holdup and pressure drop but could not resolve flow physics at local scales, considering the nature of averaging procedures. A few

references have reported local-scale resolving simulations: for example, the pore-scale numerical studies by Amiri and Hamouda [190, 191] and Fichot et al. [192] considered 2D idealized and structured porous geometries; although Liu and his colleagues [193-195] performed pore-scale simulations for 3D complex and irregular porous media, they did not attempt to resolve gas-liquid interface. As of now, no CFD simulations for resolving gas-liquid interface in complex sponge structure have been found in literature. The present study is a first attempt to fill this gap.

The reason why most CFD investigations were performed with averaging models rather than direct numerical solution lies in a large disparity of different length scales involved. They could cover at least three orders-of-magnitude for gas-liquid two-phase flows in sponge structure: the dimensions of a sponge element are usually on the order of $O(10^2)$ mm (Figure 6.1), individual liquid jets of $O(1)$ mm scale and local gas-liquid interface of $O(10^{-1})$ mm scale (Figure 6.1 a). For interface-resolving simulations, computational efforts could be prohibitively large if one considers the whole sponge structure. In the present numerical study, a representative elementary volume (REV) of sponge structures is considered instead in order to save the computational cost. To obtain a physical liquid phase distribution for such a REV, a modeling strategy is proposed and developed by mirroring computational domain and decomposing physical pressure for use of periodic conditions. With this modelling concept, numerical simulations are carried out to reveal influences of physical parameters (i.e. liquid saturation, structure wettability and interfacial tension) on gas-liquid interfacial area. Such detailed insights gained from the present computational studies are of great use for characterization of local interfacial phenomena in complex solid sponge structure.

The remainder of this chapter is organized as follows. In Section 6.2, the numerical method is validated for its predictive capability for gas flow hydrodynamics in an alumina sponge structure. Section 6.3 presents interface-resolving simulations of gas-liquid flows

in a SiSiC sponge structure and provides a detailed discussion on the results. Conclusions are given in Section 6.4.

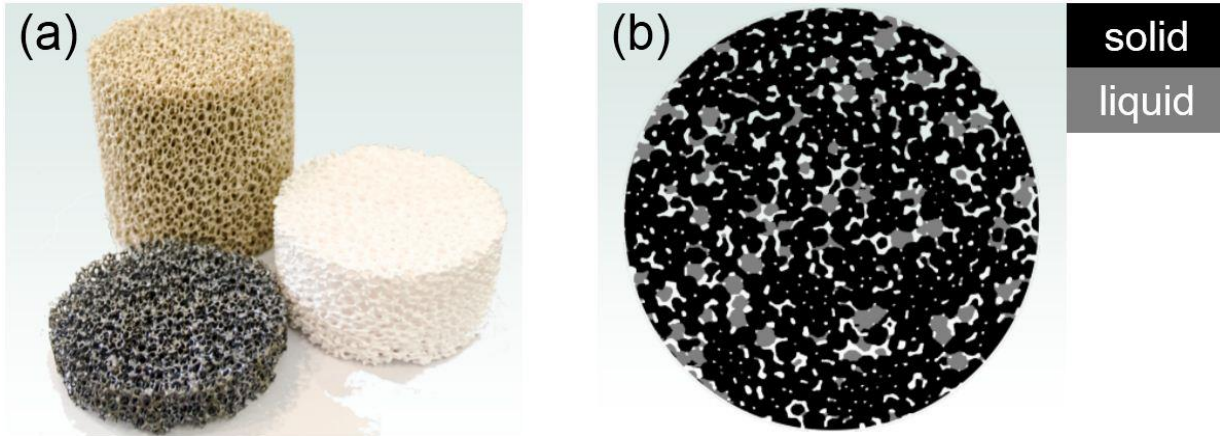


Figure 6.1: (a) Sponge structures made of different materials: silicate (top), alumina (right) and silicon infiltrated silicon carbon (SiSiC) (bottom). (b) Cross-cut view of a SiSiC sponge in a working operation with gas-liquid flows. Within the cross-sectional circle, black and gray stand for solid and liquid respectively while the rest is for gas. Both figures (a) and (b) are from Wallenstein et al. [13].

6.2 Validation for Single-phase Gas Flow in Sponge Structure

In this section, the general capability of the numerical method to reproduce accurately hydrodynamics in sponge structure is examined. For this purpose, the method is used to recalculate pressure drop of single-phase gas flow in an alumina sponge and the results are compared with experimental data from Dietrich et al. [181] and reference numerical results from Meinicke et al. [196].

6.2.1 Computational Geometry and Mesh

The computational geometry of a cubic REV sponge structure is shown in Figure 6.2. It was provided by Institute of Thermal Process Engineering (“Institut für Thermische

Verfahrenstechnik” in German), KIT. The procedure of the geometry generation included μ CT scanning of the sponge sample and subsequent geometry reconstruction using the commercial software MATLAB. Further details can be found in Meinicke et al. [196].

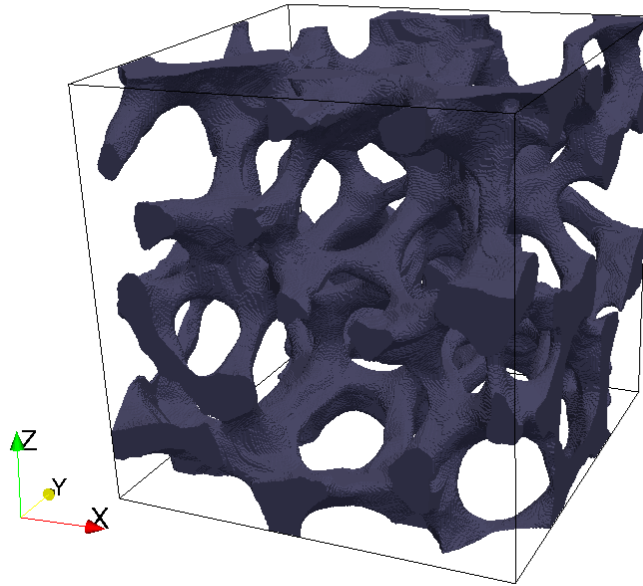


Figure 6.2: Cubic REV of an alumina sponge with porosity $\psi := V_{\text{void}}/V_{\text{REV}} = 80\%$, 20 pores per inch (ppi) and edge length $a = 6\text{mm}$.

The computational mesh for the REV geometry is then generated with the following procedure: firstly, the background (relatively coarse) grid for bulk regions is produced with *blockMesh* utility; subsequently, the mesh near solid sponge surfaces is refined with *snappyHexMesh* utility. Figure 6.3 shows an example mesh from 3D and cross-cutting view respectively. The grid cell size for the bulk region is $h = 0.2\text{ mm}$ with mesh refinement of two levels near the solid sponge surface, i.e., the smallest cell size in the vicinity of the wall is $h = 0.05\text{ mm}$. The preliminary studies have showed that the grid resolution of the example mesh is sufficient to deliver grid-independent results of pressure-drop prediction

in the present test case. Thus, this mesh resolution will be used throughout the validation for single-phase gas flows.

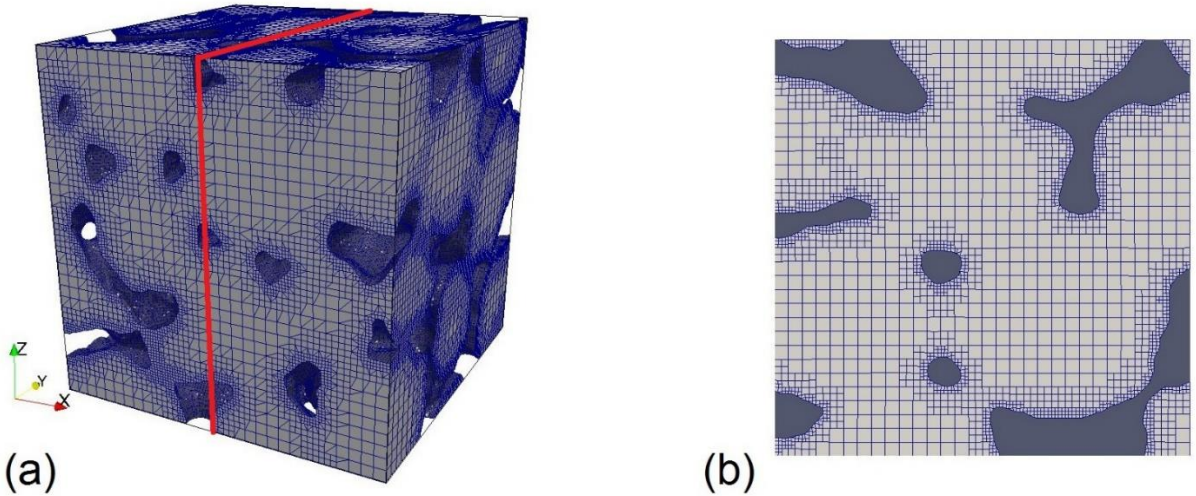


Figure 6.3: (a) 3D view of computational mesh for the cubic REV sponge geometry. (b) Cross-cutting view of the mid-plane outlined in red in (a). The solid region is shown in dark gray while the flow region in light gray. The mesh cell size for the bulk region is $h = 0.2$ mm and mesh refinement of two levels is made near the solid sponge surface.

6.2.2 Physical Properties and Computational Set-ups

Dietrich et al. [181] investigated experimentally isothermal gas hydrodynamics in alumina sponge ($\psi = 80\%$ and 20 ppi). In the experiment, pressure drop per unit length $\Delta p / \Delta x$ was measured for varying superficial inlet velocity U_0 . With the same physical and operating conditions, Meinicke et al. [196] numerically reproduced the experimental data with *simpleFoam*, a standard OpenFOAM® solver for single-phase, incompressible and steady-state flow. In this section, the computational results with the numerical model developed in this PhD study is compared to the experimental data and simulation results mentioned above.

In the present numerical simulations, the gas density and viscosity are $\rho_G = 1.0 \text{ kg m}^{-3}$ and $\mu_G = 1.726 \times 10^{-5} \text{ Pa s}$, the same as those in the experiment [181] and simulation [196]. As introduced in Section 2.1, PFM is originally developed for interfacial two-phase flows problems. When it is used for the current simulation of single-phase gas flow, the order parameter is set to $C = -1$ (i.e., for the gas phase) everywhere in the computational domain. The interfacial or phase-field specific parameters (such as the interfacial tension coefficient σ , interfacial thickness parameter ε and mobility κ) are irrelevant to the single-phase simulations.

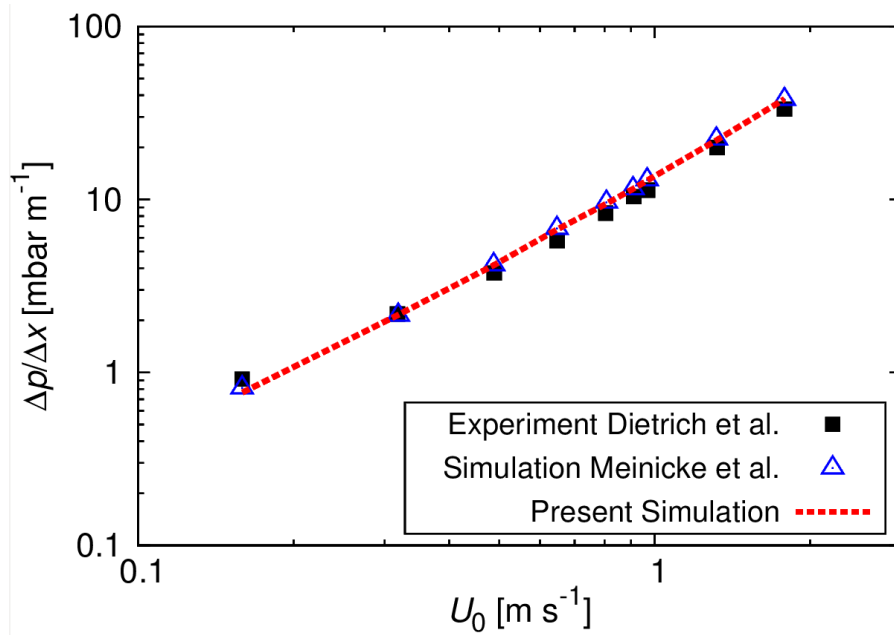


Figure 6.4: Comparison of the present simulation results with the experimental data from [181] and *simpleFoam* numerical solution from [196], with respect to pressure drop per unit length $\Delta p / \Delta x$ versus superficial gas velocity U_0 for the alumina sponge.

The boundary conditions are set similar to Meinicke et al. [196]: a certain physical velocity ($U_{\text{phy}} = U_0 / \psi$ with $\psi = 80\%$) is specified at the inlet patch, zero relative pressure

at the outlet and free-slip boundary condition at the four side patches. All the simulations are started from an initial condition with a uniform axial velocity U_{phy} in the computational domain. For the order parameter field, zero gradient conditions are applied to all the boundary patches.

6.2.3 Comparison with Reference Experimental and Computational Results

In Figure 6.4, the present simulation results for pressure drop per unit length $\Delta p / \Delta x$ versus superficial gas velocity U_0 are compared with the experimental data from [181] and *simpleFoam* simulation results from [196]. An excellent agreement is found. There U_0 varies from 0.159 to 1.784 m s⁻¹ and the resulting $\Delta p / \Delta x$ from 0.813 to 37.749 mbar m⁻¹; within this range, the gas flow is assumed to be laminar [196]. As all the results suggest, pressure drop per unit length rises as superficial gas velocity increases, a trend first noted by Ergun and Orning [197].

6.3 Interface-resolving Simulation of Two-phase Flows in Sponge Structure

In this section, the numerical method is applied for interface-resolving simulations of gas-liquid two-phase flows in a REV of SiSiC sponge, since this sponge type is of special interest to the research activities of the German Helmholtz Energy Alliance “Energy Efficient Chemical Multiphase Processes” [143]. For proper handling of periodicity of the REV, a special modeling strategy is introduced. Based on this, a series of numerical simulations are performed and the results concerning resolved gas-liquid interface are discussed.

6.3.1 Modelling Strategy

The aim of the interface-resolving simulations is to predict physical gas/liquid distribution and corresponding gas-liquid interfacial area within a REV domain under a given set of physical and operating conditions. To make sufficiently representative such

REV-based simulations of two-phase flows and especially phase distributions, one might consider to use periodic (also called as cyclic) boundary condition. But the application of this type BC into an irregular sponge REV is not straightforward. There one should take special cares to the following two points:

First, when a pair of boundary patches are set to periodic, they will be treated as if they are physically connected. Thus, each pair should have the same geometry to ensure continuity of topology. Although this geometrical constraint can be readily met for cuboid/cylinder domain without sponge structure or those with regularly structured sponge, it is not the case for complex and irregular sponge REV considered in the present study. As shown in Figure 6.2, boundary faces differ in geometry from each other.

Second, flow variables (e.g. velocity and pressure) at each periodic pair should be the same and part of numerical solution. This requirement poses two challenges to the conventional solution with the Navier-Stokes equations. On the one hand, if the pressure field is the same at a periodic pair of boundary faces, there is no pressure drop and thus no driving force for flow. On the other hand, for experiments or conventional CFD simulations, it is usual to specify a fixed inlet velocity/flow rate for a boundary patch at one end and then measure or simulate the resulting pressure drop, as shown in the previous validation for single-phase gas flow (cf. Section 6.2). However, it is impossible to do so for simulations with periodic conditions since velocity field at periodic pair can only be solved by the numerical simulations rather than be specified as an input.

To handle properly the two points above, a modelling concept is introduced. In order to have a cyclic pair of faces with the identical geometry, the original SiSiC sponge REV (Figure 6.5 a) is mirrored with respect to the red-outlined plane perpendicular to x - coordinate. In the resulting REV (Figure 6.5 b), the two boundary faces at $\mathbf{x}=0$ and $\mathbf{x}=a \mathbf{e}_x$ are exactly same in geometry so that periodic conditions shall be easily set to them. To deal with the second point above, physical pressure is split into two parts:

$$p \equiv P - \frac{\overline{p_0} - \overline{p_a}}{a} \mathbf{e}_x \cdot \mathbf{x} = P - \mathbf{f}_x \cdot \mathbf{x} \quad (6.1)$$

where $\overline{p_0}$ and $\overline{p_a}$ are the plane-averaged pressure at the plane $\mathbf{x}=0$ and $\mathbf{x}=a \mathbf{e}_x$ respectively, and P is termed as reduced pressure. By averaging Eq. (6.1) across the planes $\mathbf{x}=0$ and $\mathbf{x}=a \mathbf{e}_x$ respectively, one obtains:

$$\overline{p_0} = \overline{P} \quad (6.2)$$

$$\overline{p_a} = \overline{P_a} + \overline{p_a} - \overline{P_0} \quad (6.3)$$

Combining Eqs. (6.2) and (6.3), one reaches the following relation:

$$\overline{P_a} = \overline{P_0} \quad (6.4)$$

Equation (6.4) shows that the reduced pressure P is periodic with respect to the edge length a .

On the other hand, substituting Eq. (6.1) into the pressure gradient in Eq. (2.9), one obtains a modified N-S equation as follows:

$$\rho_c \left(\frac{\partial \mathbf{u}}{\partial t} + (\mathbf{u} \cdot \nabla) \mathbf{u} \right) = -\nabla P + \mathbf{f}_x + \nabla \cdot \left[\mu_c \left(\nabla \mathbf{u} + (\nabla \mathbf{u})^T \right) \right] + \mathbf{f}_\sigma \quad (6.5)$$

With the modified N-S equation, the reduced pressure P will be actually used in numerical simulations so that the cyclic condition is met, as shown in Eq. (6.4). On the other hand, a pressure drop per unit length for the REV can be specified explicitly as a body force $\mathbf{f}_x = ((\overline{p_0} - \overline{p_a})/a) \mathbf{e}_x = (\Delta p / \Delta x) \mathbf{e}_x$ and as a result, a flow along the direction \mathbf{e}_x will be driven by the pressure drop in the simulations. Considering the range of pressure drop and resulting velocity investigated in the present study, the two-phase flow is assumed to be laminar. Thus, one would expectedly achieve a steady-state two-phase flow characterized by a fixed superficial velocity U_0 and interfacial area A_{eff} . It is noted that Ghidersa [198] and Öztaskin et al. [199] among other research groups already employed the above pressure-decomposition method for two-phase interfacial simulations on periodic domains but they considered only simple cuboid domains.

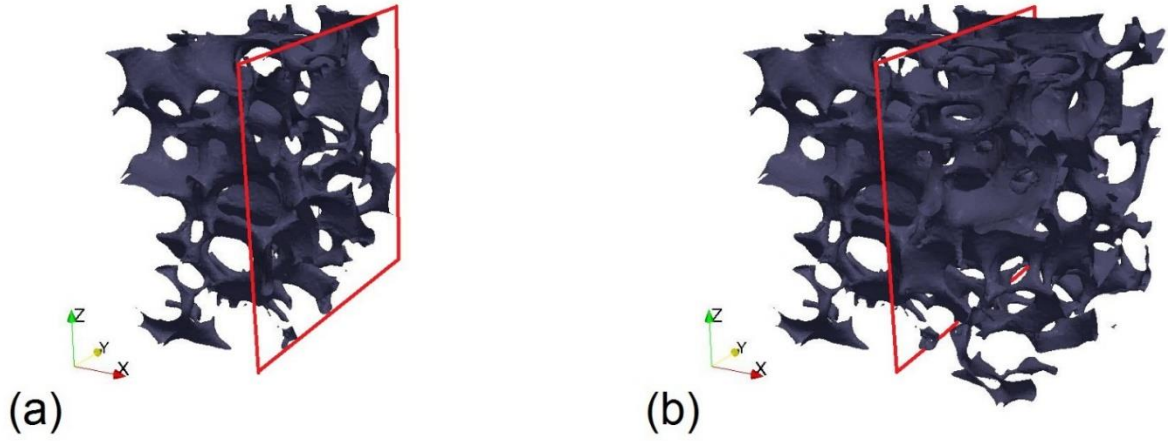


Figure 6.5: (a) Original SiSiC sponge REV geometry with $\psi = 85\%$ and 20 ppi was provided by Institut für Thermische Verfahrenstechnik, KIT [196]. (b) Cubic REV geometry ($a = 10$ mm) obtained through the mirroring process with respect to the red-outlined plane perpendicular to x -coordinate.

6.3.2 Physical Properties and Computational Set-ups

The present interface-resolving simulations consider an air-water two-phase flow system with the following physical properties: $\rho_G = 1.0 \text{ kg m}^{-3}$, $\mu_G = 1.726 \times 10^{-5} \text{ Pa s}$, $\rho_L = 998 \text{ kg m}^{-3}$ and $\mu_L = 8.9 \times 10^{-4} \text{ Pa s}$. To quantify liquid phase holdup, liquid saturation β is defined as $(V_L)/(V_L + V_G) = V_L / V_{\text{void}}$ where the sum of liquid volume V_L and gas volume V_G amounts to the total void volume of the REV V_{void} . To determine β , V_{void} is fixed through $V_{\text{void}} = \psi V_{\text{REV}}$ and V_L is calculated as:

$$V_L = \iiint_{C>0} 1 \, dx \, dy \, dz \quad (6.6)$$

For the baseline simulation shown in Figure 6.6, liquid saturation $\beta = 0.17$, equilibrium contact angle $\theta_e = 90^\circ$ and interfacial tension $\sigma = 72 \text{ mN m}^{-1}$. Here the phase-field specific parameters are chosen as follows: $Cn = 0.02$ where the characteristic length scale is chosen as $L = a$, $Pe_C = 2500$ and $N_C = 4$.

As discussed in Section 6.3.1, the two boundary faces at $\mathbf{x}=0$ and $\mathbf{x}=a \mathbf{e}_x$ are set to a periodic pair. At the four side patches, symmetry conditions are applied. On the sponge surface, no-slip boundaries are employed for the velocity and wetting boundary conditions with a prescribed equilibrium contact angle θ_e for the order parameter, cf. Eq. (2.7).

In all the simulations in this study, the pressure drop per unit length $\Delta p/\Delta x$ as an input to the computations is fixed to 500 Pa m^{-1} . For phase distribution initialization, a cylindrical liquid column with $\beta = 0.17$ is specified, as shown in Figure 6.6 a.

6.3.3 Results and Discussions

6.3.3.1 Dynamic Process Approaching Equilibrium State

The baseline simulation of achieving equilibrium state of two-phase distribution is shown in Figure 6.6. Due to the specified pressure drop along x -coordinate, a flow arises in this direction. Driven by a combined effect of fluid flow and capillarity, the initially cylindrical liquid column (Figure 6.6 a) is starting to evolve (Figure 6.6 b) and gradually converging to the equilibrium state (Figure 6.6 f).

For this baseline case, a mesh dependence study is made. For $Cn = 0.02$ and $Pe_C = 2500$, the simulation results from different mesh resolution $N_C = 2, 4$ and 8 are compared with respective to predicted evolution of liquid saturation β and gas-liquid effective interfacial area A_{eff} , as shown in Figure 6.7. A_{eff} is defined as the gas-liquid interfacial area normalized by the total volume of the REV $V_{\text{REV}} = 10^{-6} \text{ m}^3$. Since the periodic conditions are applied, the liquid volume should be conserved over time so that liquid saturation be constant. This is observed well by the simulations with $N_C = 4$ and 8 but a noticeable loss of liquid mass is found if $N_C = 2$ (Figure 6.7 a). When one checks effective interfacial area A_{eff} (Figure 6.7 b), $N_C = 4$ is shown to be a good compromise between accuracy and computational cost. Therefore, this mesh resolution will be kept in the following simulations.

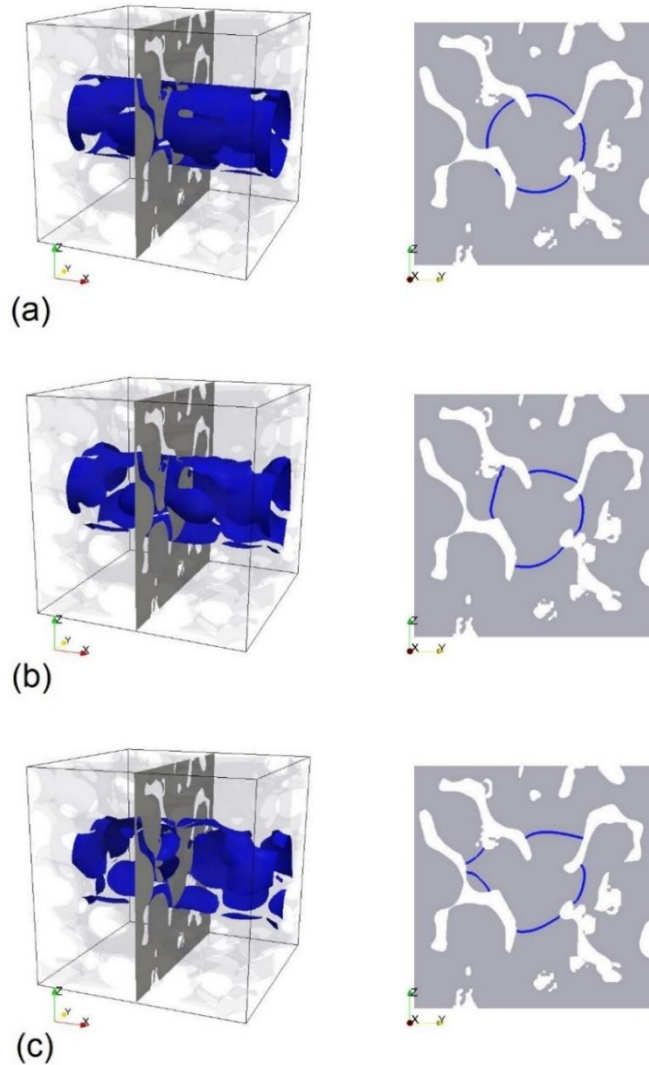


Figure 6.6: Baseline simulation of gas-liquid two-phase flows at (a) initial state $t = 0$ s, (b) $t = 0.005$ s, (c) $t = 0.02$ s, (d) $t = 0.025$ s, (e) $t = 0.03$ s and (f) equilibrium state $t = 0.05$ s in the REV ($a = 0.01$ m) of SiSiC sponge. The equilibrium contact angle is $\theta_c = 90^\circ$. In the 3D images shown on LHS, the sponge structure is shown as semi-transparent to facilitate visualization of the gas-liquid interface denoted by the blue iso-surface. On RHS are the corresponding cross-cutting views for the gray mid-plane shown in the respective LHS images.

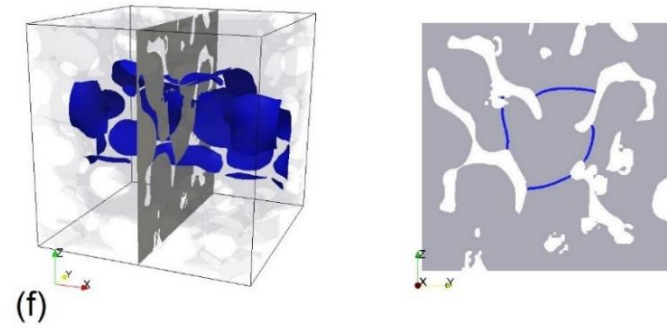
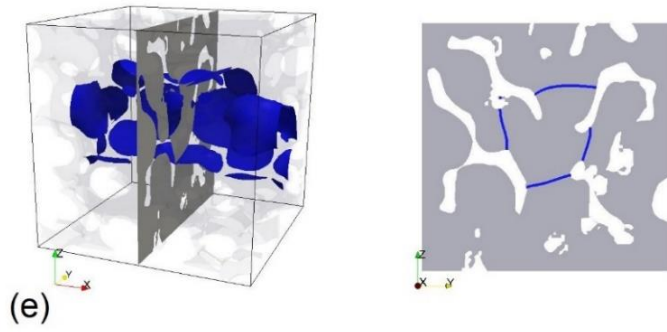
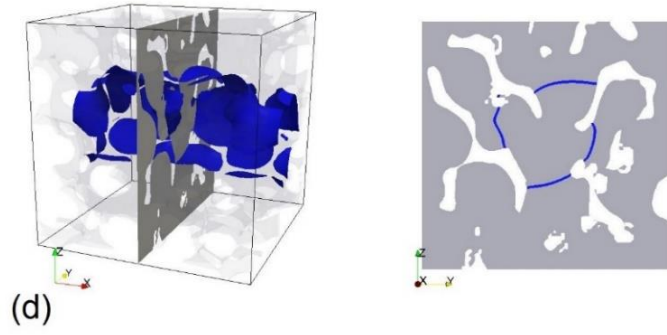


Figure 6.6: Continued.

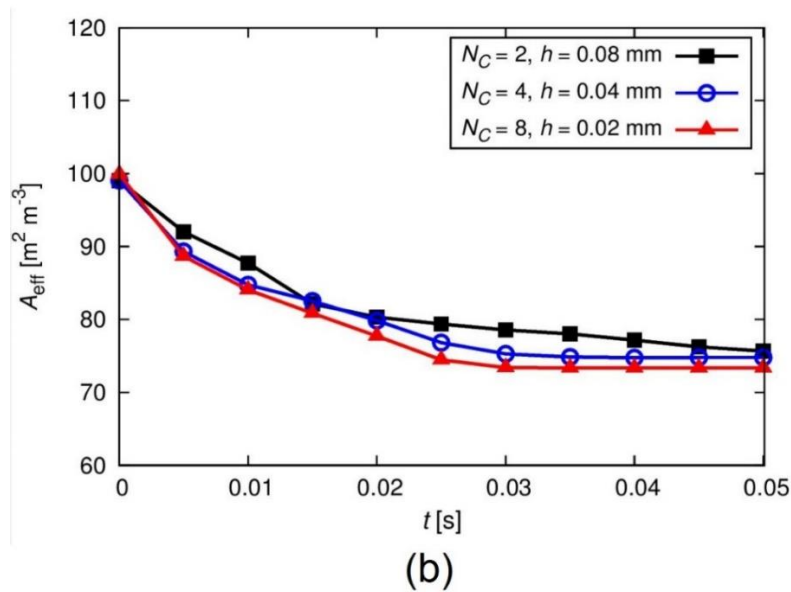
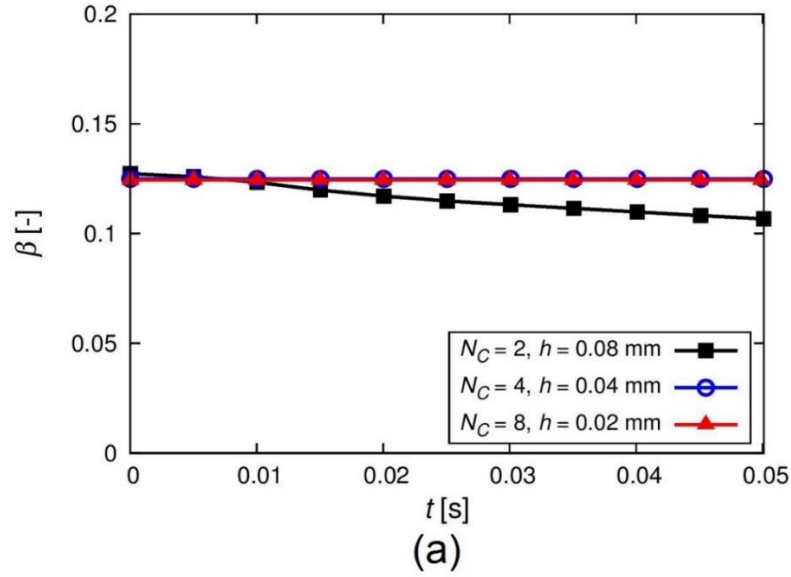


Figure 6.7: Influence of mesh resolution on predicted evolution of (a) liquid saturation β and (b) gas-liquid effective interfacial area A_{eff} with $Cn = 0.02$ and $Pe_C = 2500$.

6.3.3.2 Influence of Surface Wettability and Interfacial Tension

The respective influence of surface wettability and interface tension is studied by examining simulation results at equilibrium state. As reported by Große [200], most sponge structures used as internal packing for multiphase chemical reactors have

hydrophilic surfaces. Thus, the current numerical investigation on surface wettability considers only hydrophilic regime.

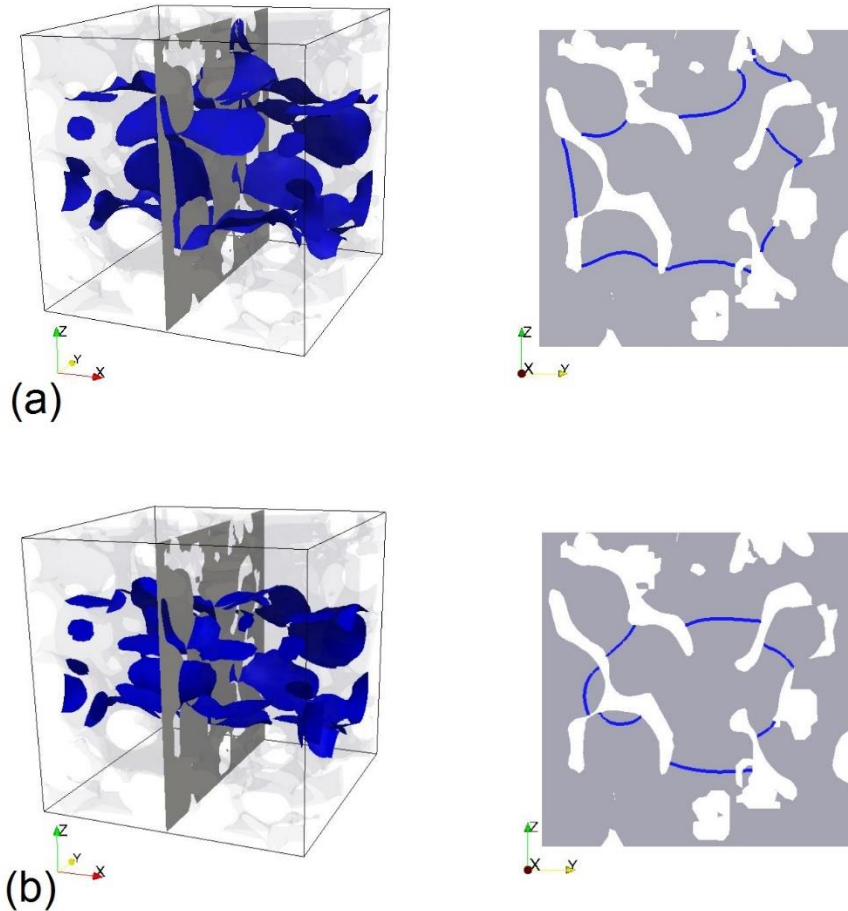


Figure 6.8: Equilibrium state liquid distribution on sponge of surface wettability (a) $\theta_c = 40^\circ$ and (b) $\theta_c = 90^\circ$. In the both cases the liquid saturation is $\beta = 0.282$.

Figure 6.8 shows the comparison of simulated equilibrium liquid distribution with two different wettability $\theta_c = 40^\circ$ and $\theta_c = 80^\circ$. It is clearly seen from the cross-cutting view that a more hydrophilic surface ($\theta_c = 40^\circ$) exhibits a higher favorability for liquid spreading around within the structure. In Figure 6.9, the effect of surface wettability, i.e., equilibrium

contact angle θ_e , on gas-liquid interfacial area is quantitatively checked. For a certain β , increase of wettability (i.e. decrease of θ_e) leads to increase of gas-liquid effective interfacial area A_{eff} . Another trend worth noting is that for a given θ_e , as β gets larger, A_{eff} rises. This is reasonable since a bigger liquid volume amounts to a larger interfacial area.

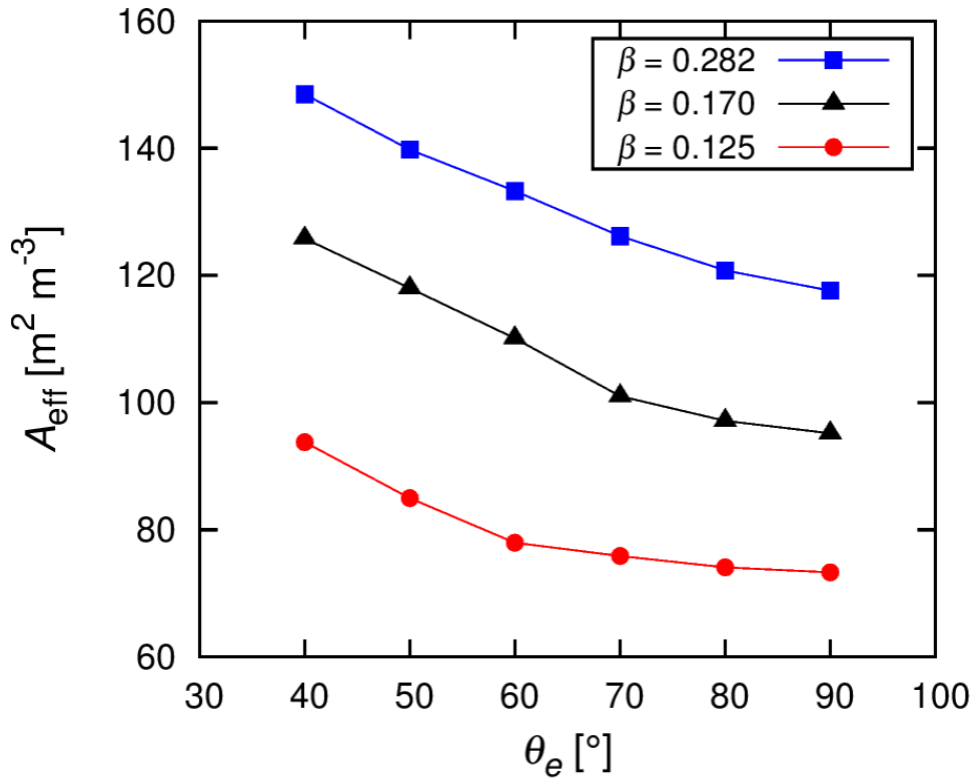


Figure 6.9: Influence of equilibrium contact angle θ_e on gas-liquid effective interfacial area A_{eff} for different liquid saturation β . The interfacial tension is $\sigma = 72 \text{ mN m}^{-1}$.

In addition to equilibrium contact angle, the influence of interfacial tension is also investigated. For this purpose, numerical studies are carried out for five different values of interfacial tension σ as 72, 62, 52, 42 and 32 mN m^{-1} . According to the Young's equation (1.2), the corresponding equilibrium contact angle is 70°, 66.6°, 61.7°, 54.1°

and 39.7° . As shown in Figure 6.10 for a certain β , as σ diminishes from 72 to 32 mN m^{-1} , A_{eff} increases by up to 30% ~ 40%. This numerical finding on the effect of σ on A_{eff} is substantiated by the experiment study by Stemmet et al. [11].

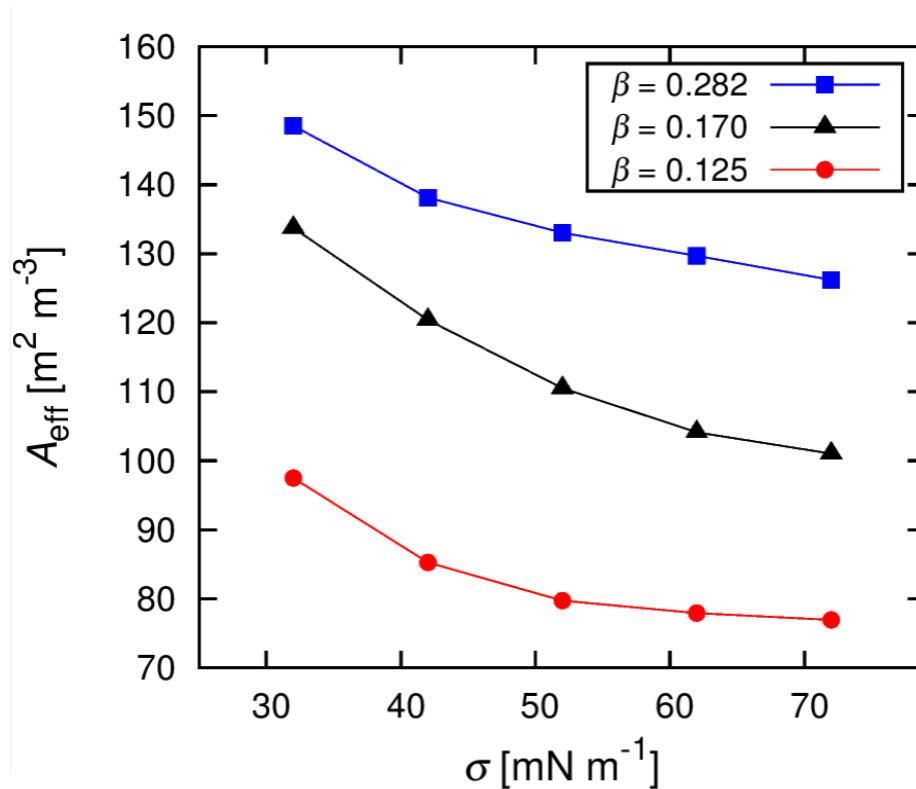


Figure 6.10: Influence of interfacial tension coefficient σ on gas-liquid effective interfacial area A_{eff} for different liquid saturation β . The corresponding equilibrium contact angle θ_e is varied with σ as prescribed by the Young's equation (1.2).

The present numerical results shown in Figure 6.9 and Figure 6.10 give a clear evidence that contact angle and interfacial tension are two factors which can be tuned to increase interfacial area and thus enhance interfacial mass transfer of two-phase flows in sponge structure. The adjustment of the former can be achieved by surface coating technology while that of the latter by addition of surfactants which gives rise to interfacial tension decrease.

6.4 Summary of Chapter 6

This chapter presents the application of the developed numerical method for interface-resolving simulations of gas-liquid two-phase flows in REV sponge structures. Firstly, the method is validated for its predictive capability of reproducing hydrodynamics in sponge structure, by recalculating pressure drop of gas flow in an alumina REV sponge. The results are shown in a very good agreement with reference experimental and numerical data in literature. Then the method is used to numerically resolve gas-liquid interface for a SiSiC sponge. The numerical simulations are carried out with a modeling concept of domain mirroring and pressure decomposition. The present computational results provide a clear evidence that interfacial area is greatly influenced by surface wettability and interfacial tension. By increasing surface wettability or decreasing interfacial tension coefficient, one can obtain an enlarged interfacial area and thus expect a considerable enhancement of interfacial mass transfer.

The present numerical investigation is a pioneering work that demonstrates the possibility of interface-resolving simulations for two-phase flow in complex sponge structure with reasonable computational cost. As shown in the current study, these interface-resolving simulations enable characterization of local interfacial behavior as well as detailed investigation into influences of liquid properties and operating conditions on interfacial phenomena.

7 Summary and Outlook

7.1 Summary and Conclusion

This PhD thesis presents interface-resolving numerical investigations of two-phase flows interacting with elementary and complex solid structures. For this purpose, a novel top-level solver (named as *phaseFieldFoam*) is developed and implemented in foam-extend. There, a phase-field description for interface evolution – i.e., the Cahn-Hilliard (CH) equation – is coupled with the two-phase Navier-Stokes equations in single-field formulation. The numerical method/code has been verified and validated through a series of test cases for interfacial two-phase flows. These include phase-field diffusion, droplet deformation in shear flow, capillary rise in vertical narrow channel, droplet wetting on chemically homogenous and heterogeneous substrates. The computational results are in good agreement with corresponding analytical and experimental data. Also the capability of the numerical code for 3D simulations with adaptive mesh refinement near interface is demonstrated.

With these successful validations and applications for two-phase interfacial flows on elementary surfaces, the numerical method/code is further employed to investigate interfacial dynamics within periodic open cellular structures (POCS). Of special focus in the present study is wettability dependent interaction of rising bubble with a POCS. Based on the numerical method/code, a numerical model is developed and first validated for terminal bubble rise velocity and instantaneous cylinder-induced bubble cutting behavior, by comparison with experimental data from literature. Then the numerical model is employed to study the behavior of a single air bubble rising through a representative subdomain of a POCS filled with stagnant water. The present numerical simulations clearly demonstrate that bubble deformation and rising path are largely determined by surface wettability of POCS. As the results suggest, the use of POCS with high surface

wettability (i.e. low equilibrium contact angle) is expected to favor mass transfer enhancement and catalytic gas-liquid reactions.

Also with the numerical method/code, local two-phase interfacial flows in heterogeneous sponge structures are studied. After the numerical model is validated for its predictive capability for gas flow hydrodynamics in alumina sponge structure, it is applied to interface-resolving simulations of gas-liquid two-phase flows in a SiSiC REV. To guarantee physical liquid phase distribution in the REV, a modeling strategy is developed by mirroring the REV and imposing periodic boundary conditions. Qualitative and quantitative investigations are performed to reveal influences of physical parameters on gas-liquid interfacial area. The numerical results clearly show that increasing surface wettability and decreasing interfacial tension coefficient are two means to enlarge interfacial area and in turn to enhance interfacial mass transfer.

All the results show that the PFM-based numerical code and model developed in this work are reliable, accurate and efficient computational tools that enable scale-resolving investigations on interfacial two-phase flows interacting with solid structures.

7.2 Outlook and Future Work

The present numerical model for droplet spreading process can be potentially used to explore some more complicated wetting phenomena, e.g. droplet impact onto surface from liquid spray or droplet moving on micro-structured surface. Besides the present model is suited to study droplet-droplet interactions – such as breakup and coalescence – on solid surfaces, which are found in many industrial micro-fluidics applications.

The present investigation on interaction of a rising bubble with single cylinder and POCS motivates several future works. Since no experimental studies on wettability-dependency of bubble interacting behavior with solid structures have yet been reported in literature, the experimental work on this area would be highly expected, so that the current

numerical findings on the surface wettability effect would be confirmed and the present numerical model be further validated. Then the numerical model can be applied to investigate the influences of other physical/geometrical factors (e.g. interfacial tension coefficient, bubble terminal velocity, relative size of bubble to solid cell window, etc.) on bubble dynamics interacting with solid structures as well as to study multi-bubble interactions (coalescence and breakup) commonly occurring in industrial bubble column reactors.

It is hoped that the present study on interface-resolving simulations of gas-liquid flows in sponge structure will stimulate further research activities in the scientific community. First, detailed experimental observation and measurement of local interfacial phenomena in sponge structure are highly needed to enable one-to-one comparison of experimental and numerical data, and the present numerical model could be further validated for its interface-resolving capability. Besides, with the numerical model one will be able to study the effects of other physical properties and characterize corresponding local interfacial phenomena in complex solid sponge structure, which is rather challenging or simply too costly to access experimentally. Moreover, the current local-scale-resolving simulations could be employed to develop closure relations used in macroscopic models, such as Euler-Euler method-based modeling, for engineering CFD simulations of multiphase hydrodynamics and interfacial mass transfer on a whole reactor scale.

All the PF simulations in the present study are performed with the equilibrium contact angle model. In future, dynamic contact angle models can be used, where dynamic contact angle is a function of contact line speed. With this, further complex moving contact line phenomena – such as contact angle hysteresis effect – can be computationally studied with the present numerical method. In the current study, the phase-field-specific parameters – especially the mobility parameter – are chosen in a rather empirical manner.

In future works, a strictly-founded methodology for fixing these parameters may be explored.

The outlook also includes further works on numerical aspects. One of them is about quantitative investigations into influences of numerical/physical parameters on volume conservation and boundedness. Besides, as an attempt to explore possibilities of further optimizing computational efficiency, dynamic load balancing can be applied for parallel simulations with adaptive mesh refinement. This will be very beneficial to PF simulations involving complex geometries, such as micro-structured substrate and heterogeneous sponge structure.

Appendix A. Workflow of Running a *phaseFieldFoam* Test Case

The workflow on how to run a test case with *phaseFieldFoam* will be demonstrated with the example test case in the folder *dropletSpreading*. The hierarchy of the files contained in this test case folder is shown in Figure A.1.

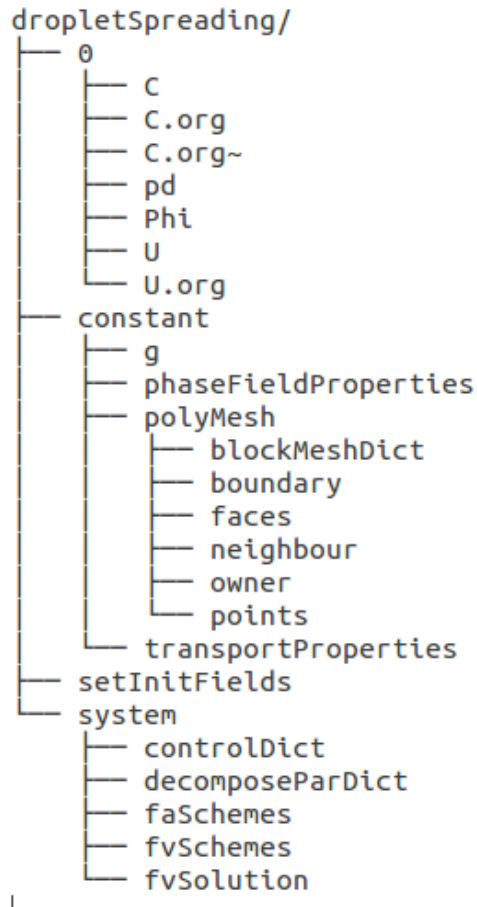


Figure A.1: The hierarchy of the files within the test case folder *dropletSpreading*.

In this test case, one carries out the simulation of a liquid droplet spreading from its initial shape towards the equilibrium state. Please note that this workflow is written for readers who have basic knowledge of OpenFOAM® and preferably working experience with *interFoam*. Thus, *phaseFieldFoam*-specific rather than OpenFOAM®-general guides

are provided here. For the latter, one is referred to the OpenFOAM® user guide (<http://cfd.direct/openfoam/user-guide/>) and in particular the dam break test-case tutorial using *interFoam* (<http://cfd.direct/openfoam/user-guide/damBreak/#x7-500002.3>).

- **Mesh Generation**

Generate the wedge mesh for 2D-axisymmetric simulation using the command *blockMesh*. Further information on using *blockMesh* for mesh generation can be found in the OpenFOAM® user guide (<http://cfd.direct/openfoam/user-guide/blockmesh/>) and special tips on wedge mesh generation therein.

- **Boundary Condition Setup**

The boundary conditions for order parameter, pressure and velocity can be found in the file *C.org*, *pd* and *U* in the folder *0*. Of special importance is wetting boundary condition setting: the equilibrium contact angle $\theta_e = 60^\circ$ for the present test-case is specified in the file *0/C.org* (see the excerpt of the file shown in Figure A.2). There boundary type *constantPhaseContactAngle* is used and *theta0* denotes the equilibrium contact angle.

```
36     bottom
37     {
38         type            constantPhaseContactAngle;
39         theta0          uniform 60;
40         limit           none;
41         value           uniform 0;
42     }
```

Figure A.2: An excerpt from the file *0/C.org* where one specifies the equilibrium contact angle denoted as *theta_0*.

- **Initial Field Setup**

As the phase indicator, i.e. the order parameter C , needs to be appropriately initialized so that a phase-field simulation can be started from an initial condition with a properly-diffuse interface. A non-uniform initial field for the order parameter should be set appropriately such that:

- 1) $C=1$ for liquid and $C=-1$ for gas
- 2) $C = \tanh(x/\sqrt{2}\varepsilon)$ across the diffuse interface between the two phases

This initialization is made with *funkySetFields*, which is similar to the standard OpenFOAM® utility *setFields* and equipped with greater flexibility for field initialization. More information on *funkySetFields* can be found on <https://openfoamwiki.net/index.php/Contrib/funkySetFields>. The active development of *funkySetFields* is included in *swak4Foam*. Thus, one should first install *swak4foam* (<https://openfoamwiki.net/index.php/Contrib/swak4Foam>) to employ *funkySetFields*.

```
1 #!/bin/bash
2
3 echo "start to set the initial field of Order Parameter with tanh profile over interface"
4 cp 0/C.org 0/C
5 cp 0/U.org 0/U
6 # Specify the droplet center
7 # The example test case here is 2D; we give y- coordinate of the center point:
8 cx=0
9 cz=0
10
11 # the radius of droplet
12 radius=0.5e-3
13
14 # the interface width |
15 epsilon=1e-5
16
17 funkySetFields -time 0 -field C -keepPatches -expression "tanh((-sqrt(sqr(pos().x-$cx)+sqr
    (pos().z-$cz))+radius)/(sqrt(2)*$epsilon))"
18
19 echo the process is finished
```

Figure A.3: The script file *setInitFields* where one initializes the order parameter field.

To exemplify the use of *funkySetFields* for the order parameter initialization, a script *setInitFields* is prepared. Its content is shown in Figure A.3. The profile of C across the diffuse interface is set according to the hyperbolic function by *funkySetFields* with corresponding options at line #17. To run this script, one needs to enter “./setInitFields” in the terminal.

- **Physical Parameter Setup**

The density, viscosity and surface tension coefficient of the gas-liquid two-phase flow system is set by the file *constant/transportProperties* (see Figure A.4) Therein *rhoa* and *rhob* denote the density of gas and liquid phase, *nua* and *nub* the kinematic viscosity of the respective phase. In line #24, *sigma* indicates the interfacial tension coefficient. Like *interFoam* testcases, gravitational acceleration is set in the file *constant/g*.

```

17
18 //- fluid properties
19 //- a: air; b: water
20 rhoa      rhoa [1 -3 0 0 0 0 0] 1;
21 rhob      rhob [1 -3 0 0 0 0 0] 910;
22 nua       nua [0 2 -1 0 0 0 0] 1.81e-05;
23 nub       nub [0 2 -1 0 0 0 0] 3.297e-05;
24 sigma     sigma [ 1 0 -2 0 0 0 0 ] 0.0294;
25

```

Figure A.4: The file *constant/transportProperties* where one specifies physical properties of the two phases.

- **Phase-Field Specific Parameter Setup**

One needs to set two phase-field specific parameters, namely, the capillary width parameter ε and the Cahn-Hilliard mobility parameter κ . One can achieve it by the file *constant/phaseFieldProperties* (see line #28 and #31 in Figure A.5).

References

- [1] D. Bonn, J. Eggers, J. Indekeu, J. Meunier, E. Rolley, Wetting and spreading, *Reviews of Modern Physics* 81 (2009) 739-805.
- [2] Trainmountain, Frankfurt To London High-Speed Rail Link Put On Hold, <http://www.trainmountain.co.uk/2014/02/19/frankfurt-london-high-speed-rail-link-put-hold/>, 2014 (accessed on 15.07.2016).
- [3] A. Meyerson, Rain drops cling valiantly to the train window in an effort to avoid an East River fate (at Spuyten Duyvil), <http://andrewmeyerson.com/post/104692661787/rain-drops-cling-valiantly-to-the-train-window-in>, 2014 (accessed on 01.07.2016).
- [4] D.Y. Xia, L.M. Johnson, G.P. Lopez, Anisotropic Wetting Surfaces with One-Dimensional and Directional Structures: Fabrication Approaches, Wetting Properties and Potential Applications, *Advanced Materials* 24 (2012) 1287-1302.
- [5] M.J. Jebrail, A.H.C. Ng, V. Rai, R. Hili, A.K. Yudin, A.R. Wheeler, Synchronized Synthesis of Peptide-Based Macrocycles by Digital Microfluidics, *Angewandte Chemie-International Edition* 49 (2010) 8625-8629.
- [6] K. Pangarkar, T.J. Schildhauer, J.R. van Ommen, J. Nijenhuis, F. Kapteijn, J.A. Moulijn, Structured packings for multiphase catalytic reactors, *Industrial & Engineering Chemistry Research* 47 (2008) 3720-3751.
- [7] E. Tronconi, G. Groppi, T. Boger, A. Heibel, Monolithic catalysts with 'high conductivity' honeycomb supports for gas/solid exothermic reactions: characterization of the heat-transfer properties, *Chemical Engineering Science* 59 (2004) 4941-4949.
- [8] M. Klumpp, A. Inayat, J. Schwerdtfeger, C. Korner, R.F. Singer, H. Freund, W. Schwieger, Periodic open cellular structures with ideal cubic cell geometry: Effect of porosity and cell orientation on pressure drop behavior, *Chemical Engineering Journal* 242 (2014) 364-378.
- [9] E. Bianchi, W. Schwieger, H. Freund, Assessment of Periodic Open Cellular Structures for Enhanced Heat Conduction in Catalytic Fixed-Bed Reactors, *Advanced Engineering Materials* 18 (2016) 608-614.
- [10] C.P. Stemmet, J. van der Schaaf, B.F.M. Kuster, J.C. Schouten, Solid foam packings for multiphase reactors - Modelling of liquid holdup and mass transfer, *Chemical Engineering Research & Design* 84 (2006) 1134-1141.
- [11] C.P. Stemmet, F. Bartelds, J. van der Schaaf, B.F.M. Kuster, J.C. Schouten, Influence of liquid viscosity and surface tension on the gas-liquid mass transfer coefficient for solid foam packings in co-current two-phase flow, *Chemical Engineering Research & Design* 86 (2008) 1094-1106.
- [12] J. Zalucky, F. Moller, M. Schubert, U. Hampel, Flow Regime Transition in Open-Cell Solid Foam Packed Reactors: Adaption of the Relative Permeability Concept and Experimental Validation, *Industrial & Engineering Chemistry Research* 54 (2015) 9708-9721.
- [13] M. Wallenstein, N. Hafen, H. Heinzmann, S. Schug, W. Arlt, M. Kind, B. Dietrich, Qualitative and quantitative insights into multiphase flow in ceramic sponges using X-ray computed tomography, *Chemical Engineering Science* 138 (2015) 118-127.
- [14] D. Pugliesi, Trickle-bed reactor, https://en.wikipedia.org/wiki/Trickle-bed_reactor, 2014.

- [15] B. Dietrich, S. Meinicke, X. Cai, M. Wörner, Structured chemical reactors: experimental analysis and simulation, *ACHEMA 2015*, Frankfurt, Germany, 2015.
- [16] J.H. Snoeijer, B. Andreotti, Moving Contact Lines: Scales, Regimes, and Dynamical Transitions, *Annual Review of Fluid Mechanics*, Vol 45 45 (2013) 269-292.
- [17] T. Young, An Essay on the Cohesion of Fluids, *Phil. Trans. R. Soc. Lond.* 95 (1805) 65-87.
- [18] C. Huh, L.E. Scriven, Hydrodynamic Model of Steady Movement of a Solid/Liquid/Fluid Contact Line, *Journal of Colloid and Interface Science* 35 (1971) 85-101.
- [19] L. Bocquet, E. Charlaix, Nanofluidics, from bulk to interfaces, *Chemical Society Reviews* 39 (2010) 1073-1095.
- [20] R.L. Hoffman, Study of Advancing Interface .1. Interface Shape in Liquid-Gas Systems, *Journal of Colloid and Interface Science* 50 (1975) 228-241.
- [21] O.V. Voinov, Hydrodynamics of wetting, *Fluid Dynamics* 11 (1976) 714-721.
- [22] L.H. Tanner, Spreading of Silicone Oil Drops on Horizontal Surfaces, *Journal of Physics D-Applied Physics* 12 (1979) 1473-1484.
- [23] R.G. Cox, The Dynamics of the Spreading of Liquids on a Solid-Surface .2. Surfactants, *Journal of Fluid Mechanics* 168 (1986) 195-220.
- [24] C.L. Navier, Mémoire sur les lois du mouvement des fluides, *Mem. Acad. Sci. Inst. Fr.* 6 (1823) 389-440.
- [25] E.B. Dussan, Spreading of Liquids on Solid-Surfaces - Static and Dynamic Contact Lines, *Annual Review of Fluid Mechanics* 11 (1979) 371-400.
- [26] T.D. Blake, The physics of moving wetting lines, *Journal of Colloid and Interface Science* 299 (2006) 1-13.
- [27] M. Fermigier, P. Jenffer, An Experimental Investigation of the Dynamic Contact-Angle in Liquid Liquid-Systems, *Journal of Colloid and Interface Science* 146 (1991) 226-241.
- [28] X.D. Wang, X.F. Peng, Y.Y. Duan, B.X. Wang, Dynamics of spreading of liquid on solid surface, *Chinese Journal of Chemical Engineering* 15 (2007) 730-737.
- [29] J.C. Berg, *Wettability*, Marcel Dekker, New York, 1993.
- [30] M. Renardy, Y. Renardy, J. Li, Numerical simulation of moving contact line problems using a volume-of-fluid method, *Journal of Computational Physics* 171 (2001) 243-263.
- [31] S. Afkhami, S. Zaleski, M. Bussmann, A mesh-dependent model for applying dynamic contact angles to VOF simulations, *Journal of Computational Physics* 228 (2009) 5370-5389.
- [32] C. Schonecker, T. Baier, S. Hardt, Influence of the enclosed fluid on the flow over a microstructured surface in the Cassie state, *Journal of Fluid Mechanics* 740 (2014) 168-195.
- [33] T.Z. Qian, X.P. Wang, P. Sheng, Power-law slip profile of the moving contact line in two-phase immiscible flows, *Physical Review Letters* 93 (2004).
- [34] T.D. Blake, J.M. Haynes, Kinetics of Liquid/Liquid Displacement, *Journal of Colloid and Interface Science* 30 (1969) 421-423.

- [35] T.D. Blake, J. De Coninck, Dynamics of wetting and Kramers' theory, *European Physical Journal-Special Topics* 197 (2011) 249-264.
- [36] D. Seveno, T.D. Blake, S. Goossens, J. De Coninck, Predicting the Wetting Dynamics of a Two-Liquid System, *Langmuir* 27 (2011) 14958-14967.
- [37] C.W. Hirt, B.D. Nichols, Volume of Fluid (Vof) Method for the Dynamics of Free Boundaries, *Journal of Computational Physics* 39 (1981) 201-225.
- [38] M. Wörner, Numerical modeling of multiphase flows in microfluidics and micro process engineering: a review of methods and applications, *Microfluidics and Nanofluidics* 12 (2012) 841-886.
- [39] M. Rudman, Volume-tracking methods for interfacial flow calculations, *International Journal for Numerical Methods in Fluids* 24 (1997) 671-691.
- [40] W.J. Rider, D.B. Kothe, Reconstructing volume tracking, *Journal of Computational Physics* 141 (1998) 112-152.
- [41] A. Fath, D. Bothe, Direct numerical simulations of thermocapillary migration of a droplet attached to a solid wall, *International Journal of Multiphase Flow* 77 (2015) 209-221.
- [42] M. Rieber, Numerische Modellierung der Dynamik freier Grenzflächen in Zweiphasenströmungen, Universität Stuttgart, 2004.
- [43] K. Eisenschmidt, M. Ertl, H. Goma, C. Kieffer-Roth, C. Meister, P. Rauschenberger, M. Reitzle, K. Schlottke, B. Weigand, Direct numerical simulations for multiphase flows: An overview of the multiphase code FS3D, *Applied Mathematics and Computation* 272 (2016) 508-517.
- [44] C. Fang, C. Hidrovo, F.M. Wang, J. Eaton, K.E. Goodson, 3-D numerical simulation of contact angle hysteresis for microscale two phase flow, *International Journal of Multiphase Flow* 34 (2008) 690-705.
- [45] H. Alla, S. Freifer, T. Roques-Carmes, A computational fluid dynamics model using the volume of fluid method for describing the dynamics of spreading of Newtonian fluids, *Colloids and Surfaces a-Physicochemical and Engineering Aspects* 386 (2011) 107-115.
- [46] I. Malgarinos, N. Nikolopoulos, M. Marengo, C. Antonini, M. Gavaises, VOF simulations of the contact angle dynamics during the drop spreading: Standard models and a new wetting force model, *Advances in Colloid and Interface Science* 212 (2014) 1-20.
- [47] J.B. Dupont, D. Legendre, Numerical simulation of static and sliding drop with contact angle hysteresis, *Journal of Computational Physics* 229 (2010) 2453-2478.
- [48] D. Legendre, M. Maglio, Numerical simulation of spreading drops, *Colloids and Surfaces a-Physicochemical and Engineering Aspects* 432 (2013) 29-37.
- [49] A.A. Saha, S.K. Mitra, Effect of dynamic contact angle in a volume of fluid (VOF) model for a microfluidic capillary flow, *Journal of Colloid and Interface Science* 339 (2009) 461-480.
- [50] N. Linder, A. Criscione, I.V. Roisman, H. Marschall, C. Tropea, 3D computation of an incipient motion of a sessile drop on a rigid surface with contact angle hysteresis, *Theoretical and Computational Fluid Dynamics* 29 (2015) 373-390.
- [51] H.G. Weller, A new approach to VOF-based interface capturing methods for incompressible and compressible flow, Tech. Rep. TR/HGW/07, OpenCFD Ltd, 2006.

- [52] S. Osher, J.A. Sethian, Fronts Propagating with Curvature-Dependent Speed - Algorithms Based on Hamilton-Jacobi Formulations, *Journal of Computational Physics* 79 (1988) 12-49.
- [53] M. Sussman, A.S. Almgren, J.B. Bell, P. Colella, L.H. Howell, M.L. Welcome, An adaptive level set approach for incompressible two-phase flows, *Journal of Computational Physics* 148 (1999) 81-124.
- [54] P.D.M. Spelt, A level-set approach for simulations of flows with multiple moving contact lines with hysteresis, *Journal of Computational Physics* 207 (2005) 389-404.
- [55] H. Ding, P.D.M. Spelt, Inertial effects in droplet spreading: a comparison between diffuse-interface and level-set simulations, *Journal of Fluid Mechanics* 576 (2007) 287-296.
- [56] Y. Sui, P.D.M. Spelt, Validation and modification of asymptotic analysis of slow and rapid droplet spreading by numerical simulation, *Journal of Fluid Mechanics* 715 (2013) 283-313.
- [57] Y. Sui, P.D.M. Spelt, An efficient computational model for macroscale simulations of moving contact lines, *Journal of Computational Physics* 242 (2013) 37-52.
- [58] Y.M. Chen, R. Mertz, R. Kulenovic, Numerical simulation of bubble formation on orifice plates with a moving contact line, *International Journal of Multiphase Flow* 35 (2009) 66-77.
- [59] J.K. Park, K.H. Kang, Numerical analysis of moving contact line with contact angle hysteresis using feedback deceleration technique, *Physics of Fluids* 24 (2012).
- [60] H. Liu, S. Krishnan, S. Marella, H.S. Udaykumar, Sharp interface Cartesian grid method II: A technique for simulating droplet interactions with surfaces of arbitrary shape, *Journal of Computational Physics* 210 (2005) 32-54.
- [61] S. Zahedi, K. Gustavsson, G. Kreiss, A conservative level set method for contact line dynamics, *Journal of Computational Physics* 228 (2009) 6361-6375.
- [62] D. Lakehal, C. Narayanan, D. Caviezel, J. von Rickenbach, S. Reboux, Progress in computational microfluidics using TransAT, *Microfluidics and Nanofluidics* 15 (2013) 415-429.
- [63] S.O. Unverdi, G. Tryggvason, A Front-Tracking Method for Viscous, Incompressible, Multi-Fluid Flows, *Journal of Computational Physics* 100 (1992) 25-37.
- [64] S. Manservigi, R. Scardovelli, A variational approach to the contact angle dynamics of spreading droplets, *Computers & Fluids* 38 (2009) 406-424.
- [65] M. Muradoglu, S. Tasoglu, A front-tracking method for computational modeling of impact and spreading of viscous droplets on solid walls, *Computers & Fluids* 39 (2010) 615-625.
- [66] D. Jacqmin, Calculation of two-phase Navier-Stokes flows using phase-field modeling, *Journal of Computational Physics* 155 (1999) 96-127.
- [67] J.D. van der Waals, The thermodynamic theory of capillarity under the hypothesis of a continuous variation of density (in Dutch), *Verhandel/Konink Akad Wetten* 1 (1879) 8.
- [68] J.W. Cahn, Phase Separation by Spinodal Decomposition in Isotropic Systems, *Journal of Chemical Physics* 42 (1965) 93-99.

- [69] D.M. Anderson, G.B. McFadden, A.A. Wheeler, Diffuse-interface methods in fluid mechanics, *Annual Review of Fluid Mechanics* 30 (1998) 139-165.
- [70] J.J. Feng, C. Liu, J. Shen, P.T. Yue, An energetic variational formulation with phase field methods for interfacial dynamics of complex fluids: advantages and challenges, in: M.-C.T. Calderer, E. Terentjev, (Eds.), *Modeling of Soft Matter*, Springer, New York, 2005, pp. 1-26.
- [71] P. Yue, J.J. Feng, Can diffuse-interface models quantitatively describe moving contact lines?, *European Physical Journal-Special Topics* 197 (2011) 37-46.
- [72] D. Jacqmin, Contact-line dynamics of a diffuse fluid interface, *Journal of Fluid Mechanics* 402 (2000) 57-88.
- [73] J. Lowengrub, L. Truskinovsky, Quasi-incompressible Cahn-Hilliard fluids and topological transitions, *Proceedings of the Royal Society a-Mathematical Physical and Engineering Sciences* 454 (1998) 2617-2654.
- [74] P.T. Yue, J.J. Feng, C. Liu, J. Shen, A diffuse-interface method for simulating two-phase flows of complex fluids, *Journal of Fluid Mechanics* 515 (2004) 293-317.
- [75] C.F. Zhou, P.T. Yue, J.J. Feng, Formation of simple and compound drops in microfluidic devices, *Physics of Fluids* 18 (2006).
- [76] M. Ahmadlouydarab, J.J. Feng, Motion and coalescence of sessile drops driven by substrate wetting gradient and external flow, *Journal of Fluid Mechanics* 746 (2014) 214-235.
- [77] E. Olsson, G. Kreiss, A conservative level set method for two phase flow, *Journal of Computational Physics* 210 (2005) 225-246.
- [78] P.T. Yue, J.J. Feng, Phase-field simulations of dynamic wetting of viscoelastic fluids, *Journal of Non-Newtonian Fluid Mechanics* 189 (2012) 8-13.
- [79] Y.L. Wang, D.Q. Minh, G. Amberg, Dynamic wetting of viscoelastic droplets, *Physical Review E* 92 (2015).
- [80] T.Z. Qian, X.P. Wang, P. Sheng, A variational approach to moving contact line hydrodynamics, *Journal of Fluid Mechanics* 564 (2006) 333-360.
- [81] S. Guo, M. Gao, X.M. Xiong, Y.J. Wang, X.P. Wang, P. Sheng, P. Tong, Direct Measurement of Friction of a Fluctuating Contact Line, *Physical Review Letters* 111 (2013).
- [82] T.Z. Qian, X.P. Wang, P. Sheng, Molecular scale contact line hydrodynamics of immiscible flows, *Physical Review E* 68 (2003).
- [83] X.P. Wang, T.Z. Qian, P. Sheng, Moving contact line on chemically patterned surfaces, *Journal of Fluid Mechanics* 605 (2008) 59-78.
- [84] Y. Shi, X.P. Wang, Modeling and simulation of dynamics of three-component flows on solid surface, *Japan Journal of Industrial and Applied Mathematics* 31 (2014) 611-631.
- [85] Q. Zhang, T.Z. Qian, X.P. Wang, Phase field simulation of a droplet impacting a solid surface, *Physics of Fluids* 28 (2016).
- [86] W. Villanueva, G. Amberg, Some generic capillary-driven flows, *International Journal of Multiphase Flow* 32 (2006) 1072-1086.
- [87] A. Carlson, M. Do-Quang, G. Amberg, Modeling of dynamic wetting far from equilibrium, *Physics of Fluids* 21 (2009).

- [88] A. Carlson, M. Do-Quang, G. Amberg, Dissipation in rapid dynamic wetting, *Journal of Fluid Mechanics* 682 (2011) 213-240.
- [89] A. Carlson, G. Bellani, G. Amberg, Contact line dissipation in short-time dynamic wetting, *Epl* 97 (2012).
- [90] A. Carlson, G. Bellani, G. Amberg, Universality in dynamic wetting dominated by contact-line friction, *Physical Review E* 85 (2012).
- [91] V.V. Khatavkar, P.D. Anderson, P.C. Duineveld, H.E.H. Meijer, Diffuse-interface modelling of droplet impact, *Journal of Fluid Mechanics* 581 (2007) 97-127.
- [92] V.V. Khatavkar, P.D. Anderson, H.E.H. Meijer, Capillary spreading of a droplet in the partially wetting regime using a diffuse-interface model, *Journal of Fluid Mechanics* 572 (2007) 367-387.
- [93] V.V. Khatavkar, P.D. Anderson, H.E.H. Meijer, On scaling of diffuse-interface models, *Chemical Engineering Science* 61 (2006) 2364-2378.
- [94] P.T. Yue, C.F. Zhou, J.J. Feng, Sharp-interface limit of the Cahn-Hilliard model for moving contact lines, *Journal of Fluid Mechanics* 645 (2010) 279-294.
- [95] P.T. Yue, J.J. Feng, C. Liu, J. Shen, Diffuse-interface simulations of drop coalescence and retraction in viscoelastic fluids, *Journal of Non-Newtonian Fluid Mechanics* 129 (2005) 163-176.
- [96] P. Yue, C. Zhou, J.J. Feng, C.F. Ollivier-Gooch, H.H. Hu, Phase-field simulations of interfacial dynamics in viscoelastic fluids using finite elements with adaptive meshing, *Journal of Computational Physics* 219 (2006) 47-67.
- [97] P.T. Yue, C.F. Zhou, J.J. Feng, Spontaneous shrinkage of drops and mass conservation in phase-field simulations, *Journal of Computational Physics* 223 (2007) 1-9.
- [98] C.F. Zhou, P.T. Yue, J.J. Feng, C.F. Ollivier-Gooch, H.H. Hu, 3D phase-field simulations of interfacial dynamics in Newtonian and viscoelastic fluids, *Journal of Computational Physics* 229 (2010) 498-511.
- [99] P.T. Yue, J.J. Feng, Wall energy relaxation in the Cahn-Hilliard model for moving contact lines, *Physics of Fluids* 23 (2011).
- [100] H. Ding, P.D.M. Spelt, Wetting condition in diffuse interface simulations of contact line motion, *Physical Review E* 75 (2007).
- [101] H. Ding, P.D.M. Spelt, Onset of motion of a three-dimensional droplet on a wall in shear flow at moderate Reynolds numbers, *Journal of Fluid Mechanics* 599 (2008) 341-362.
- [102] H. Ding, E.Q. Li, F.H. Zhang, Y. Sui, P.D.M. Spelt, S.T. Thoroddsen, Propagation of capillary waves and ejection of small droplets in rapid droplet spreading, *Journal of Fluid Mechanics* 697 (2012) 92-114.
- [103] H. Ding, T.G. Theofanous, The inertial regime of drop impact on an anisotropic porous substrate, *Journal of Fluid Mechanics* 691 (2012) 546-567.
- [104] H. Ding, P.D.M. Spelt, C. Shu, Diffuse interface model for incompressible two-phase flows with large density ratios, *Journal of Computational Physics* 226 (2007) 2078-2095.
- [105] C.Y. Zhang, H. Ding, P. Gao, Y.L. Wu, Diffuse interface simulation of ternary fluids in contact with solid, *Journal of Computational Physics* 309 (2016) 37-51.

- [106] H. Garcke, B. Nestler, B. Stoth, A multiphase field concept: Numerical simulations of moving phase boundaries and multiple junctions, *Siam Journal on Applied Mathematics* 60 (1999) 295-315.
- [107] H. Garcke, B. Nestler, B. Stinner, F. Wendler, Allen-Cahn systems with volume constraints, *Mathematical Models & Methods in Applied Sciences* 18 (2008) 1347-1381.
- [108] B. Nestler, F. Wendler, M. Selzer, B. Stinner, H. Garcke, Phase-field model for multiphase systems with preserved volume fractions, *Physical Review E* 78 (2008).
- [109] X.F. Yang, J.J. Feng, C. Liu, J. Shen, Numerical simulations of jet pinching-off and drop formation using an energetic variational phase-field method, *Journal of Computational Physics* 218 (2006) 417-428.
- [110] M. Ben Said, M. Selzer, B. Nestler, D. Braun, C. Greiner, H. Garcke, A Phase-Field Approach for Wetting Phenomena of Multiphase Droplets on Solid Surfaces, *Langmuir* 30 (2014) 4033-4039.
- [111] F. Weyer, M. Ben Said, J. Hotzer, M. Berghoff, L. Dreesen, B. Nestler, N. Vandewalle, Compound Droplets on Fibers, *Langmuir* 31 (2015) 7799-7805.
- [112] A. Badillo, Quantitative phase-field modeling for wetting phenomena, *Physical Review E* 91 (2015).
- [113] S. Succi, *The Lattice Boltzmann equation for fluid dynamics and beyond*, Clarendon, Oxford, 2001.
- [114] X.W. Shan, H.D. Chen, Lattice Boltzmann Model for Simulating Flows with Multiple Phases and Components, *Physical Review E* 47 (1993) 1815-1819.
- [115] M.R. Swift, E. Orlandini, W.R. Osborn, J.M. Yeomans, Lattice Boltzmann simulations of liquid-gas and binary fluid systems, *Physical Review E* 54 (1996) 5041-5052.
- [116] H.Y. Chen, D. Jasnow, J. Vinals, Interface and contact line motion in a two phase fluid under shear flow, *Physical Review Letters* 85 (2000) 1686-1689.
- [117] A.J. Briant, P. Papatzacos, J.M. Yeomans, Lattice Boltzmann simulations of contact line motion in a liquid-gas system, *Philosophical Transactions of the Royal Society of London Series a-Mathematical Physical and Engineering Sciences* 360 (2002) 485-495.
- [118] A.J. Briant, A.J. Wagner, J.M. Yeomans, Lattice Boltzmann simulations of contact line motion. I. Liquid-gas systems, *Physical Review E* 69 (2004).
- [119] A.J. Briant, J.M. Yeomans, Lattice Boltzmann simulations of contact line motion. II. Binary fluids, *Physical Review E* 69 (2004).
- [120] C.M. Pooley, H. Kusumaatmaja, J.M. Yeomans, Contact line dynamics in binary lattice Boltzmann simulations, *Physical Review E* 78 (2008).
- [121] O. Kuksenok, D. Jasnow, J. Yeomans, A.C. Balazs, Periodic droplet formation in chemically patterned microchannels, *Physical Review Letters* 91 (2003).
- [122] J. Leopoldes, A. Dupuis, D.G. Bucknall, J.M. Yeomans, Jetting micron-scale droplets onto chemically heterogeneous surfaces, *Langmuir* 19 (2003) 9818-9822.
- [123] A. Dupuis, J.M. Yeomans, Lattice Boltzmann modelling of droplets on chemically heterogeneous surfaces, *Future Generation Computer Systems* 20 (2004) 993-1001.

- [124] A. Dupuis, J. Leopoldes, D.G. Bucknall, J.M. Yeomans, Control of drop positioning using chemical patterning, *Applied Physics Letters* 87 (2005).
- [125] H. Kusumaatmaja, J. Leopoldes, A. Dupuis, J.M. Yeomans, Drop dynamics on chemically patterned surfaces, *Europhysics Letters* 73 (2006) 740-746.
- [126] H. Kusumaatmaja, J.M. Yeomans, Modeling contact angle hysteresis on chemically patterned and superhydrophobic surfaces, *Langmuir* 23 (2007) 6019-6032.
- [127] H. Kusumaatmaja, J.M. Yeomans, Controlling drop size and polydispersity using chemically patterned surfaces, *Langmuir* 23 (2007) 956-959.
- [128] A. Dupuis, J.M. Yeomans, Modeling droplets on superhydrophobic surfaces: Equilibrium states and transitions, *Langmuir* 21 (2005) 2624-2629.
- [129] A. Dupuis, J.M. Yeomans, Droplet dynamics on patterned substrates, *Pramana-Journal of Physics* 64 (2005) 1019-1027.
- [130] B.M. Mognetti, H. Kusumaatmaja, J.M. Yeomans, Drop dynamics on hydrophobic and superhydrophobic surfaces, *Faraday Discussions* 146 (2010) 153-165.
- [131] B.M. Mognetti, J.M. Yeomans, Modeling Receding Contact Lines on Superhydrophobic Surfaces, *Langmuir* 26 (2010) 18162-18168.
- [132] M.L. Blow, J.M. Yeomans, Anisotropic imbibition on surfaces patterned with polygonal posts, *Philosophical Transactions of the Royal Society a-Mathematical Physical and Engineering Sciences* 369 (2011) 2519-2527.
- [133] H. Kusumaatmaja, R.J. Vrancken, C.W.M. Bastiaansen, J.M. Yeomans, Anisotropic drop morphologies on corrugated surfaces, *Langmuir* 24 (2008) 7299-7308.
- [134] A. Dupuis, J.M. Yeomans, Droplets on patterned substrates: Water off a beetle's back, *International Journal for Numerical Methods in Fluids* 50 (2006) 255-261.
- [135] H. Marschall, X. Cai, M. Worner, O. Deutschmann, Conservative finite volume discretization of the two-phase Navier-Stokes Cahn-Hilliard and Allen-Cahn equations on general grids with applications to dynamic wetting, (2016) in preparation.
- [136] H. Marschall, X. Cai, M. Worner, O. Deutschmann, Development of Phase Field Methods using OpenFOAM® - Part I: Method Development and Implementation, 10th International OpenFOAM® Workshop, Ann Arbor, Michigan, USA, 2015.
- [137] X. Cai, H. Marschall, M. Wörner, O. Deutschmann, Numerical Simulation of Wetting Phenomena with a Phase-Field Method Using OpenFOAM®, *Chemical Engineering & Technology* 38 (2015) 1985-1992.
- [138] X. Cai, M. Wörner, H. Marschall, O. Deutschmann, Numerical study on the wettability dependent interaction of a rising bubble with a periodic open cell structure, *Catalysis Today* 273 (2016) 151-160.
- [139] M. Wörner, X. Cai, H. Alla, P. Yue, A semi-analytical method to estimate the slip length of spreading spherical-cap droplets using Cox theory, *Theoretical and Computational Fluid Dynamics* (2016) submitted.
- [140] X. Cai, M. Wörner, O. Deutschmann, Interface-resolving simulations of gas-liquid flows in a solid sponge structure, 9th International Conference on Multiphase Flow (ICMF 2016), Florence, Italy, 2016.

- [141] X. Cai, H. Marschall, M. Wörner, O. Deutschmann, A phase field method with adaptive mesh refinement for numerical simulation of 3D wetting processes with OpenFOAM®, 2nd International Symposium on Multiscale Multiphase Process Engineering (MMPE), Hamburg, Germany, 2014.
- [142] X. Cai, M. Wörner, O. Deutschmann, Implementation of a Phase Field Method in OpenFOAM® for Simulation of Spreading Droplets and Verification by Test Problems, 7th Open Source CFD International Conference, Hamburg, Germany, 2013.
- [143] U. Hampel, R. Dittmeyer, A. Patyk, T. Wetzel, R. Lange, H. Freund, W. Schwieger, M. Grunewald, M. Schluter, U. Petasch, The Helmholtz Energy Alliance "Energy Efficient Multiphase Chemical Processes", Chemie Ingenieur Technik 85 (2013) 992-996.
- [144] J.W. Cahn, J.E. Hilliard, Free Energy of a Nonuniform System I. Interfacial Free Energy, Journal of Chemical Physics 28 (1958) 258-267.
- [145] A.J. Bray, Theory of Phase-Ordering Kinetics, Advances in Physics 43 (1994) 357-459.
- [146] J.W. Cahn, J.E. Hilliard, Free Energy of a Nonuniform System III. Nucleation in a 2-Component Incompressible Fluid, Journal of Chemical Physics 31 (1959) 688-699.
- [147] J. Kim, A continuous surface tension force formulation for diffuse-interface models, Journal of Computational Physics 204 (2005) 784-804.
- [148] Q.W. He, N. Kasagi, Phase-Field simulation of small capillary-number two-phase flow in a microtube, Fluid Dynamics Research 40 (2008) 497-509.
- [149] P.C. Hohenberg, B.I. Halperin, Theory of Dynamic Critical Phenomena, Reviews of Modern Physics 49 (1977) 435-479.
- [150] A.J. Bray, Theory of phase-ordering kinetics, Advances in Physics 51 (2002) 481-587.
- [151] A. Karma, Phase-field formulation for quantitative modeling of alloy solidification, Physical Review Letters 87 (2001).
- [152] B. Nestler, H. Garcke, B. Stinner, Multicomponent alloy solidification: Phase-field modeling and simulations, Physical Review E 71 (2005).
- [153] H.G. Weller, G. Tabor, H. Jasak, C. Fureby, A tensorial approach to computational continuum mechanics using object-oriented techniques, Computers in Physics 12 (1998) 620-631.
- [154] H. Jasak, A. Jemcov, Z. Tukovic, OpenFOAM: A C++ Library for Complex Physics Simulations, International Workshop on Coupled Methods in Numerical Dynamics IUC, Dubrovnik, Croatia, 2007.
- [155] C. Greenshields, OpenFOAM User Guide, <http://foam.sourceforge.net/docs/Guides-a4/UserGuide.pdf>, CFD Direct Ltd., 2015.
- [156] C. Greenshields, OpenFOAM Programmer's Guide, <http://foam.sourceforge.net/docs/Guides-a4/ProgrammersGuide.pdf>, CFD Direct Ltd., 2015.
- [157] H. Jasak, Error Analysis and Estimation for the Finite Volume Method with Applications to Fluid Flows, Department of Mechanical Engineering, Imperial College of Science, Technology and Medicine, London, 1996.

- [158] O. Ubbink, Numerical prediction of two fluid systems with sharp interfaces, Department of Mechanical Engineering, Imperial College of Science, Technology and Medicine, London, 1997.
- [159] H. Rusche, Computational Fluid Dynamics of Dispersed Two-Phase Flows at High Phase Fractions, Department of Mechanical Engineering, Imperial College of Science, Technology and Medicine, London, 2002.
- [160] H. Marschall, Towards the Numerical Simulation of Multi-Scale Two-Phase Flows, Fakultät für Chemie, Technische Universität München, München, 2011.
- [161] H. Jasak, H. Nilsson, H. Rusche, M. Beaudoin, B. Gschaider, RELEASE NOTES FOR FOAM-EXTEND-3.2, <https://sourceforge.net/p/foam-extend/foam-extend-3.2/ci/master/tree/ReleaseNotes.txt>, The foam-extend project, Ann Arbor, 2015.
- [162] S. Dong, On imposing dynamic contact-angle boundary conditions for wall-bounded liquid-gas flows, *Computer Methods in Applied Mechanics and Engineering* 247 (2012) 179-200.
- [163] H. Abels, H. Garcke, G. Grun, Thermodynamically Consistent, Frame Indifferent Diffuse Interface Models for Incompressible Two-Phase Flows with Different Densities, *Mathematical Models & Methods in Applied Sciences* 22 (2012).
- [164] E. Berberovic, N.P. van Hinsberg, S. Jakirlic, I.V. Roisman, C. Tropea, Drop impact onto a liquid layer of finite thickness: Dynamics of the cavity evolution, *Physical Review E* 79 (2009).
- [165] R.I. Issa, Solution of the Implicitly Discretized Fluid-Flow Equations by Operator-Splitting, *Journal of Computational Physics* 62 (1986) 40-65.
- [166] J.U. Brackbill, D.B. Kothe, C. Zemach, A Continuum Method for Modeling Surface-Tension, *Journal of Computational Physics* 100 (1992) 335-354.
- [167] B. Lafaurie, C. Nardone, R. Scardovelli, S. Zaleski, G. Zanetti, Modeling Merging and Fragmentation in Multiphase Flows with Surfer, *Journal of Computational Physics* 113 (1994) 134-147.
- [168] G. Taylor, The formation of emulsions in definable fields of flow, *Proceedings of the Royal Society of London. Series A* 146 (1934) 501-523.
- [169] V.E. Badalassi, H.D. Ceniceros, S. Banerjee, Computation of multiphase systems with phase field models, *Journal of Computational Physics* 190 (2003) 371-397.
- [170] G.K. Batchelor, *An Introduction To Fluid Dynamics*, Cambridge University Press, 1967.
- [171] P.G. de Gennes, F. Brochard-Wyart, D. Quéré, *Capillarity and Wetting Phenomena: Drops, Bubbles, Pearls, Waves*, Springer New York, 2004.
- [172] A. Zosel, Studies of the Wetting Kinetics of Liquid-Drops on Solid-Surfaces, *Colloid and Polymer Science* 271 (1993) 680-687.
- [173] H.P. Jansen, K. Sotthewes, J. van Swigchem, H.J.W. Zandvliet, E.S. Kooij, Lattice Boltzmann modeling of directional wetting: Comparing simulations to experiments, *Physical Review E* 88 (2013) 013008.
- [174] F.J.M. Ruiz-Cabello, H. Kusumaatmaja, M.A. Rodriguez-Valverde, J. Yeomans, M.A. Cabrerizo-Vilchez, Modeling the Corrugation of the Three-Phase Contact Line Perpendicular to a Chemically Striped Substrate, *Langmuir* 25 (2009) 8357-8361.

- [175] C.-O. Möller, M. Schlüter, Experimental study on mass transfer processes and local flow parameters in periodic open cell structures, 10th European Congress of Chemical Engineering (ECCE10), Nice, France, 2015.
- [176] Q.I.E. Segers, Cutting bubbles using wire-mesh structures - direct numerical simulations, Technische Universiteit Eindhoven, Eindhoven, 2015.
- [177] R. Clift, J.R. Grace, M.E. Weber, Bubbles, Drops, and Particles, Academic Press, 1978.
- [178] K. Thiruvalluvan Sujatha, Personal Communication, 2015.
- [179] X.D. Wang, X.F. Peng, B.X. Wang, Contact angle hysteresis and hysteresis tension on rough solid surface, Chinese Journal of Chemical Engineering 12 (2004) 615-621.
- [180] M.V. Twigg, J.T. Richardson, Fundamentals and applications of structured ceramic foam catalysts, Industrial & Engineering Chemistry Research 46 (2007) 4166-4177.
- [181] B. Dietrich, W. Schabel, M. Kind, H. Martin, Pressure drop measurements of ceramic sponges-Determining the hydraulic diameter, Chemical Engineering Science 64 (2009) 3633-3640.
- [182] B. Dietrich, G. Schell, E.C. Bucharsky, R. Oberacker, M.J. Hoffmann, W. Schabel, M. Kind, H. Martin, Determination of the thermal properties of ceramic sponges, International Journal of Heat and Mass Transfer 53 (2010) 198-205.
- [183] I. Mohammed, T. Bauer, M. Schubert, R. Lange, Gas-liquid distribution in tubular reactors with solid foam packings, Chemical Engineering and Processing 88 (2015) 10-18.
- [184] D.W. Green, Perry's Chemical Engineers' Handbook, McGraw-Hill, New York, NY, 2008.
- [185] C. Soulaïne, G. Debenest, M. Quintard, Upscaling multi-component two-phase flow in porous media with partitioning coefficient, Chemical Engineering Science 66 (2011) 6180-6192.
- [186] C. Soulaïne, P. Horgue, J. Franc, M. Quintard, Gas-Liquid Flow Modeling in Columns Equipped with Structured Packing, Aiche Journal 60 (2014) 3665-3674.
- [187] P. Horgue, C. Soulaïne, J. Franc, R. Guibert, G. Debenest, An open-source toolbox for multiphase flow in porous media, Computer Physics Communications 187 (2015) 217-226.
- [188] S. Whitaker, Coupled Transport in Multiphase Systems: A Theory of Drying, Advances in Heat Transfer 31 (1998) 1-102.
- [189] Y.N. Wang, J.W. Chen, F. Larachi, Modelling and simulation of trickle-bed reactors using computational fluid dynamics: A state-of-the-art review, Canadian Journal of Chemical Engineering 91 (2013) 136-180.
- [190] H.A.A. Amiri, A.A. Hamouda, Evaluation of level set and phase field methods in modeling two phase flow with viscosity contrast through dual-permeability porous medium, International Journal of Multiphase Flow 52 (2013) 22-34.
- [191] H.A.A. Amiri, A.A. Hamouda, Pore-scale modeling of non-isothermal two phase flow in 2D porous media: Influences of viscosity, capillarity, wettability and heterogeneity, International Journal of Multiphase Flow 61 (2014) 14-27.

- [192] F. Fichot, P. Meekunnasombat, J. Belloni, F. Duval, A. Garcia, M. Quintard, Two-phase flows in porous media: Prediction of pressure drops using a diffuse interface mathematical description, *Nuclear Engineering and Design* 237 (2007) 1887-1898.
- [193] J.J. Liu, L.J. Lin, R. Song, J.Z. Zhao, A Pore Scale Modelling of Fluid Flow in Porous medium Based on Navier-Stokes Equation, *Disaster Advances* 6 (2013) 129-136.
- [194] X. Liu, Y.F. Zhu, B. Gong, J.P. Yu, S.T. Cui, From molecular dynamics to lattice Boltzmann: a new approach for pore-scale modeling of multi-phase flow, *Petroleum Science* 12 (2015) 282-292.
- [195] Z.Y. Liu, H.Y. Wu, Pore-scale modeling of immiscible two-phase flow in complex porous media, *Applied Thermal Engineering* 93 (2016) 1394-1402.
- [196] S. Meinicke, T. Wetzel, B. Dietrich, CFD modelling of single-phase hydrodynamics and heat transfer in solid sponges, 11th Int. Conf. on CFD in the Minerals and Proc. Industries, Melbourne, 2015.
- [197] S. Ergun, A.A. Orning, Fluid Flow through Randomly Packed Columns and Fluidized Beds, *Industrial and Engineering Chemistry* 41 (1949) 1179-1184.
- [198] B.E. Ghidersa, Finite Volume-based Volume-of-Fluid Method for the Simulation of Two-Phase Flows in Small Rectangular Channels, Fakultät für Maschinenbau, Universität Karlsruhe (TH), Karlsruhe, 2004.
- [199] M.C. Öztasquin, M. Wörner, H.S. Soyhan, Numerical investigation of the stability of bubble train flow in a square minichannel, *Physics of Fluids* 21 (2009).
- [200] J. Große, Über keramische Schwämme als Kolonneneinbauten: Grundlegende Untersuchungen zu Morphologie, Fluidodynamik und Stoffübergang bei der mehrphasigen Durchströmung im Gegenstrom, Karlsruher Instituts für Technologie, Karlsruhe, 2011.

Nomenclature

a	[m]	edge length of a cubic REV sponge structure
A_{eff}	[m ⁻¹]	effective (i.e. specific) interfacial area
A_i	[m ²]	gas-liquid interfacial area
C	[-]	order parameter (also called as phase-field variable)
Cn	[-]	Cahn number
d	[m]	channel width
d_s	[m]	strut diameter
D	[m]	droplet or bubble diameter
D_0	[m]	initial droplet or bubble diameter
D_{cyl}	[m]	diameter of solid cylinder
D_{def}	[-]	deformation parameter of an ellipsoid
$\hat{\mathbf{e}}_x$	[-]	unit vector in x direction
$\hat{\mathbf{e}}_z$	[-]	unit vector in z direction
EO	[-]	Eötvös number
F	[-]	volume fraction
\mathbf{g}	[m s ⁻²]	gravity vector
g	[m s ⁻²]	gravitational acceleration
h	[m]	mesh size
H	[m]	height of computational domain
H_e	[m]	equilibrium height of a droplet
H_{col}	[m]	final height of liquid column in capillary rise
L	[m]	characteristic length scale
L_C	[m]	interface width
L_e	[m]	equilibrium spreading length of a droplet
L_s	[m]	slip length
L_{long}	[m]	length of the long axis of an ellipsoid
L_{short}	[m]	length of the short axis of an ellipsoid
Mo	[-]	Morton number
$\hat{\mathbf{n}}_s$	[-]	unit normal vector to solid surface pointing into fluid

N_C	[-]	number of mesh cells per interface width
N_D	[-]	number of mesh cells per bubble diameter
p	[N m ⁻²]	pressure
Pe_C	[-]	Peclet number in Cahn-Hilliard equation
r	[m]	radial coordinate
R	[m]	droplet or bubble radius
R_0	[m]	initial droplet or bubble radius
Re	[-]	bubble Reynolds number
s	[m]	window size of cubic cell
t	[s]	time
U	[m s ⁻¹]	characteristic velocity scale
U_0	[m s ⁻¹]	superficial velocity in sponge structure
U_{phy}	[m s ⁻¹]	physical velocity in sponge structure
\mathbf{u}	[m s ⁻¹]	velocity field
V	[m ³]	volume of a certain flowing phase in sponge structure
V_{REV}	[m ³]	total volume of a REV
V_{void}	[m ³]	total void volume of a REV
W	[m]	width of computational domain
x	[m]	x -coordinate
y	[m]	y -coordinate
z	[m]	z -coordinate

Greek symbols

β	[-]	liquid saturation
$\dot{\gamma}$	[s ⁻¹]	shear rate
ε	[m]	capillary width
κ	[m ³ s kg ⁻¹]	mobility
λ	[J m ⁻¹]	mixing energy parameter
λ_{μ}	[-]	liquid-to-gas viscosity ratio
μ	[Pa s]	dynamic viscosity
ξ	[N s m ⁻²]	thermodynamics constant
ϕ	[J m ⁻³]	Cahn-Hilliard chemical potential
ψ	[-]	porosity
ρ	[kg m ⁻³]	density
σ	[N m ⁻¹]	interfacial tension coefficient
θ_a	[°]	advancing contact angle
θ_{app}	[°]	apparent contact angle
θ_e	[°]	equilibrium contact angle
θ_m	[°]	microscopic contact angle
θ_r	[°]	receding contact angle
θ_{td}	[°]	thermodynamically-equilibrium contact angle

Subscripts

G	gas phase
L	liquid phase
cl	contact line

List of Abbreviations

AC	Allen-Cahn equation
AMR	Adaptive Mesh Refinement
AKD	Arbeitskreis Deutschmann
BC	Boundary Conditions
CH	Cahn-Hilliard equation
CFD	Computational Fluid Dynamics
CP	Chemical Potential
CSF	Continuum Surface Force
CSS	Continuous Surface Stress
FAU	Friedrich-Alexander-University Erlangen-Nürnberg
FVM	Finite Volume Method
KIT	Karlsruhe Institute of Technology
LBM	Lattice Boltzmann Method
LHS	Left-Hand Side
LS	Level-Set Method
MCL	Moving Contact Line
MD	Molecular Dynamics
NS	Navier-Stokes equations
μ CT	Micro Computed Tomography
PF	Phase-Field
PFM	Phase-Field Method
PFDTs	Perfluorodecyltrichlorosilane
POCS	Periodic Open Cellular Structures
ppi	pores per inch
REV	Representative Elementary Volume
RHS	Right-Hand Side
SiSiC	Silicon Infiltrated Silicon Carbide
STL	Stereolithography
TUHH	Hamburg University of Technology
VOF	Volume-of-Fluid Method

List of Figures

Figure 1.1: Lotus effect of dewdrops on a leaf (from Bonn et al. [1]).	1
Figure 1.2: On a high-speed train (a), we might have an enjoyable watching experience of wetting when observing rain droplets over the window (b). The picture (a) and (b) are adapted respectively from Trainmountain [2] and Meyerson [3].	2
Figure 1.3: A digital microfluidic system (from Jebrail et al. [5]). There each droplet is working as a micro-reactor where parallel reactions can take place with no cross-interference or cross-contamination.	3
Figure 1.4: Inside-views into (a) structure-packed multiphase reactor of successively decreasing length scales: (b) periodic open-cell structure (POCS), (c) sponge (i.e. foam) structure, (d) rising bubble in a representative domain of POCS filled with liquid, (e) gas-liquid interfacial flow in a representative domain of sponge structure, (f) wetting phenomenon involving contact line where three phases meet together. Among the pictures here, (a) is redrawn from Pugliesi [13]; (b) and (c) are from Dietrich et al. [14].	4
Figure 1.5: A liquid-droplet in ambient gas and resting on solid surface, with equilibrium contact angle θ_e . The “point” where the liquid-gas interface meets the solid surface is termed as contact line. It is noted that since here is a 2D lateral view, the black square dot indicating the contact line is not a point but truly a line in 3D reality.	6
Figure 1.6: Macroscopic- (main panel), microscopic- (inset a) and molecular- (inset b) scale involved in moving contact line physics (adapted from Bonn et al. [1]).	7
Figure 3.1: Analytical and simulated order parameter C profile across the diffuse interface with differing mesh resolutions. The Cahn number is $Cn = 0.01$. Adapted from Cai et al. [141].	39
Figure 3.2: Order parameter field (shown as “ordPar”) from the 2D PF simulation with $Cn = 0.01$, $N_C = 4$ and $N_D = 100$. Taken from Cai et al. [141].	39

Figure 3.3: Comparison of the analytical estimate from Yue et al. [96] and present numerical results with respect to the Cahn number Cn versus the shift in order parameter ΔC . Adapted from Cai et al. [141].	40
Figure 3.4: Due to the shear flow, an initially spherical droplet of radius R_0 deforms to an ellipsoid with long axis L_{long} and short axis L_{short} . Adapted from Cai et al. [141].	42
Figure 3.5: Comparison between the computational results for differing Reynolds number Re and Taylor's analytical solution (Eq. (3.8)) with respect to the deformation parameter D_{def} versus the capillary number Ca . Adapted from Cai et al. [141].	43
Figure 3.6: Simulated capillary rise of water into a vertical narrow channel at four instants: (a) 0 ms (initial state), (b) 3 ms, (c) 30 ms, (d) 100 ms (final state). The channel width $d = 2\text{mm}$ and the equilibrium contact angle $\theta_e = 45^\circ$. Adapted from Cai et al. [136].	45
Figure 3.7: Computed and analytical water column equilibrium height for different equilibrium contact angles. Adapted from Cai et al. [136].	45
Figure 4.1: (a) Initial shape of a droplet deposited on surface. (b) Its equilibrium shape for a given equilibrium contact angle θ_e . Adapted from Cai et al. [136].	47
Figure 4.2: Comparison of the present simulation results and the analytical solutions [46] in terms of H_e/R_0 and L_e/R_0 versus θ_e . Adapted from Cai et al. [136].	48
Figure 4.3: Comparison of the present simulation results and the analytical solutions [46, 170] in terms of normalized droplet height as function of the Eötvös number for $\theta_e = 60^\circ$. The insets show the final droplet shape for the respective Eötvös number. Adapted from Cai et al. [136].	49
Figure 4.4: Comparison of the simulation ($Pe_c = 200$ and 1000) and the experiment [171] with respect to instantaneous droplet base radius. Taken from Cai et al. [136].	51
Figure 4.5: (a) Initial state of the 3D AMR simulation (one-quarter geometry and hexahedral grid) of a droplet wetting on a solid surface (equilibrium contact angle	

$\theta_e = 75^\circ$). (b) A close-up into the interfacial zone where two-level AMR is applied. Taken from Cai et al. [136]. 53

Figure 4.6: 3D AMR simulation of a droplet spreading process on a solid surface with $\theta_e = 75^\circ$ at different instants of (a) $t/t_{cap} = 0$ (initial state), (b) $t/t_{cap} = 2$, (c) $t/t_{cap} = 8$ and (d) $t/t_{cap} = 30$ (equilibrium shape). Taken from Cai et al. [136]. 54

Figure 4.7: Comparison of 3D AMR and 2D axisymmetric stationary-grid simulations with respect to instantaneous droplet base radius. Taken from Cai et al. [136]. 54

Figure 4.8: PFM simulation of a droplet spreading process on the chemically-patterned surface (red stripes: SiO_2 , $\theta_e = 40^\circ$ and yellow stripes: PFDTs, $\theta_e = 110^\circ$) at different instants of (a) $t/t_{cap} = 0$ (initial state), (b) $t/t_{cap} = 40$, (c) $t/t_{cap} = 200$ and (d) $t/t_{cap} = 1000$ (equilibrium state). Taken from Cai et al. [136]. 56

Figure 4.9: Instantaneous base radius of the droplet in the parallel and perpendicular direction to the stripes. Taken from Cai et al. [136]. 57

Figure 4.10: Temporal evolution of the droplet from a bottom-view. (a) – (h): the experiment and LB simulation from Jansen et al. [172]; (i) – (l): the present PF simulation. The numbers at the bottom left corner in subfigures (e) – (h) denote time step while those in subfigures (i) – (l) refer to t/t_{cap} . Taken from Cai et al. [136]. 58

Figure 5.1: 2D axisymmetric phase-field simulation of an air bubble rising in quiescent liquid with $Cn = 0.02$, $Pe_c = 1008$, $N_c = 6$ and $N_d = 75$. Taken from Cai et al. [137]. 62

Figure 5.2: Simulated bubble rise velocity ($Cn = 0.02$ and $Pe_c = 1008$) with different mesh resolutions. Adapted from Cai et al. [137]. 64

Figure 5.3: Simulated bubble rise velocity ($Pe_c = 1008$ and $N_c = 6$) with different Cahn numbers. Adapted from Cai et al. [137]. 64

Figure 5.4: Simulated bubble rise velocity ($Cn = 0.02$, $N_c = 6$ and $N_d = 75$) with different Peclet numbers. The dashed horizontal line indicates the terminal bubble velocity measured by the experiment. Adapted from Cai et al. [137]. 65

Figure 5.5: Comparison of the present numerical results with the experimental data from Segers [177], with respect to the terminal bubble Reynolds number versus the Eötvös number. Adapted from Cai et al. [137].	67
Figure 5.6: Instantaneous gas-liquid interfacial area during the bubble splitting process, delivered by the phase-field simulations ($\theta_c = 30^\circ$, $Cn = 0.04$ and $Pe_c = 1000$) with different mesh resolutions. Adapted from Cai et al. [137].	69
Figure 5.7: Cylinder-induced bubble cutting process. (a) – (j): experimental and numerical results from Segers [177]. In the adapted presentation here, 0.15 s is deducted from the original time frame used by Segers [177], so that a shorter computational domain needs to be considered by the present phase-field simulation ($\theta_c = 60^\circ$) shown in (k) – (o). Adapted from Cai et al. [137].	71
Figure 5.8: Bubble breakup process under differing surface wettability of the cylinder. Adapted from Cai et al. [137].	73
Figure 5.9: Influence of cylinder surface wettability on temporal evolution of bubble interfacial area during the bubble splitting process. Adapted from Cai et al. [137].	74
Figure 5.10: The representative domain of a POCS considered in the present simulation with window size $s = 4$ mm, strut diameter $d_s = 1$ mm and grid angle $\alpha = 90^\circ$. The whole structure is tilted by 45° . Adapted from Cai et al. [137].	76
Figure 5.11: 3D view of the phase-field simulations of the bubble interacting process with the POCS under different surface wettability of the POCS. Adapted from Cai et al. [137].	78
Figure 5.12: 2D lateral view of the phase-field simulations of the bubble interacting process with the POCS under different surface wettability of the POCS. Adapted from Cai et al. [137].	79
Figure 6.1: (a) Sponge structures made of different materials: silicate (top), alumina (right) and silicon infiltrated silicon carbon (SiSiC) (bottom). (b) Cross-cut view of a SiSiC sponge in a working operation with gas-liquid flows. Within the cross-sectional circle, black and gray stand for solid and liquid respectively while the rest is for gas. Both figures (a) and (b) are from Wallenstein et al. [12].	85

Figure 6.2: Cubic REV of an alumina sponge with porosity $\psi := V_{\text{void}} / V_{\text{REV}} = 80\%$, 20 pores per inch (ppi) and edge length $a = 6\text{mm}$ 86

Figure 6.3: (a) 3D view of computational mesh for the cubic REV sponge geometry. (b) Cross-cutting view of the mid-plane outlined in red in (a). The solid region is shown in dark gray while the flow region in light gray. The mesh cell size for the bulk region is $h = 0.2\text{ mm}$ and mesh refinement of two levels is made near the solid sponge surface..... 87

Figure 6.4: Comparison of the present simulation results with the experimental data from [182] and *simpleFoam* numerical solution from [197], with respect to pressure drop per unit length $\Delta p / \Delta x$ versus superficial gas velocity U_0 for the alumina sponge. 88

Figure 6.5: (a) Original SiSiC sponge REV geometry with $\psi = 85\%$ and 20 ppi was provided by Institut für Thermische Verfahrenstechnik, KIT [197]. (b) Cubic REV geometry ($a = 10\text{ mm}$) obtained through the mirroring process with respect to the red-outlined plane perpendicular to x -coordinate. 92

Figure 6.6: Baseline simulation of gas-liquid two-phase flows at (a) initial state $t = 0\text{ s}$, (b) $t = 0.005\text{ s}$, (c) $t = 0.02\text{ s}$, (d) $t = 0.025\text{ s}$, (e) $t = 0.03\text{ s}$ and (f) equilibrium state $t = 0.05\text{ s}$ in the REV ($a = 0.01\text{ m}$) of SiSiC sponge. The equilibrium contact angle is $\theta_c = 90^\circ$. In the 3D images shown on LHS, the sponge structure is shown as semi-transparent to facilitate visualization of the gas-liquid interface denoted by the blue iso-surface. On RHS are the corresponding cross-cutting views for the gray mid-plane shown in the respective LHS images. 94

Figure 6.7: Influence of mesh resolution on predicted evolution of (a) liquid saturation β and (b) gas-liquid effective interfacial area A_{eff} with $Cn = 0.02$ and $Pe_c = 2500$ 96

Figure 6.8: Equilibrium state liquid distribution on sponge of surface wettability (a) $\theta_c = 40^\circ$ and (b) $\theta_c = 90^\circ$. In the both cases the liquid saturation is $\beta = 0.282$ 97

Figure 6.9: Influence of equilibrium contact angle θ_c on gas-liquid effective interfacial area A_{eff} for different liquid saturation β . The interfacial tension is $\sigma = 72\text{ mN m}^{-1}$ 98

Figure 6.10: Influence of interfacial tension coefficient σ on gas-liquid effective interfacial area A_{eff} for different liquid saturation β . The corresponding equilibrium contact angle θ_e is varied with σ as prescribed by the Young's equation (1.2). 99

Figure A.1: The hierarchy of the files within the test case folder *dropletSpreading*. 105

Figure A.2: An excerpt from the file *0/C.org* where one specifies the equilibrium contact angle denoted as *theta_0*..... 106

Figure A.3: The script file *setInitFields* where one initializes the order parameter field..... 107

Figure A.4: The file *constant/transportProperties* where one specifies physical properties of the two phases..... 108

Figure A.5: The file *constant/phaseFieldProperties* where phase-field specific parameters ε and κ are specified. 109

Publications:

I: Journal Articles

- [1] **X. Cai**, H. Marschall, M. Wörner and O. Deutschmann. Numerical simulation of wetting phenomena with a phase-field method using OpenFOAM®. *Chemical Engineering and Technology*, 38 (2015) 1985-1992.
- [2] **X. Cai**, M. Wörner, H. Marschall and O. Deutschmann. Numerical study on the wettability dependent interaction of a rising bubble with a periodic open cell structure. *Catalysis Today* 273 (2016) 151-160.
- [3] M. Wörner, **X. Cai**, H. Alla and P. Yue. A semi-analytical method to estimate the slip length of spreading cap-shaped droplets using Cox theory (under review).

II: Conference Proceedings Papers

- [1] **X. Cai**, H. Marschall, M. Wörner, O. Deutschmann. A phase field method with adaptive mesh refinement for numerical simulation of 3D wetting processes with OpenFOAM®, 2nd International Symposium on Multiscale Multiphase Process Engineering (MMPE), Hamburg, Germany, September 24-27, 2014.
- [2] **X. Cai**, M. Wörner, O. Deutschmann. Implementation of a Phase Field Method in OpenFOAM® for Simulation of Spreading Droplets and Verification by Test Problems, 7th Open Source CFD International Conference, Hamburg, Germany, October 24-25, 2013.

III: Conference Oral Presentations

- [1] **X. Cai**, M. Wörner, H. Marschall and O. Deutschmann. Numerical study on the wettability dependent interaction of a rising bubble with a periodic open cell structure. 5th International Conference on Structured Catalysts and Reactors (ICOSCAR-5), Donostia-San Sebastian, Spain, June 22–24, 2016.
- [2] **X. Cai**, M. Wörner, O. Deutschmann. Interface-resolving simulations of gas-liquid flows in a solid sponge structure. 9th International Conference on Multiphase Flow (ICMF 2016), Florence, Italy, May 22-27, 2016.

- [3] M. Wörner, **X. Cai**, H. Marschall, O. Deutschmann. Numerical study on the wettability- dependent interaction of droplets and bubbles with solid structures. 9th International Conference on Multiphase Flow (ICMF 2016), Florence, Italy, May 22-27, 2016.
- [4] **X. Cai**, M. Wörner, H. Marschall, O. Deutschmann. A Phase Field Method for Numerical Simulation of Wetting and Spreading Processes with OpenFOAM®, Jahrestreffen der ProcessNet Fachgruppen Fachgruppen Agglomerations- und Schüttguttechnik, Mehrphasenströmungen und Computational Fluid Dynamics, Bingen, Germany, 29. Feb. – 2. Mar. 2016.
- [5] H. Marschall, **X. Cai**, M. Wörner, O. Deutschmann. Development of Phase Field Methods using OpenFOAM® – Part I: Method Development and Implementation, 10th International OpenFOAM® Workshop, Ann Arbor, Michigan, USA, June 29 – July 2, 2015.
- [6] **X. Cai**, H. Marschall, M. Wörner, O. Deutschmann. Development of Phase Field Methods using OpenFOAM® – Part II: Application to Complex Wetting Physics, 10th International OpenFOAM® Workshop, Ann Arbor, Michigan, USA, June 29 – July 2, 2015.
- [7] B. Dietrich, S. Meinicke, **X. Cai**, M. Wörner. Structured chemical reactors: experimental analysis and simulation,ACHEMA 2015, Frankfurt, Germany, June 15–19, 2015.
- [8] **X. Cai**, H. Marschall, M. Wörner, O. Deutschmann. A Phase Field Method for Numerical Simulation of Wetting and Spreading Processes with OpenFOAM®, Jahrestreffen der ProcessNet Fachgruppen Computational Fluid Dynamics and Mehrphasenströmungen, Lüneburg, Germany, March, 19–20, 2015.
- [9] **X. Cai**, H. Marschall, M. Wörner, D. Bothe, O. Deutschmann. Development of Phase Field Methods for Direct Numerical Simulation of Wetting Processes with OpenFOAM®, 9th International OpenFOAM® Workshop, Zagreb, Croatia, June 23-26, 2014.
- [10] **X. Cai**, M. Wörner, O. Deutschmann. A Phase Field Method for Numerical Simulation of Wetting and Spreading Processes with OpenFOAM®, Jahrestreffen der ProcessNet Fachgruppen Computational Fluid Dynamics, Mischvorgänge und Rheologie, Würzburg, Germany, February 24-26, 2014.

IV: Conference Posters

- [1] **X. Cai**, H. Marschall, M. Wörner, O. Deutschmann. Development of Phase Field Methods with OpenFOAM® and its Application to Dynamic Wetting Processes, 2nd International Conference on Numerical Methods in Multiphase Flows, Darmstadt, Germany, June 30 — July 01, 2014.

V: Invited talks

- [1] **X. Cai**, H. Marschall, M. Wörner, O. Deutschmann. Computational Fluids Dynamics (CFD) Simulation of Wetting Phenomena, SIAM Student Chapter Seminar, Virginia Tech, Blacksburg, Virginia, USA, Feb. 12, 2015.
- [2] **X. Cai**, M. Wörner, O. Deutschmann. Implementation of a Phase Field Method in OpenFOAM® for Simulation of Spreading Droplets and Verification by Test Problems, Center of Smart Interfaces, TU Darmstadt, Darmstadt, Germany, Dec. 06, 2013.